

c./

MEASUREMENT OF THE FREE NEUTRON-PROTON  
ELASTIC DIFFERENTIAL CROSS SECTION AT  
212 AND 418 MEV OVER THE FULL ANGULAR RANGE



by Richard Dubois

B.Sc. McGill University (1976)  
M.Sc. UBC (1978)

A THESIS SUBMITTED IN PARTIAL FULFILLMENT OF  
THE REQUIREMENTS FOR THE DEGREE OF  
DOCTOR OF PHILOSOPHY

IN THE FACULTY OF GRADUATE STUDIES  
(DEPARTMENT OF PHYSICS)

WE ACCEPT THIS THESIS AS CONFORMING  
TO THE REQUIRED STANDARDS

The University of British Columbia

June, 1980

© Richard Dubois, 1980

In presenting this thesis in partial fulfilment of the requirements for an advanced degree at the University of British Columbia, I agree that the Library shall make it freely available for reference and study.

I further agree that permission for extensive copying of this thesis for scholarly purposes may be granted by the Head of my Department or by his representatives. It is understood that copying or publication of this thesis for financial gain shall not be allowed without my written permission.

Department of Physics

The University of British Columbia  
2075 Wesbrook Place  
Vancouver, Canada  
V6T 1W5

Date 27 Aug 1980

## ABSTRACT

The free neutron-proton elastic differential cross section has been measured at neutron beam energies of 212 and 418 MeV. The experiment determined the angular distribution over the range  $15^\circ$ - $180^\circ$  (CM) in two segments, having the same overall normalization. The  $15^\circ$ - $90^\circ$  range was measured by detecting scattered neutrons in a scintillator and MWPC array. Normalization was obtained by moving the array into the direct neutron beam. Energy selection was made via a time of flight (TOF) measurement relative to the TRIUMF cyclotron RF. The neutron detector was calibrated absolutely using an associated particle technique, in which the recoil proton was detected. The ratio of coincidentally observed neutron-proton pairs to protons alone yielded the efficiency, which was used to calibrate neutron beam monitors. The remainder of the angular distribution was obtained by detecting the scattered protons in a magnetic spectrometer. Proton selection was made using the TOF through the spectrometer and the momentum. Energy selection was made via the RF TOF. Normalization was provided by the same monitors as used in the measurement of the forward half of the angular distribution. The normalization of  $d\sigma/d\Omega$  has been determined to about 3%, with statistical accuracies of

about 1-3% on the individual data points. These data have been included in a phase shift analysis together with all world data, showing an improvement in the energy dependence of the differential cross section near  $0^\circ$  CM and in the phase shifts, notably  $\bar{E}_3$ . Together with the previously measured Wolfenstein parameters, unambiguous phase shifts in the  $I=0$  system are obtained for the first time in the TRIUMF energy range.

## ACKNOWLEDGEMENTS

I would like to express my appreciation to the members of the BASQUE group at TRIUMF for their invaluable help in performing these measurements. They are Claude Amsler, Ed Auld, Tony Clough, Martin Comyn, John Edgington, Reg Gibson, George Ludgate, Reg Richardson, Lyle Robertson, and Noel Stewart. In particular, I would like to thank David Bugg for calculating the corrections to the data, and for his overall guidance of the experimental program.

Many possibly tedious hours of my life have been diverted to more useful endeavours through the use of the excellent histogramming package, FLOWA, developed at TRIUMF by Arthur Haynes.

My thanks go to my supervisor, Mike Craddock, for his guidance and support during the four years of my education at the University of British Columbia and TRIUMF.

Much of that graduate and undergraduate education was shared with my friend and fellow student, Richard Keeler, with whom I have had uncounted hours of stimulating discussion and argument. His grasp of physics has often helped me with difficult problems.

I would like to express my deep gratitude to David Axen for teaching me the art of experimental physics. He has been the backbone of the BASQUE group, combining leadership, diplomacy and some larceny to keep it on course. He is largely responsible for the progress I have made in this work.

My loving wife, Deborah, has always given me the greatest support and encouragement throughout these four years and especially these last months of intensive work in completing the data analysis and preparation of this thesis.

THIS THESIS IS DEDICATED TO DEBORAH

## TABLE OF CONTENTS

I. INTRODUCTION .....	1
I.1 historical review .....	1
I.2 motivation for the experiment .....	4
I.3 description of the experimental method .....	6
II. PRINCIPLE OF THE EXPERIMENT .....	10
III. EXPERIMENTAL EQUIPMENT .....	16
III.1 fixed equipment .....	16
III.1.1 the cyclotron .....	18
III.1.2 proton polarimeter .....	22
III.1.3 neutron production target .....	25
III.1.4 neutron collimator .....	28
III.1.5 neutron beam intensity monitor .....	29
III.1.6 cleanup collimator and sweep magnet .....	32
III.1.7 liquid hydrogen target .....	34
III.1.8 downstream helium bag and beam dump .....	37
III.1.9 hydrogen target monitor .....	38
III.2 the neutron detector .....	41
III.2.1 the trigger scintillators .....	44
III.2.2 the veto counters .....	46
III.2.3 the multi-wire proportional chambers .....	46
III.4 apparatus for the efficiency measurement ...	48
III.6 the proton detector .....	52

III.7 electronics .....	57
IV. ANALYSIS AND RESULTS .....	64
IV.1 analysis of neutron counter data .....	64
IV.1.1 event selection .....	65
IV.1.1.1 time of flight .....	67
IV.1.1.2 MWPC track fitting .....	73
IV.1.2 the neutron beam .....	80
IV.2 measurement of the absolute efficiency of the neutron detector .....	84
IV.2.1 principle and requirements of the measurement .....	84
IV.2.2 data taking .....	91
IV.2.3 corrections to the number of nucleons incident on the detectors .....	94
IV.2.4 analysis with no exit track angle cut .....	97
IV.2.5 analysis with a $170^\circ$ exit track angle cut ..	101
IV.2.6 error analysis .....	108
IV.3 the neutron monitors .....	112
IV.3.1 monitor stability .....	112
IV.3.2 monitor linearity with neutron flux .....	115
IV.3.3 random coincidences in the monitors .....	118
IV.4 analysis of the forward hemisphere data .....	119
IV.4.1 elimination of backgrounds .....	119
IV.4.2 corrections due to equipment problems .....	121
IV.4.3 empty target subtraction .....	122

IV.4.4 zero degree data .....	123
IV.4.5 time of flight cuts on the data .....	125
IV.4.6 corrections to the raw data .....	126
IV.4.6.1 incident beam .....	126
IV.4.6.2 data at non-zero angles .....	127
IV.4.7 parameters needed to calculate $d\sigma/d\Omega$ .....	129
IV.4.8 error estimate .....	131
IV.4.9 angular distributions .....	134
IV.4.10 cross calibration of the monitors .....	136
IV.4.10.1 absolute monitor efficiencies .....	136
IV.4.10.2 error estimate .....	138
IV.5 analysis of the backward hemisphere data ....	139
IV.5.1 selection of events .....	141
IV.5.2 total energy counter .....	152
IV.5.3 reduction of the raw data .....	155
IV.5.4 empty target data .....	155
IV.5.6 corrections to the data due to equipment aberrations .....	156
IV.5.7 corrections to the raw data .....	158
IV.5.8 parameters needed to calculate $d\sigma/d\Omega$ .....	160
IV.5.9 error estimation .....	162
IV.5.10 angular distributions .....	165
IV.6 in retrospect .....	173
IV.7 comparison of experimental techniques .....	173
V.INTERPRETATION OF THE DATA .....	175

V.1 principle of phase shift analysis .....	175
V.2 current status of the phase shift analysis ...	179
V.3 new data in the phase shift analysis .....	182
V.2.1 data near 212 MeV .....	182
V.2.2 data near 418 MeV .....	187
V.3 energy dependencies .....	190
V.4 conclusion .....	195
References .....	196
APPENDIX A. MWPC TRACK FITTING CRITERIA .....	201
APPENDIX B. CORRECTION FOR INCOMPLETE AZIMUTHAL ACCEPTANCE OF DETECTORS .....	204
B.1 principle of the algorithm .....	205
B.2 application to the neutron detector .....	214
APPENDIX C. DENSITIES OF LIQUID AND GASEOUS HYDROGEN IN THE TARGET .....	217
APPENDIX D. INVENTORY OF MATERIALS .....	223

## LIST OF FIGURES

1. EXPERIMENTAL CONFIGURATIONS .....	8
2. SCATTERED NUCLEON KINETIC ENERGY VERSUS LABORATORY ANGLE .....	14
3. OVERVIEW OF APPARATUS USED IN THE MEASUREMENTS ...	17
4. THE TRIUMF FACILITY .....	19
5. BEAM LINE 4A .....	23
6. PROTON POLARIMETER .....	24
7. THE LIQUID DEUTERIUM TARGET .....	26
8. NEUTRON BEAM INTENSITY MONITORS .....	30
9. CLEANUP COLLIMATOR AND SWEEP MAGNET .....	33
10. THE LIQUID HYDROGEN TARGET .....	35
11. TARGET MONITOR .....	39
12. THE NEUTRON DETECTOR .....	42
13. SCHEMATIC OF THE P1 AND P2 SCINTILLATOR ARRAYS ..	45
14. MULTI-WIRE PROPORTIONAL CHAMBERS .....	49
15. THE RECOIL PROTON TELESCOPE .....	50
16. THE PROTON SPECTROMETER .....	53
17. ELECTRONICS FOR THE NEUTRON MONITORS .....	59
18. ELECTRONICS FOR THE NEUTRON DETECTOR .....	60
19. ELECTRONICS FOR THE PROTON SPECTROMETER .....	61
20. ELECTRONICS FOR THE COMPUTER GATING AND EVENT READOUT .....	62

21. MEASUREMENT OF THE FORWARD HEMISPHERE OF THE DIFFERENTIAL CROSS SECTION .....	66
22. RESOLUTION OF THE TIME OF FLIGHT MEASUREMENT AS A FUNCTION OF KINETIC ENERGY .....	668
23. TIME DIFFERENCE BETWEEN ELASTICALLY SCATTERED NEUTRONS AND BACKGROUNDS .....	670
24. TIME OF FLIGHT OF CHARGED PARTICLES THROUGH THE NEUTRON DETECTOR .....	72
25. VERTICAL PROFILE OF EVENTS FROM THE CARBON CONVERTER WITH NO EXIT TRACK ANGLE CUT .....	75
26. DETERMINATION OF THE MAXIMUM ALLOWABLE EXIT TRACK ANGLE FROM THE CONVERTER .....	76
27. VERTICAL PROFILE OF EVENTS AT THE CARBON WITH AN EXIT TRACK ANGLE CUT OF $17^{\circ}$ .....	78
28. VERTICAL AND HORIZONTAL PROFILES OF THE NEUTRON BEAM .....	81
29. CALIBRATION OF THE NEUTRON DETECTOR .....	85
30. ENVELOPE OF ACCEPTED NEUTRONS DETERMINED BY THE RECOIL ARM .....	87
31. HORIZONTAL AND VERTICAL PROFILES OF NEUTRONS AT THE CARBON IN THE CALIBRATION .....	90
32. TOF AND ADC SPECTRA IN THE CALIBRATION MEASUREMENT .....	93
33. EXIT TRACK ANGLE DISTRIBUTION .....	98
34. NEUTRON DETECTOR EFFICIENCIES WITHOUT EXIT TRACK	

CUTS .....	100
35. RATIO OF EFFICIENCIES WITH AND WITHOUT THE EXIT TRACK ANGLE CUT .....	102
36. NEUTRON DETECTOR EFFICIENCIES WITH EXIT TRACK CUTS .....	105
37. RATIO OF IN-BEAM TO OUT-OF-BEAM MONITOR COUNTS AS A FUNCTION OF TIME .....	113
38. RELATION BETWEEN THE OUT-OF-BEAM MONITOR AND PROTON POLARIMETER COUNT RATES .....	116
39. TYPICAL P1-RF TOF SPECTRUM FOR THE NEUTRON DETECTOR .....	120
40. NEUTRON BEAM RF TIME OF FLIGHT SPECTRUM .....	124
41. CONFIGURATION FOR THE BACKWARD HEMISPHERE MEASUREMENT .....	140
42. PARTICLE IDENTIFICATION IN THE SPECTROMETER .....	144
43. MOMENTUM DIFFERENCE BETWEEN ELASTIC PROTONS AND MOST ENERGETIC INELASTIC PROTONS .....	145
44. CORRELATION OF MOMENTUM AND RF TOF .....	147
45. PROFILE OF EVENTS FROM THE LIQUID HYDROGEN TARGET .....	148
46. INTERSECTION OF TRACKS FROM THE TWO HALVES OF THE SPECTROMETER AT THE MAGNET CENTER .....	150
47. MOMENTUM OF THE FULL ENERGY ELASTIC PROTONS .....	151
48. CORRELATION OF PULSE HEIGHT IN S4 WITH THE TOF FROM S1 TO S2 .....	153

49. PULSE HEIGHT IN S4 FOR FULL ENERGY PROTONS .....	154
50. AVERAGE POLAR SCATTERING ANGLE .....	161
51. BACKWARD HEMISPHERE DIFFERENTIAL CROSS SECTION AT 212 MEV .....	168
52. PREVIOUS BACKWARD HEMISPHERE DIFFERENTIAL CROSS SECTION DATA NEAR 212 MEV .....	169
53. BACKWARD HEMISPHERE DIFFERENTIAL CROSS SECTION AT 418 MEV .....	170
54. PREVIOUS BACKWARD HEMISPHERE DIFFERENTIAL CROSS SECTION DATA NEAR 418 MEV .....	171
55. ENERGY DEPENDENCE OF THE DIFFERENTIAL CROSS SECTION .....	192
56. ENERGY DEPENDENCE OF THE I=0 PHASE SHIFTS .....	193
57. ENERGY DEPENDENCE OF THE I=1 PHASE SHIFTS .....	194
B1. ALLOWED REGIONS OF THE AZIMUTHAL SCATTERING ANGLE .....	206
B2. GEOMETRY OF THE $\phi_{1-2}$ ALGORITHM .....	208
B3. ROTATION OF THE EXIT TRACK ELLIPSE BY THE INCIDENT AZIMUTHAL ANGLE .....	211
B4. DEFINITION OF THE EIGHT POSSIBLE INTERSECTIONS OF THE ELLIPSE AND THE DETECTOR BOUNDARIES .....	213
B5. VERTICAL PROFILE AT THE CARBON WITH P2E FAILED ..	216
C1. TEMPERATURE OF THE LIQUID AS A FUNCTION OF THE PRESSURE .....	218
C2. DENSITY OF THE LIQUID HYDROGEN AS A FUNCTION OF	

TEMPERATURE .....	219
C3. HYDROGEN GAS PRESSURE AND DENSITY AS FUNCTIONS OF ENTROPY .....	221
C4. HYDROGEN GAS DENSITY AS A FUNCTION OF TEMPERATURE .....	222
D1. MEAN PATH LENGTH OF SCATTERED PROTONS IN HYDROGEN .....	226

## LIST OF TABLES

1. WORLD DATA FOR THE N-P DIFFERENTIAL CROSS SECTION . . .	7
2. DIMENSIONS OF THE NEUTRON BEAM MONITOR COUNTERS . . .	31
3. DIMENSIONS OF THE HYDROGEN TARGET MONITOR COUNTERS . . .	40
4. DIMENSIONS OF THE NEUTRON DETECTOR SCINTILLATORS . . .	43
5. DIMENSIONS OF THE RECOIL ARM COUNTERS . . . . .	51
6. DIMENSIONS OF THE SPECTROMETER SCINTILLATORS . . . . .	55
7. NEUTRON BEAM PROPERTIES . . . . .	82
8. RECOIL ARM AND NEUTRON DETECTOR CONFIGURATIONS . . . . .	89
9. MULTIPLE SCATTERING AND ATTENUATION CORRECTIONS . . .	96
10. NEUTRON DETECTOR EFFICIENCIES WITHOUT EXIT TRACK CUTS . . . . .	99
11. NEUTRON DETECTOR EFFICIENCIES WITH EXIT TRACK CUTS . . . . .	106
12. ERROR ESTIMATES FOR THE EFFICIENCY OF THE NEUTRON DETECTOR . . . . .	110
13. CORRECTIONS TO THE MONITORS FOR INDUCED ACTIVITY . . .	117
14. CORRECTIONS TO THE FORWARD HEMISPHERE DATA . . . . .	128
15. VARIATION OF $D\sigma/D\Omega$ FOR VARIOUS CHOICES OF THE CUTS . . . . .	133
16. RESULTS FOR THE DIFFERENTIAL CROSS SECTION AT 212 AND 418 MEV . . . . .	135
17. ABSOLUTE EFFICIENCIES OF THE NEUTRON MONITORS . . . . .	137

18. CALCULATED CORRECTIONS TO THE DATA .....	159
19. SENSITIVITY OF THE BACKWARD DIFFERENTIAL CROSS SECTION TO THE RF CUTS .....	163
20. BACKWARD HEMISPHERE DIFFERENTIAL CROSS SECTION AT 212 MEV .....	166
21. BACKWARD HEMISPHERE DIFFERENTIAL CROSS SECTION AT 418 MEV .....	167
22. PHASE SHIFTS PREDICTED FROM THE PREVIOUS DATA AT 212 AND 418 MEV .....	181
23. PHASE SHIFT FITTED VALUES OF THE NORMALIZATIONS FOR DATA NEAR 212 MEV .....	185
24. PHASE SHIFTS FROM THE CURRENT ANALYSIS AT 212 MEV	186
25. PHASE SHIFT FITTED NORMALIZATIONS FOR DATA NEAR 418 MEV .....	188
26. PHASE SHIFT RESULTS FROM THE CURRENT ANALYSIS AT 418 MEV .....	191
D1. THICKNESS OF MATERIALS BETWEEN THE HYDROGEN TARGET AND SPECTROMETER .....	225

## I. INTRODUCTION

### I.1 HISTORICAL REVIEW

Study of the nucleon-nucleon (N-N) force has been a central occupation for physicists since the discovery of the neutron by Chadwick<sup>1</sup>. Nucleons are the most accessible tools for a study of the strong interaction. Furthermore, as they are considered to be the basic constituents of nuclei, knowledge of their interaction is relevant to an understanding of nuclear properties. With these two goals in mind, a tremendous amount of effort has been invested in the experimental determination and theoretical explanation of the nucleon-nucleon interaction.

The first decade of research was devoted to identifying the properties of the force: that it was energy dependent<sup>2</sup>; that the core region was strongly repulsive<sup>3</sup>; that a new symmetry, Isospin<sup>4</sup>, was respected by it; and that non-central forces<sup>5</sup>, tensor and spin-orbit, were present as well. With this information, the most general form of the interaction potential was

constructed<sup>6</sup>, although there was little or no understanding of the processes which generated the force.

A major success was made by Yukawa<sup>7</sup> in his generalization of the ideas of electrodynamics, in which he postulated the strong force to be mediated by the exchange of virtual particles that, by necessity, had finite mass to account for the short range of the force. With the discovery of the pion, by Powell<sup>8</sup> in 1947, and further experimental evidence, it was shown<sup>9</sup> that his view well described the long range (greater than a few pion Compton wavelengths) properties of the force.

In light of this success, much effort was poured into the meson theoretic approach<sup>10</sup> which hoped to show that the short and medium range components of the strong interaction were due to the exchange of other, heavier mesons. Two short-comings were apparent in this approach: the strong force did not lend itself to perturbation theory; and, in order to fit the experimental data, a medium mass meson, the  $\sigma$ , was required<sup>11</sup>. The  $\sigma$  meson has never been found experimentally.

At this time, phenomenological approaches<sup>12</sup> were taken to describe the interaction. Combining knowledge of the form of the potential with experimental measurement of

a limited number of NN observables, analyses were undertaken that parametrized the amplitudes in terms of phase shifts. The high angular momentum (and so, long range) phases were calculated from the one pion exchange (OPE) potential and the remainder were determined from the data. These values of the phase shifts were then available for use in nuclear theory calculations.

An outgrowth of the meson exchange ideas has been combined with the technique of dispersion relations<sup>13-15</sup> to provide the currently accepted mode of calculation. Through applications of the principles of analyticity, unitarity, and crossing, the dispersion relations describing the N-N interaction are transformed into those requiring knowledge of  $\pi N$ ,  $\pi\pi$ , and  $eN$  interactions, but nothing of the actual N-N force itself. This method encounters difficulties at short range, owing to computational problems in including the exchange of systems of mass greater than two pions. To produce an "all radius" potential, the core region is parametrized from N-N data, with the hope that this region ( $< 0.8$  fm) will soon be calculable in the theory of quantum chromodynamics (QCD). In this approach, fits have been obtained to the data which are of comparable quality to those of the phenomenological phase shift analyses (PSA).

## I.2 MOTIVATION FOR THE EXPERIMENT

Information on the isospin dependence of the N-N force requires an examination of interactions of both the proton-proton (p-p) and neutron-proton (n-p) systems; the p-p case has access only to the  $I=1$  channel, whereas the n-p case involves both  $I=0$  and  $I=1$  channels.

At the outset of this experiment, data for the p-p system were of adequate quality, while those for the n-p system in the energy range 200 - 500 MeV were scarce and of low accuracy. Input of the data into the PSA gave non-unique solutions for the parameters<sup>16</sup>. Furthermore, there were systematic disagreements between some of the data sets, especially around 300 MeV, e.g. the data from the Princeton-Pennsylvania Accelerator<sup>17</sup> (PPA) and Liverpool<sup>18</sup>.

Using phase shift analyses as a base, a study<sup>19</sup> was undertaken to assess the best set of experiments to perform in order to maximize the resulting information. The procedure used was iterative, in that "measurements", with errors, of various observables were input to the analysis and the effect observed. The result of the study was that measurements of the following free, elastic n-p

observables were expected to be the to best improve the data set:

Wolfenstein parameters  $D, R, A, D_t, R_t, A_t$   $55^\circ-125^\circ$   
 CM  $\pm 0.03$   
 Polarization  $P$   $55^\circ-125^\circ$  CM  $\pm 0.02$   
 differential cross section  $5^\circ-180^\circ$  CM  $\pm 1\%$

The error level shown was arbitrary, but typical of that required. To date, the Wolfenstein parameters and polarization have all been measured, leaving only the differential cross section to finish the experimental program, aimed at fixing all  $I=0$  phases to the same precision as the  $I=1$  phases.

Measurement of the differential cross section to this level became possible with the advent of the high flux "meson factories"<sup>20</sup> so that high intensity, nearly monoenergetic neutron beams became available, using deuterium targets for neutron production. Additionally, and perhaps most importantly, this measurement of  $d\sigma/d\Omega$  is novel in that it is the first in the intermediate energy range 200-500 MeV to provide a distribution over the entire angular range with a single normalization.

Due to the kinematics of n-p scattering, the rate and

energy of scattered particles decrease rapidly approaching 90° lab. Consequently, it becomes impractical to detect the scattered neutrons over the entire angular range. In practice, only forward going, energetic particles are detected: neutrons, to obtain the forward part; and forward scattered protons for the backward region. These measurements had previously always been done by separate methods and different experimental groups. Table 1 lists the previously existing cross section data in the vicinities of the energies 212 and 418 MeV.

### 1.3 DESCRIPTION OF THE EXPERIMENTAL METHOD

The technique used in this experiment was as follows (Fig 1). The neutron beam, monitored by an upstream detector, was incident on a proton target with the scattered neutrons observed by a neutron detector. As is explained later in the text, use of the technique of placing the detector in and out of the incident beam largely eliminated detector efficiencies from the measurement, allowing calculation of  $d\sigma/d\Omega$ . The neutron detector was then calibrated absolutely by a conjugate particle method: scattered protons were counted in one arm while some neutrons were detected at the kinematically

<u>Neutron Energy</u>	<u>Center of Mass Angular Range (deg)</u>	<u>Performed At</u>
195.6	11 - 51	PPA <sup>46</sup>
196	111 - 179	PPA <sup>47</sup>
199	76 - 158	Rochester <sup>48</sup>
200	6 - 180	Dubna <sup>49</sup>
210	11 - 51	PPA <sup>46</sup>
210	111 - 179	PPA <sup>47</sup>
211.5	120 - 180	LAMPF <sup>42</sup>
215	76 - 178	Rochester <sup>48</sup>
224	111 - 179	PPA <sup>47</sup>
224	11 - 51	PPA <sup>46</sup>
390.2	11 - 53	PPA <sup>46</sup>
400	12 - 178	Carnegie <sup>50</sup>
414	60 - 180	PPA <sup>48</sup>
421	151 - 180	Saclay <sup>43</sup>
428.9	118 - 180	LAMPF <sup>42</sup>

**Table 1. World data for the n-p differential cross section.**

This Table lists all the previously existing data on the differential cross section near the energies 212 and 418 MeV.

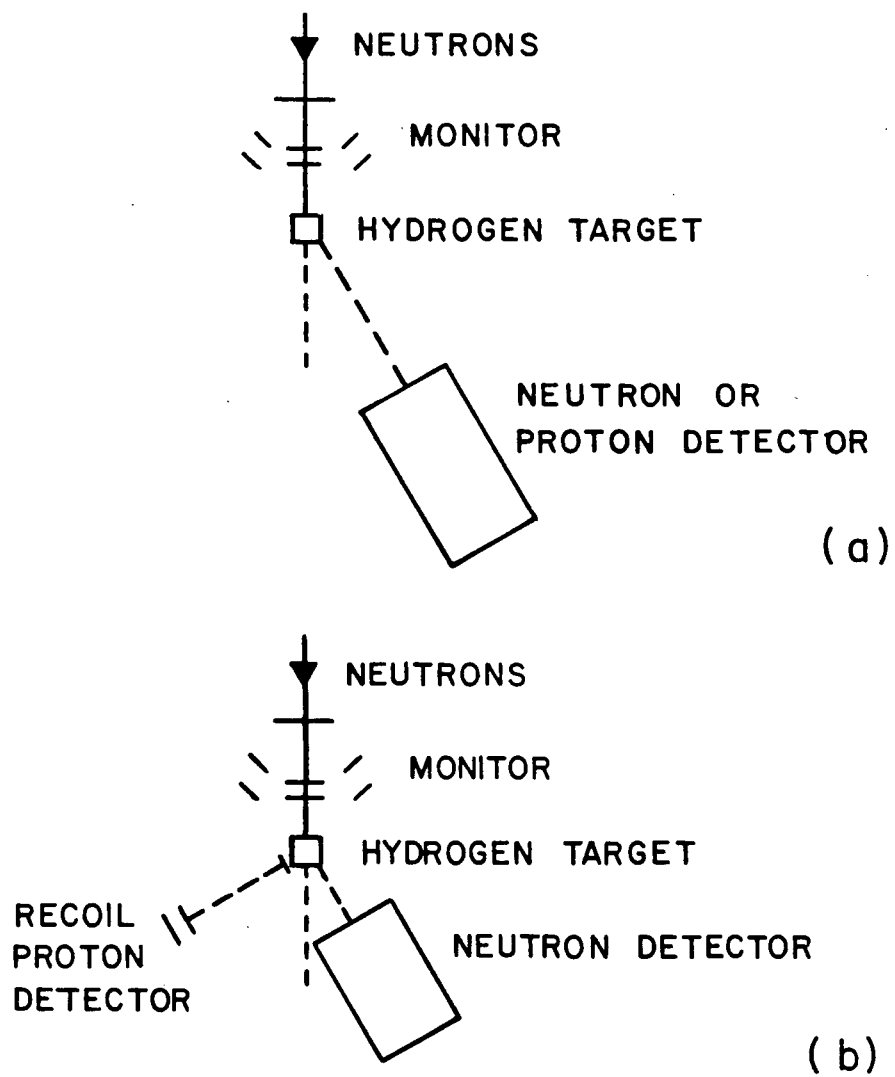


Fig 1. Experimental configurations.

Fig(a) shows the setup used to measure the differential cross section. Fig(b) shows the setup for the calibration of the neutron monitors.

conjugate angle by the neutron detector, giving the absolute efficiency of the detector. This information was used to cross-calibrate the upstream monitor, giving its efficiency for detecting neutrons.

Armed with this information, measurement of the backward hemisphere could proceed. Scattered protons were detected with virtually 100% efficiency. With the number of incident neutrons known from the same monitor, the cross section was obtained, with the same normalization as the forward hemisphere.

The object of this thesis is to report on the measurement of  $d\sigma/d\Omega$  over the entire angular range at two energies, 212 and 418 MeV. The calibration of the neutron detector and monitor is also discussed.

Finally, the results of this measurement are incorporated with the world data set on all N-N observables into a phase shift analysis, completing this program of elastic n-p work.

## II. PRINCIPLE OF THE EXPERIMENT

The interpretation of the n-p elastic differential cross section is that it is the probability that a neutron incident upon a target proton will scatter elastically into a specified solid angle. In principle, it can simply be determined by counting both the incident number of neutrons and the number scattered into the solid angle of interest. In practice, however, the counting of neutrons is difficult due to the generally low and energy-dependent efficiencies of all neutron detectors.

For a detector with a small solid angle of acceptance,  $d\Omega$ , the number of neutrons scattered into it,  $N_s$ , is given by

$$N_s = n_0 n_t t \frac{d\sigma}{d\Omega} d\Omega$$

where  $n_0$  is the incident number of neutrons

$n_t$  is the density of target protons

$d\sigma/d\Omega$  is the elastic n-p

differential cross section (laboratory frame)

$d\Omega$  is the solid angle subtended by the detector, and

$t$  is the target thickness.

With a neutron detector of finite size, efficiency  $\varepsilon$ , and a beam monitor having efficiency  $\eta$ , the numbers of particles detected are

$$N_p = \varepsilon \frac{N_{\text{mon}}}{\eta} n_t t \frac{d\sigma}{d\Omega} d\Omega \quad (1)$$

where  $N_p$  is the number counted by the neutron detector, and

$N_{\text{mon}}$  is the number counted by the neutron monitor.

The functional dependences of the variables should be noted here:

$$\eta = \eta(E)$$

$$\varepsilon = \varepsilon(x, y)$$

$$\frac{d\sigma}{d\Omega} = \frac{d\sigma}{d\Omega}(\theta, E)$$

$$n_0 = n_0(x', y')$$

$$N_p = N_p(\theta, E)$$

Here  $(x, y)$  correspond to coordinates describing the plane perpendicular to the scattered particle direction;  $E$  represents the kinetic energy of the particle; and  $\theta$  the polar scattering angle. The  $(x', y')$  are the coordinates perpendicular to the incident beam direction. Henceforth, the  $(x, y)$  variations shall be neglected and considered only as corrections to the ideal case of uniformity in spatial coordinates.

The efficiencies  $\eta$  and  $\epsilon$  are generally unknown, but can be eliminated if the measurements are made with the detector placed in the incident neutron beam: both the detector and the monitor sample the same beam.

$$N_p(0) = \epsilon(E_i) \frac{N_{\text{mon}}(\theta=0)}{\eta(E_i)} \quad (2)$$

With  $E$  the energy of the incident beam. Combining eq (1) and (2), noting that in eq (1)  $\epsilon(E) = \epsilon(E_s)$ , the scattered energy, one gets

$$\frac{N_p(\theta, E_s)}{N_p(0, E_i)} = \frac{\epsilon(E_s)}{\epsilon(E_i)} \frac{N_{\text{mon}}(\theta)}{N_{\text{mon}}(0)} t \frac{d\sigma}{d\Omega} d\Omega n_t$$

and

$$\frac{d\sigma}{d\Omega}(\theta, E_i) = \frac{N_p(\theta, E_s)}{N_p(0, E_i)} \frac{\epsilon(E_i)}{\epsilon(E_s)} \frac{N_{\text{mon}}(0)}{N_{\text{mon}}(\theta)} \frac{1}{n_t t d\Omega}$$

The monitor efficiency,  $\eta(E)$ , has cancelled out and only the relative energy efficiency variation of the neutron detector remains.

Fig 2 shows a typical plot of scattered particle kinetic energy as function of laboratory scattering angle. The rate and energy of the scattered particles drop rapidly as the angle approaches  $90^\circ$  lab. It is well known that neutron detector efficiencies fall rapidly with energy in the range (100 - 500 MeV). It is practically impossible to detect a single type of particle over the entire angular range and one must detect protons in the range  $0^\circ - 50^\circ$  (lab) to measure the backward angular distribution of the scattered neutrons.

With a proton detector one cannot simply move into the incident neutron beam to cancel out the monitor efficiency. It must be known absolutely a priori. As has been described briefly in the introduction, it is determined by cross-calibration from the neutron detector efficiency, when it is also in the neutron beam so that both the neutron detector and monitors sample the same neutron beam.

Once  $\eta$  is known, the number counted by the proton detector, of essentially unit efficiency, is

$$N_p(\theta) = \frac{N_{mm}(\theta)}{\eta(E_i)} n_t t \frac{d\sigma(\theta_r)}{d\Omega}$$

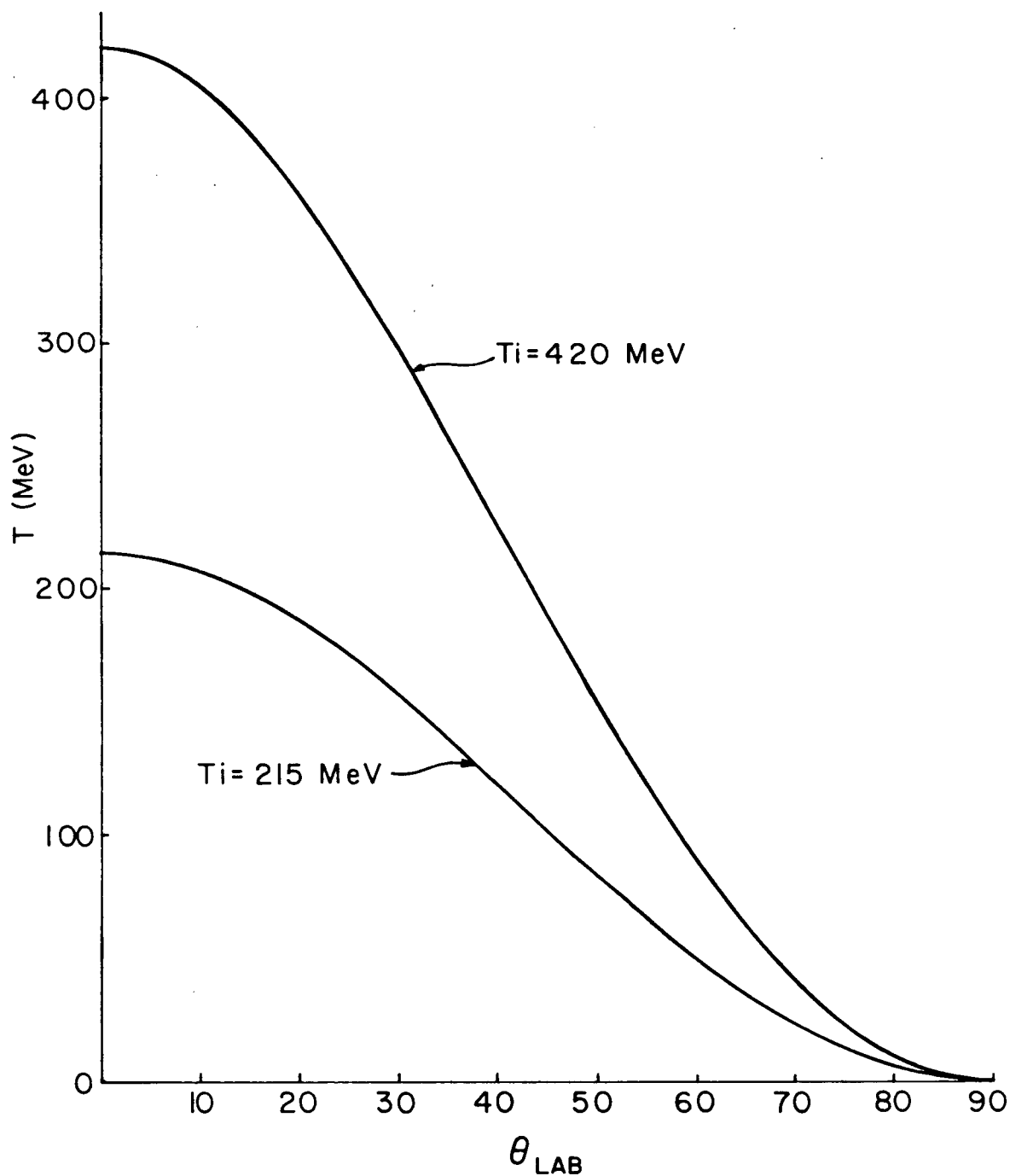


Fig 2. Scattered nucleon kinetic energy versus laboratory angle.

The variation of the scattered nucleon's kinetic energy with polar lab scattering angle is shown for incident kinetic energies of 215 and 420 MeV.

with  $\theta_r$  being the conjugate angle to  $\theta$ , and  $d\sigma/d\Omega$  the only unknown in the equation.

To summarize, having measured the absolute efficiency of the neutron monitor, the differential cross section is obtained over the entire angular range with a single normalization.

### III. EXPERIMENTAL EQUIPMENT

As discussed in the previous chapter, the object of the measurements was to determine the number of neutrons incident on the target, and the number of neutrons (or protons) scattered into a given solid angle. Fig 3 shows a schematic of the apparatus used to perform the measurement.

Neutrons produced at the deuterium target scattered from the liquid hydrogen ( $\text{LH}_2$ ) target. The scattered neutrons (or protons) were observed in a movable detector.

#### III.1 FIXED EQUIPMENT

This section deals with the elements of apparatus which were fixed on the experimental floor, ie. did not involve the movable neutron or proton detectors.

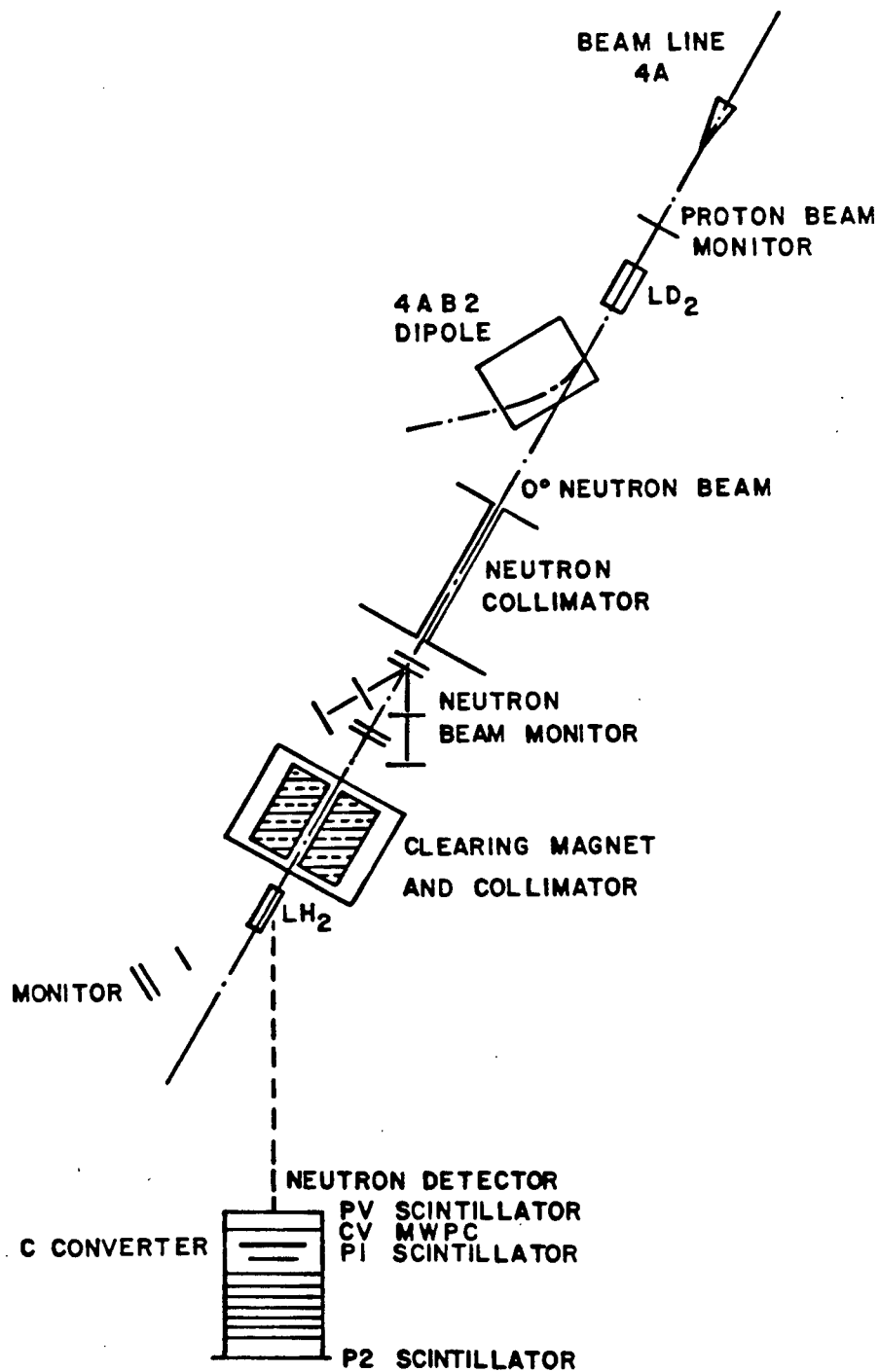


Fig 3. Overview of apparatus used in the measurements.  
 Neutrons produced at the LD<sub>2</sub> target are collimated and then scatter in the LH<sub>2</sub> target into a movable detector. The neutron detector is shown here.

### III. 1. 1 The Cyclotron

The primary proton beam was produced by the TRIUMF sector-focused cyclotron<sup>21</sup>. The protons, accelerated as H<sup>-</sup> ions, are extracted by a carbon or aluminium "stripper" foil. The radial distance of the foil from the cyclotron determines the energy of the extracted beam, which is variable from about 183-518 MeV.

Two beams are typically extracted (Fig 4), one into the "proton" hall, and the other into the "meson" hall. As TRIUMF is principally a meson factory, proton currents of from 10-100  $\mu$ A are delivered to B11 for a high meson flux. The needs of the proton hall are in the region of 0.5  $\mu$ A, and for this experiment, went as low as 2-5 nA. Consequently, much effort had been put into achieving large split ratios between the extracted currents of B11 and 4. It has been found that ratios of up to 1000:1 can be maintained to about 5%.

The proton currents required by this experiment varied over a factor of about 100, so that techniques were required that would allow variation of the beam intensity without change in the other properties of the beam: spatial position, size and energy. Simply reducing the

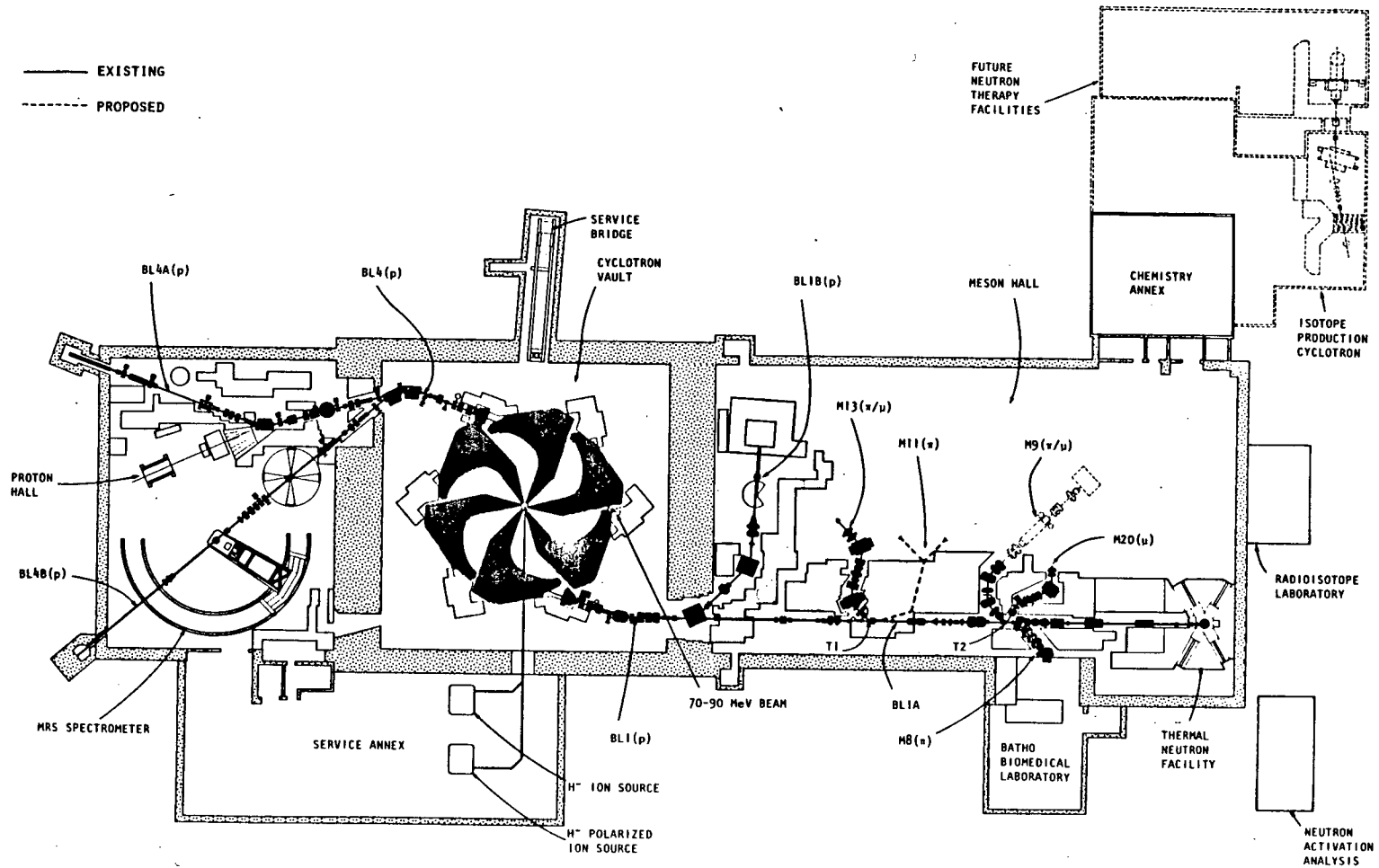


Fig 4. The TRIUMF Facility

Two independent beams are extracted from the cyclotron. One goes to the proton hall for N-N and nuclear physics studies and the other to the meson hall.

current in the ion source, which produces the  $H^-$  ions that are injected into the cyclotron, was inadequate as that procedure changed the emittance of the beam injected to the cyclotron.

Three techniques were used at various times in the data taking: making use of a pulser on the ion source, which eliminated a given fraction of the beam pulses; defocussing a lens element (the Einzel lens) on the injection beamline to dump unwanted portions of the beam; and altering the vertical position of the stripper foil, to intercept a variable fraction of the proton beam circulating in the cyclotron tank. These three methods were found to be equivalent in their ability to allow low beam currents to be extracted without changing beam properties in going from high currents.

The cyclotron radio-frequency (RF) accelerating cavity operates at 23 MHz, and so every 43 ns a proton bunch, of up to 5 ns duration, is extracted from the cyclotron tank. The bunch width could be varied down to about 2 ns through the use of a "buncher" and chopper on the injection line.

The RF signal, available to the experiment, had a constant phase with respect to the proton bunch extraction

time. This signal served two purposes: it gave a reference time with which to clock the arrival of particles at the experimental station, allowing determination of the particles' energy by the time of flight<sup>22</sup> (TOF) method (which will be described later in the text); and, permitted one to observe "decelerated" beam<sup>23</sup>. Beam in the cyclotron tank, which is not stripped and extracted, is accelerated to the outer edge of the tank where it slips out of phase with the RF, is decelerated back to the stripper foil and extracted. These protons would arrive at the experiment at a time different from, but with the same energy as, the main proton beam, which could cloud the results of the TOF method.

Since the RF period was 43 ns, timings relative to the RF signal were modulo 43 ns. Particles which took multiples of 43 ns to reach the experiment appeared to have identical energy in the TOF method. To examine this effect, a "1:5 selector"<sup>24</sup> was used to mechanically suppress four out of every five proton bursts from the cyclotron, to a level of about  $10^{-4}$ . Data taken in this way could then be used to see whether there was any hydrogen-associated low energy background that "wrapped around" to be under the elastic neutron peak.

The proton beam was transported to the neutron

production target using conventional magnetic elements, shown in Fig 5. The beam line elements were carefully tuned to ensure that the beam properties were not affected by small drifts in the settings of the elements.

Several remotely insertable, gas-filled, multi-wire proportional chambers were available along the beam line to check the spatial properties of the beam. Two, having 3 mm wire spacing, were located just upstream of the neutron production target. The spot size of the beam on these monitors was typically  $5 \times 5 \text{ mm}^2$ .

As further checks, there were also a split plate monitor and a polarimeter upstream.

### III.1.2 Proton Polarimeter

A twin double arm polarimeter (Fig 6) was mounted just upstream of the neutron production target. In previous experiments it had been used to monitor the polarization of the proton beam in the measurement of the free n-p Wolfenstein parameters. In this experiment, it was used as an intensity monitor and to check on the horizontal steering of the proton beam.

The arms of the polarimeter were set at the

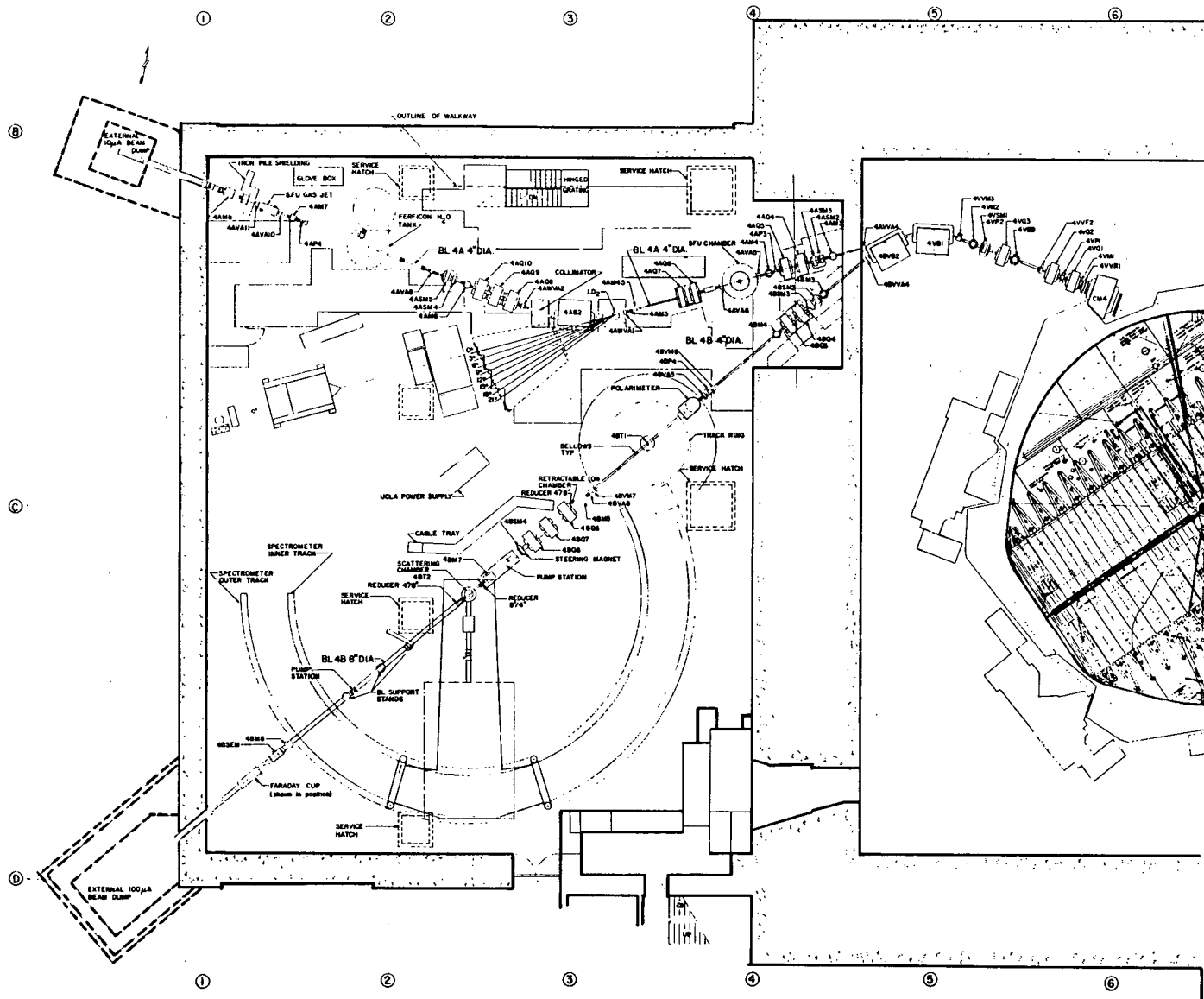


Fig 5. Beam line 4A

Protons extracted from the cyclotron are transported to the experimental area via magnetic focussing and bending magnets. Downstream of this experiment, the proton beam goes to a well shielded dump.

1st LETTER	2nd LETTER	SUBSCRIPT
R RIGHT	R RECOIL	F FRONT
L LEFT	F FORWARD	R REAR

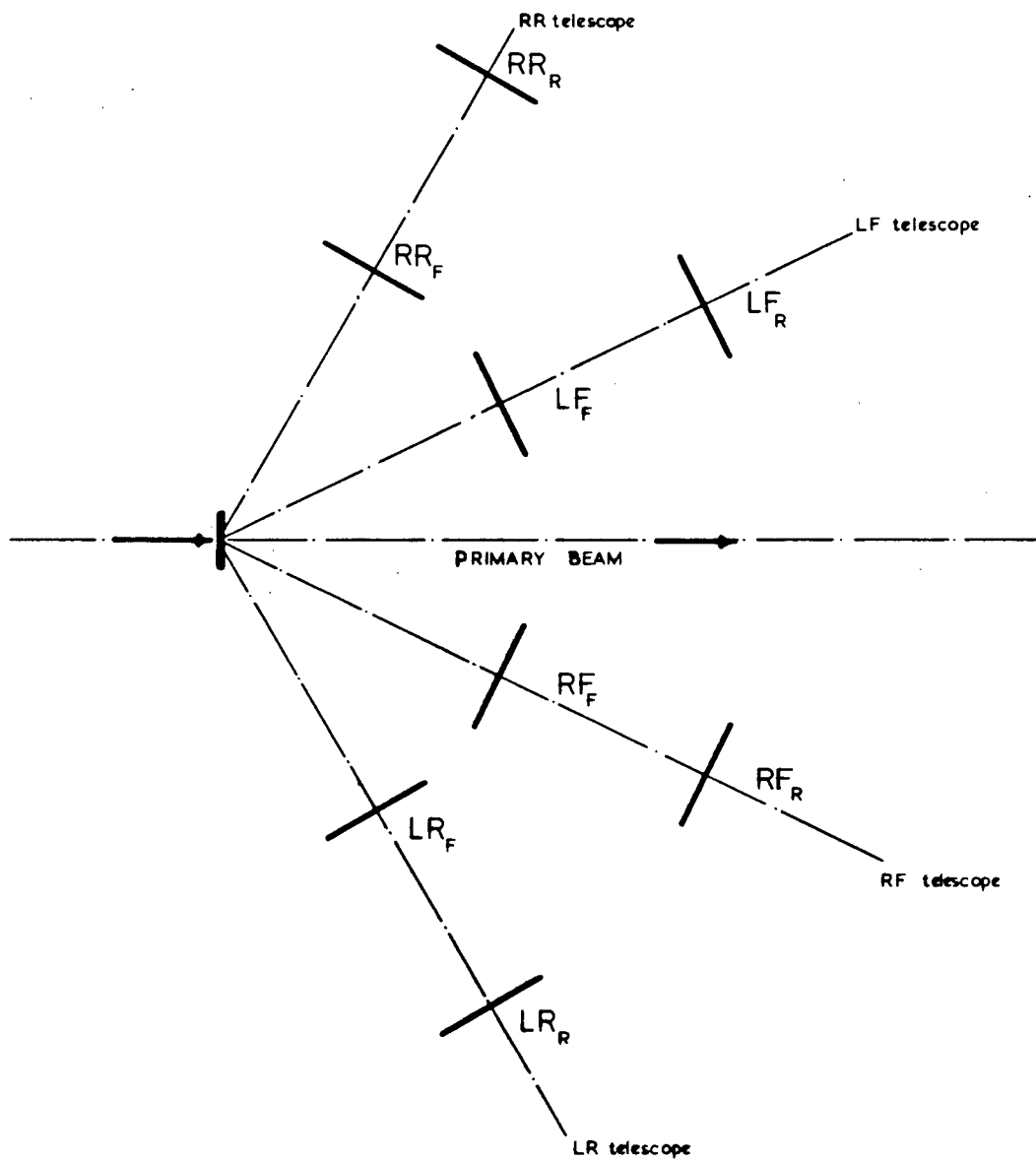


Fig 6. Proton polarimeter.

The proton polarimeter, upstream of the  $LD_2$  target, detected left-right asymmetries in elastic p-p scattering, by observing both protons in two twin-arm counters.

kinematically conjugate angles for elastic p-p scattering from the 0.127 mm thick CH<sub>2</sub> target. Any differences in the scattering rates between the left and right arms indicated a horizontal mis-steering of the proton beam (mainly due to the rapid change of the proton-carbon differential cross section with scattering angle).

Due to requirements of other experimenters on the beam line, the CH<sub>2</sub> target was changed frequently so that the polarimeter could not be used as a long term intensity monitor.

### III.1.3 Neutron Production Target

Neutrons were produced at zero degrees with respect to the incident proton direction by quasi-elastic scattering of the incident proton beam from a liquid deuterium (LD<sub>2</sub>) target<sup>25</sup>. Immediately downstream of the target a bending magnet was used to transport the remaining proton beam to the beam stop. On the way there, the beam was monitored by a secondary emission counter. The magnet also served to eliminate charged particles coming from the target from the resulting neutron beam.

The target flask, shown in Fig 7, of length 203 mm by

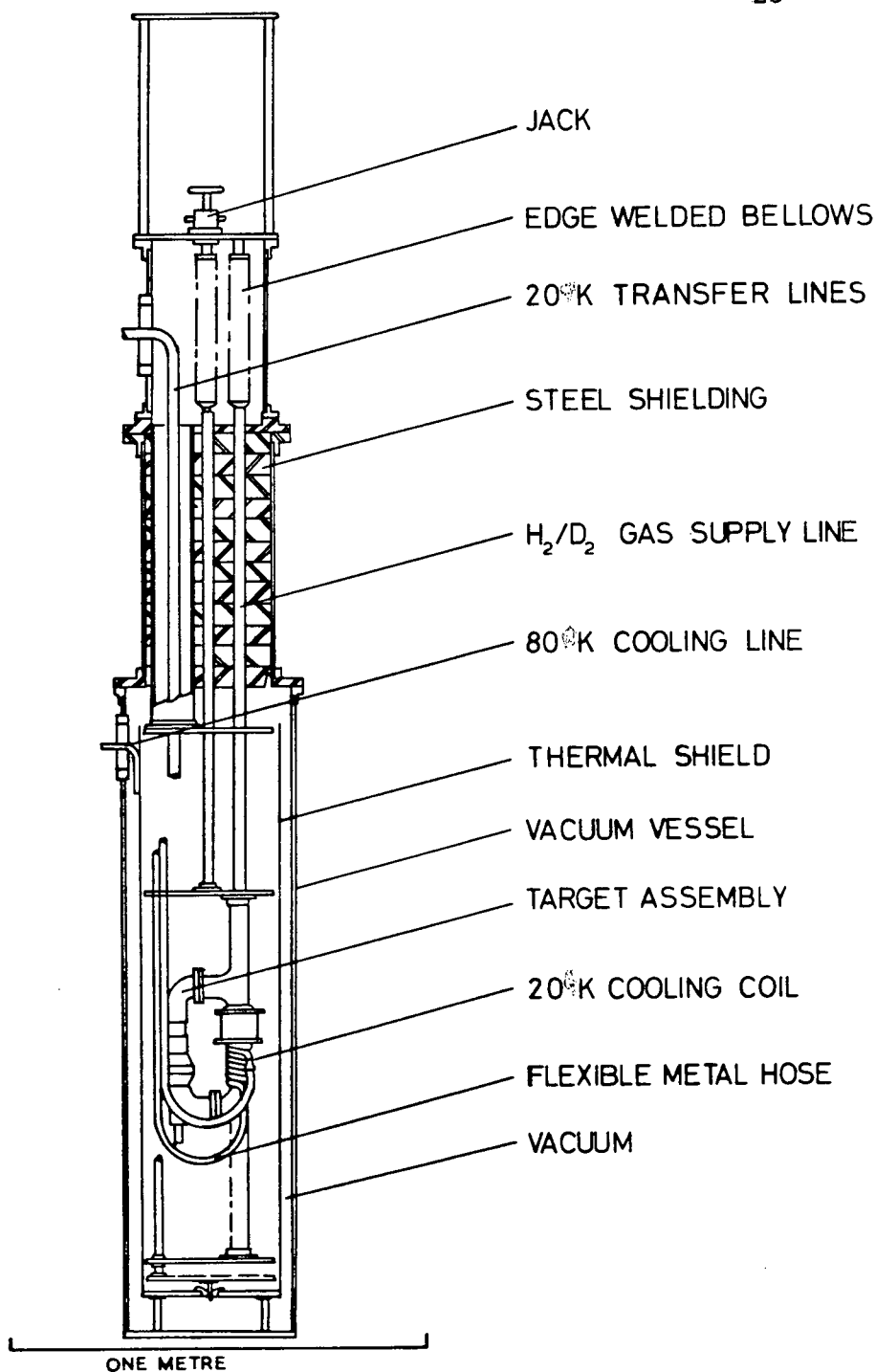


Fig 7. The liquid deuterium target.

The deuterium is held in the region denoted "target assembly". Three orientations are possible by moving the assembly up or down: a dummy cell, a carbon target, and the deuterium flask.

51 mm diameter, held the liquid deuterium. The target end windows were made of 50  $\mu\text{m}$  stainless steel, while the target vessel was separated from the beam pipe vacuum by windows of 120  $\mu\text{m}$  thickness.

Target cooling was provided by a Philips A-20 cryogenerator with two cooling lines. The 20K line fed the heat exchanger directly, while the 80K line cooled the radiation shield. The target could be filled in approximately twelve hours (most of this time required to cool the chamber) and emptied in about one hour.

A hydrogen bulb thermometer and carbon resistors were used to monitor the flask's temperature and pressure. These quantities were interfaced into the cyclotron control system, giving access to them at any time.

### III.1.4 Neutron Collimator

A collimator was used to define the size of the neutron beam and shield the experimental area and equipment. It could be used to look at any angle of scatter from the liquid deuterium target from  $-30^\circ$  to  $30^\circ$  in  $3^\circ$  steps. In this experiment, only the  $0^\circ$  port was left open, the others being filled with steel plugs.

At the upstream entrance, the steel pipes were of 100 mm diameter and in the center were of 125 mm diameter. They were placed between steel plates, with the spaces between the pipes filled with lead. The length of the  $0^\circ$  port was 3.3 m and its diameter was reduced to 3.81 cm by specially made steel plugs.

### III.1.5 Neutron Beam Intensity Monitor

The incident neutron flux was monitored by an assembly of counters, forming two independent monitors, placed upstream of the hydrogen target. These monitors had to deal with changes in the neutron flux over two orders of magnitude. For this reason, they were built in the configuration shown in Fig 8.

The in-line counters, G1 and G2, were intended to work at low intensities, while the out-of-beam counters, CR and CL, placed at  $290^\circ$  to the incident neutron direction, were for high intensities. The two monitors provided internal consistency checks on each other, as well as for checking the beam conditions.

A small fraction of the neutron beam interacted in the 2.54 cm thick  $\text{CH}_2$  slab to produce charged particles, which were detected by the monitor counters. The veto, CV, ensured that the neutral particle flux could be monitored. The CH slab was made larger than the collimator exit hole, making the monitors insensitive to small shifts in the neutron beam shape. Copper plates eliminated some of the low energy background in the out-of-beam monitor. At 212 MeV, 0.635 cm thick plate was used, while 1.91 cms

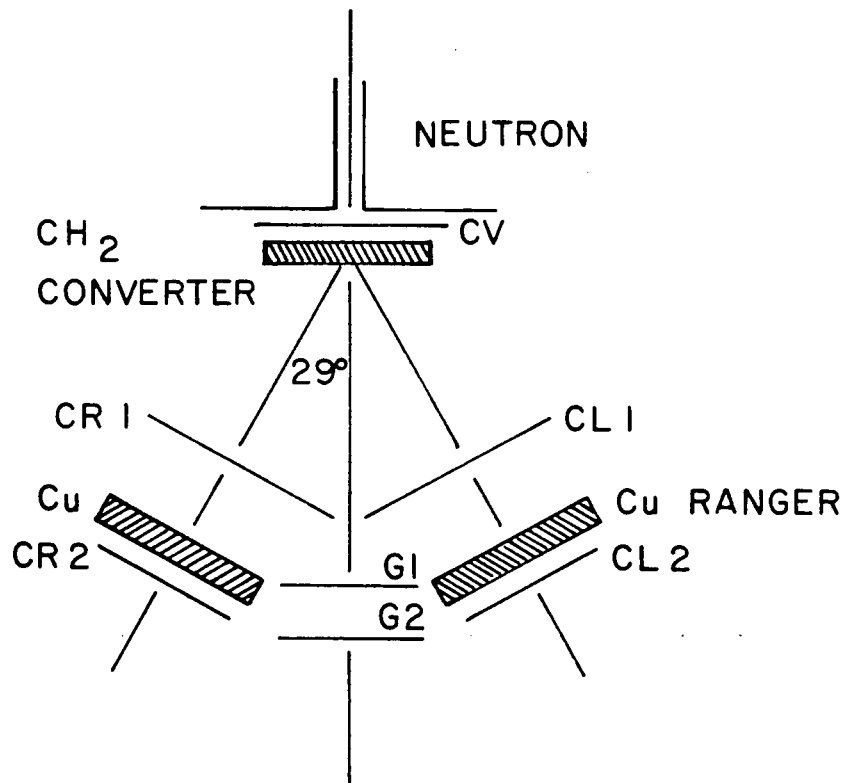


Fig 8. Neutron beam intensity monitors.

Neutrons interacted in the  $\text{CH}_2$  converter to produce charged particles which were detected in three counter arms. The two out-of-beam arms were summed to give one monitor, and the in-beam arm was the second monitor. Copper ranger was included in the out-of-beam monitor to reduce the low energy background.

<u>Counter</u>	<u>Height</u> (cm)	<u>Width</u> (cm)	<u>Thickness</u> (cm)
CV	25.0	25.0	0.30
CL1	20.3	20.3	0.32
CL2	15.2	15.2	0.32
CR1	20.3	20.3	0.32
CR2	15.2	15.2	0.32
G1	25.0	25.0	0.30
G2	25.0	25.0	0.30

Table 2. Dimensions of the neutron beam monitor counters.

were used at 418 MeV. Table 2 gives the dimensions of the monitor counters.

### III.1.6 Cleanup Collimator And Sweep Magnet

A secondary collimator (Fig 9) was employed to reduce the neutral particle background from the main collimator and the monitors. It was constructed of an aluminium frame filled with lead bricks and shot, placed between the pole faces of the sweep magnet. Emphasis was placed on shielding the angular region over which the detectors moved, and geometrically, the shielding restricted the background to scattering angles of less than about  $5^\circ$ . The upstream bore of the collimator was 5.08 cm, and was 47 cm long.

An inner helium bag was utilized along the length of the secondary collimator to reduce scattering of the neutron beam in the air upstream of the hydrogen target. The sweep magnet was used to remove charged particle backgrounds produced by the neutron beam upstream, as no veto counter was placed upstream of the target. It was found that the veto introduced more background than it eliminated, by converting a fraction of the neutron beam without self-vetoing. The sweep magnet field was held at

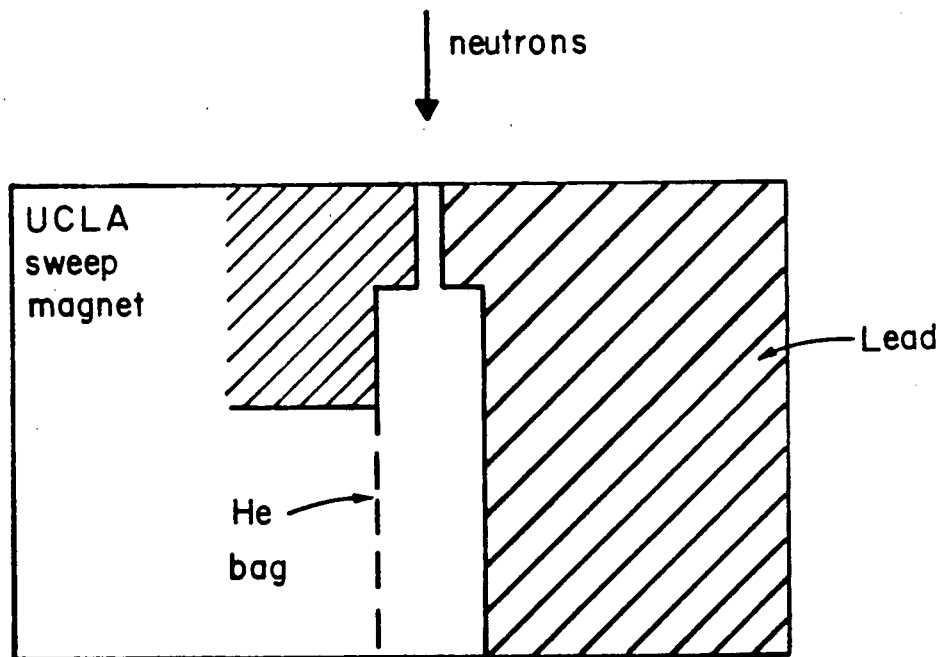


Fig 9. Cleanup collimator and sweep magnet.  
The secondary collimator reduced the background from the upstream monitors and the lips of the main collimator. The sweep magnet removed any remaining charged particles.

10 kgauss throughout the experiment.

### III.1.7 Liquid Hydrogen Target

The liquid hydrogen ( $\text{LH}_2$ ) was contained in a mylar flask which, at room temperature, was 199.5 mm long with a 136.5 mm diameter (Fig 10). Cooling was provided by a Stirling cycle engine which could cool the target to liquid in about twenty-four hours. Once cold, it could be remotely emptied in about eight minutes, leaving cold gas in the flask, and filled in about two minutes.

The density of the liquid was most accurately determined by monitoring the pressure of the gas on the boil-off line. The normal operating pressure was 17 psia, corresponding to a density of  $0.0701 \text{ g/cm}^3$ . The refrigerator cut in and out on pressure excursions of  $\pm 0.25$  psia variation from the operating point, while a 3 psia variation corresponded to a 1% change in the density.

The temperature of the flask was monitored by a Cu/Constantan thermocouple attached to the center top of the flask, and was continuously recorded. The typical gas density was  $5.4 \cdot 10^{-4} \text{ g/cm}^3$ . Knowledge of the empty target gas density was required in order to correct the

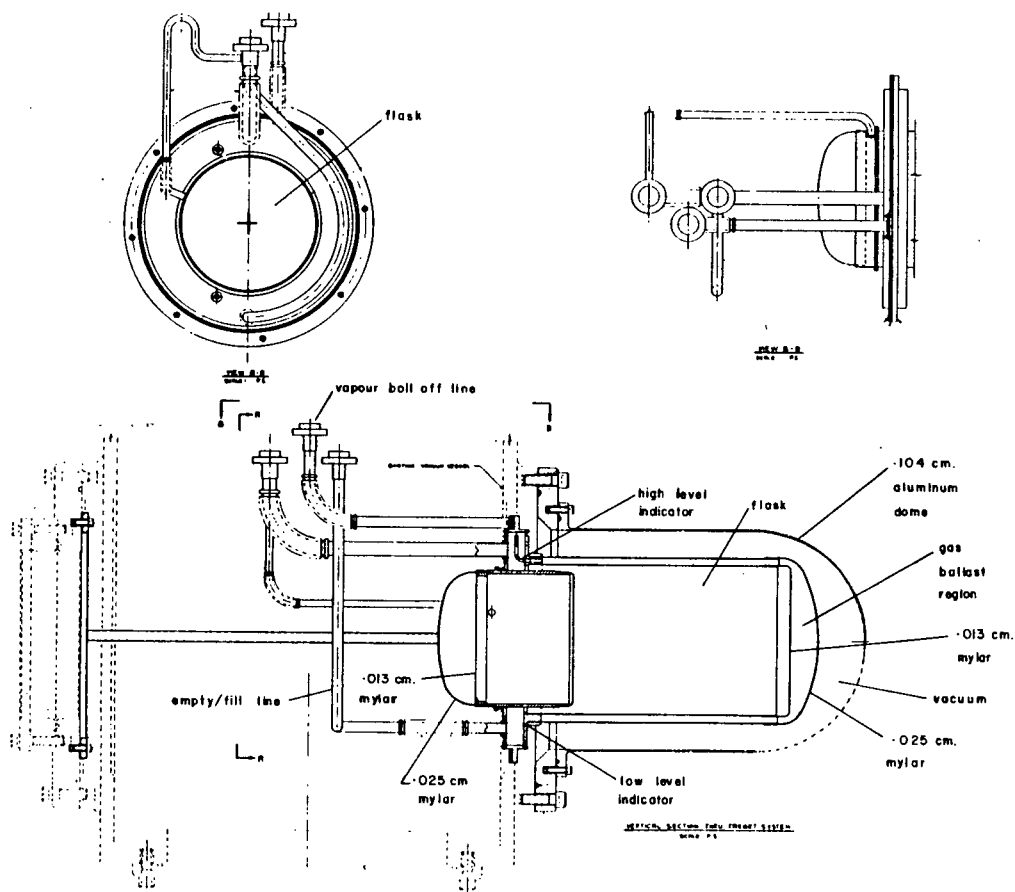


Fig 10. The liquid hydrogen target.

The target flask was surrounded by a gas ballast region maintained at the same pressure. The evacuated region outside the gas ballast was surrounded by a spun aluminium dome.

empty target subtraction, as is described later.

The length of a similar target was measured at both room and liquid nitrogen temperatures, and was found to contract by 0.4% of its magnitude. By linear extrapolation, this gave a target length at liquid hydrogen temperature of 198.5 mm, with 0.1 mm as an upper limit on the error of the extrapolation.

In the  $H_2$  molecule, there are two possible orientations of the proton spins: parallel (ortho-) and anti-parallel (para-), which occur in the ratio of 3:1, and have different thermal properties<sup>26</sup>. To make the liquid homogeneous, a catalyst was used to convert virtually all of the hydrogen molecules to the para state. The substance used was a nickel silicate having the brand name APACHI-1 produced by Houdry Division of Air Products.

The mylar end windows of the flask were 0.013 cm thick. The flask was covered with ten layers of 6.3  $\mu$ m aluminized mylar ("superinsulation"), and was surrounded by a gas ballast region whose walls were 0.025 mm thick mylar. This region was in contact with the liquid, and so was maintained at the same pressure. The evacuated region, outside the gas ballast, was enclosed by a spun aluminium dome, 0.107 cm thick. This dome was found to be the main

contributor to background events.

### III.1.8 Downstream Helium Bag And Beam Dump

A self supporting helium bag, made of mylar, was placed downstream of the  $LH_2$  target to reduce background from the neutron beam scattering from air in this region. The cylinder was 630 cm long by 36 cm diameter, strengthened by inner styrofoam rings and supported by two styrofoam stands.

At the end of the  $0^\circ$  line, a stack of concrete blocks supported two rows of  $15 \times 7.5 \times 5$  cm<sup>3</sup> lead bricks. The bricks were placed to the left of the incident beam so that when the detector was at a non-zero angle, the bricks were between the detector and the intersection point of the beam and the wall.

### III.1.9 Hydrogen Target Monitor

A three counter telescope (Fig 11) was used to provide an additional monitor of the  $\text{LH}_2$  target status. It was placed at  $45^\circ$  to the neutron beam, with the solid angle defining counter 70 cm from the center of the target. The telescope acceptance was limited to approximately the volume of the flask. The placement and dimensions were chosen to optimize the constraints that the counting rate be higher than that of the detector at any angle; that it accept charged particles from the region of the flask only; and that it be out of the path of the detector. The counter dimensions are listed in Table 3.

This completes the discussion of the fixed equipment. The remaining discussion of the apparatus will deal with the neutron detector, used in the forward hemisphere measurement, the recoil arm, used to calibrate the neutron detector, and, finally, the proton detector used for the backward hemisphere data.

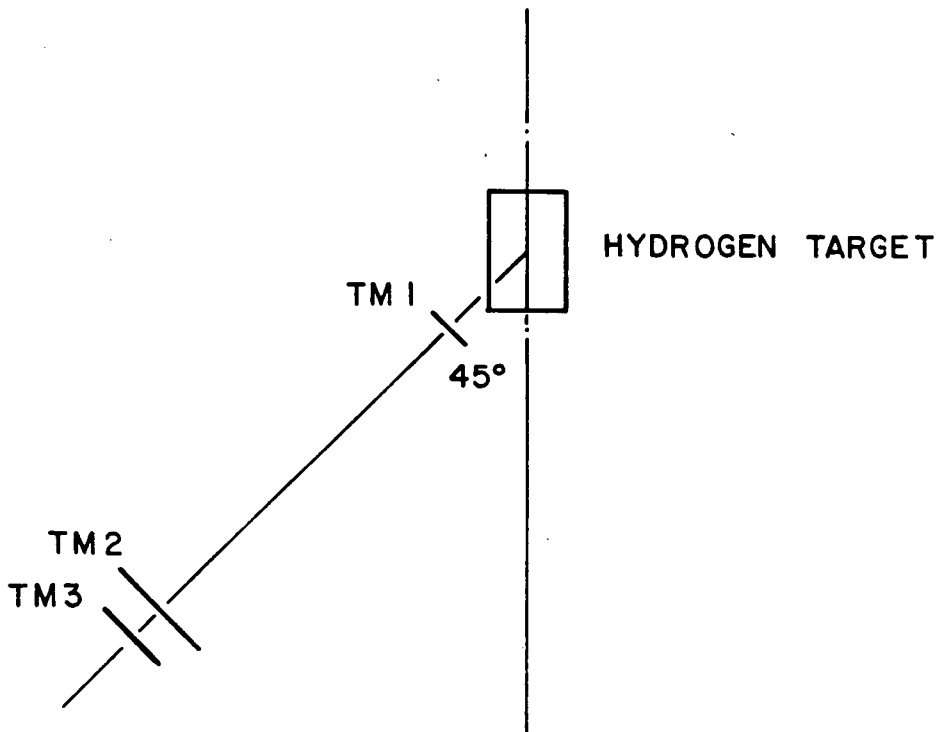


Fig 11. Target monitor.  
The status of the LH<sub>2</sub> target was monitored by a three counter telescope at 45° to the incident beam direction.

<u>Counter</u>	<u>Height</u> (cm)	<u>Width</u> (cm)	<u>Thickness</u> (cm)
TM1	6.0	6.0	0.32
TM2	10.0	10.0	0.32
TM3	6.0	6.0	0.32

Table 3. Dimensions of the hydrogen target monitor counters.

### III.2 THE NEUTRON DETECTOR

The principle involved in the neutron detector was to allow a neutral particle to impinge on a block of carbon, where there was a probability of interaction that resulted in charged particles emerging from the block. These charged particles were detected by scintillation counters and indicated the interaction of a neutral particle in the carbon converter.

The apparatus used for the detector is shown in Fig 12. The carbon block was  $53 \times 53 \times 9$  cm<sup>3</sup> and was followed by two trigger scintillators, P1 and P2, which detected the converted charged particles. The carbon block was 5.57 m from the target center. The detector was mounted on wheels and was attached to a center post, underneath the hydrogen target, by radius arms. The dimensions of all the scintillators used are listed in Table 4.

An aluminium plate 1 cm thick was placed between the two scintillators in order to reduce the number of triggers from low energy background events. The plates were approximately one metre square in area.

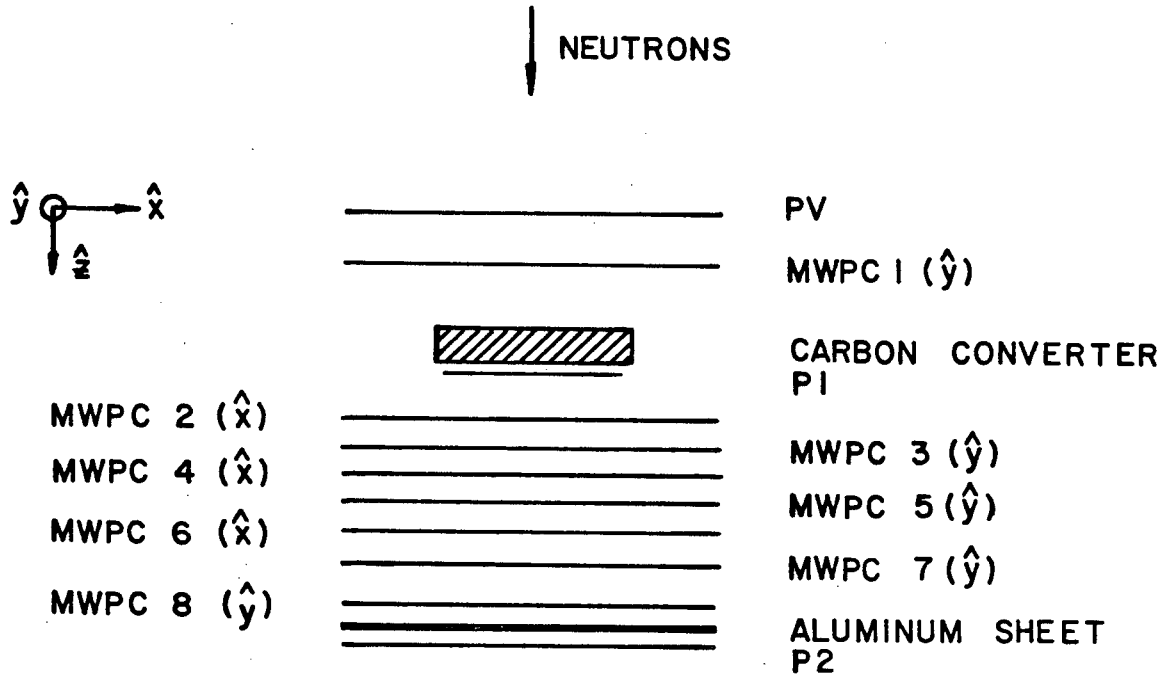


Fig 12. The neutron detector.

Neutrons incident on the detector interacted in the carbon converter to produce charged particles which were detected in the scintillator and MWPC array downstream of the converter. Charged particles incident on the detector were vetoed by a combination of a scintillator and MWPC.

Counter	Height (cm)	Width (cm)	Thickness (cm)
P1	50.0	50.0	0.64
PV A-F	74.4	36.5	0.30
PV G-H	100.0	15.0	0.32
P2 A-F	74.4	36.5	0.30
P2 G-H	100.0	15.0	0.32

Table 4. Dimensions of the neutron detector scintillators.

### III.2.1 The Trigger Scintillators

P2 consisted of a hodoscope of scintillation counters, shown Fig 13, to give the better timing resolution that can be obtained from smaller counters. P1 was made smaller in area than the carbon block in an attempt to minimize edge effects. To further reduce backgrounds, the P1 scintillator was viewed by two photomultipliers, one at the top, the other at the bottom. Requiring a coincidence between the two tubes eliminated some of the background due to noise in the tubes, and due to such phenomena as Cerenkov light from cosmic ray muons passing through either light guide. In an attempt to get the best timing from all the scintillators on the detector, the light guides were made adiabatic, in which the guides were segmented along the edge of the scintillator, joining at the cylindrical light guide base, the length of each segment being equal.

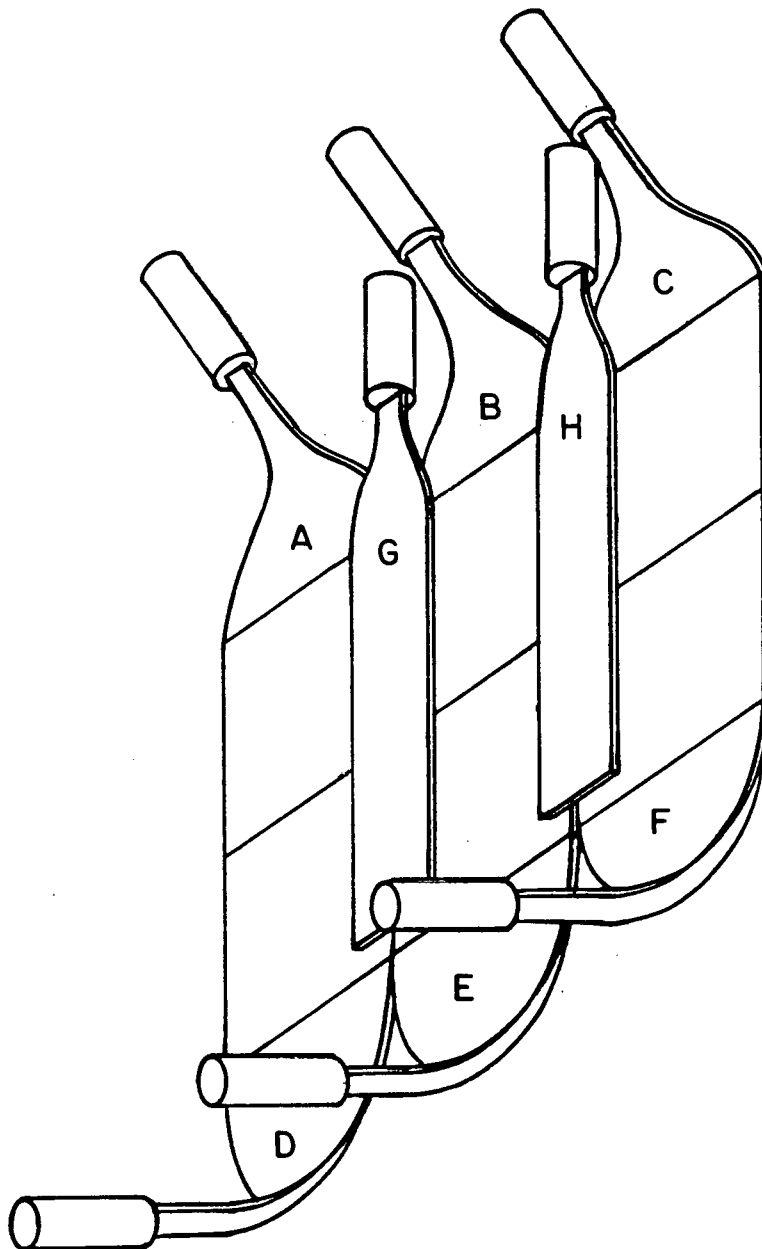


Fig 13. Schematic of the PV and P2 scintillator arrays.

The PV and P2 hodoscopes were identical. The one meter-square area was covered by six scintillators from above and below (A-F) overlapped in the middle, and two scintillators (G-H) covered the spaces between the others.

### III.2.2 The Veto Counters

Two veto counters were used to ensure that only neutral particles were able to trigger the detector: a scintillator hodoscope (PV), identical to P2 in configuration; and a multi-wire proportional chamber (MWPC, to be described shortly). The MWPC was used as a low mass device to pick up charged particles missed by PV, or conversion of neutrals in PV. The need for very high vetoing efficiency is best illustrated by an example: with a detector having efficiencies of 2% and 100%, respectively, for neutrons and charged particles, a veto efficiency of 99% would result in a charged particle background of 50% for equal fluxes of both particles.

### III.2.3 The Multi-wire Proportional Chambers

There were seven MWPC's between P1 and P2 to reconstruct the tracks of the converted charged particles through the detector. The principle use of this information was to identify the location of the interaction in the carbon block. There were three MWPC's giving horizontal coordinates and four giving vertical coordinates.

The operational characteristics of the MWPC's have been well described elsewhere<sup>27</sup>. Consequently, only the properties important to this measurement are discussed here. The MWPC's were constructed with a wire spacing of 2 mm. To allow a saving on electronics, they were operated in a mode which electronically grouped the wires in pairs, effectively reducing the resolution to 4 mm. This was achieved by summing the output from each pair of wires into an amplifier, instead of a single wire per amplifier.

A pulse, induced on a wire by a charged particle traversing the chamber, was stretched out to last 800 ns as a logic pulse. If the external trigger electronics determined that a particle of interest had passed by, a strobe pulse was sent to transfer all signal pulses into latches. Data input was then inhibited while the latches were read sequentially. There was a one-to-one relationship between the latches and wire pairs, so that a set latch identified the fired wire and MWPC. Once the reading was finished, an external reset re-enabled the MWPC system. Readout of a typical event involved a dead time of about 5 msec, with the MWPC's having a memory time (the time in which the particle's ion track remained in the chamber) of about 150 ns, so that the rate limit on

the MWPC's was about  $10^6 \text{ sec}^{-1}$ .

The MWPC's used the "magic"<sup>28</sup> gas mixture of approximately 50 % argon, bubbled through methylal, 0.4 % argon-freon 13B1, and 46 % isobutane. This mixture has the property that the ions from the charged particle track diffuse to the nearest wire within 2 mm.

The MWPC's (Fig 14) covered one metre square in area and consisted of 20  $\mu\text{m}$  sense wires sandwiched between high tension (HT) plane wires of 122  $\mu\text{m}$  thick.

#### III.4 APPARATUS FOR THE EFFICIENCY MEASUREMENT

As previously discussed, the calibration of the neutron detector was achieved via the conjugate particle technique. For this an additional proton telescope was required to supplement the neutron detector.

The proton telescope is shown in Fig 15, and was composed of three scintillators, with copper plates between the last two. The scintillator dimensions and placements were chosen to ensure that the conjugate neutrons passed through the neutron detector. The dimensions are listed in Table 5. The reasons for these choices are discussed later in the text.

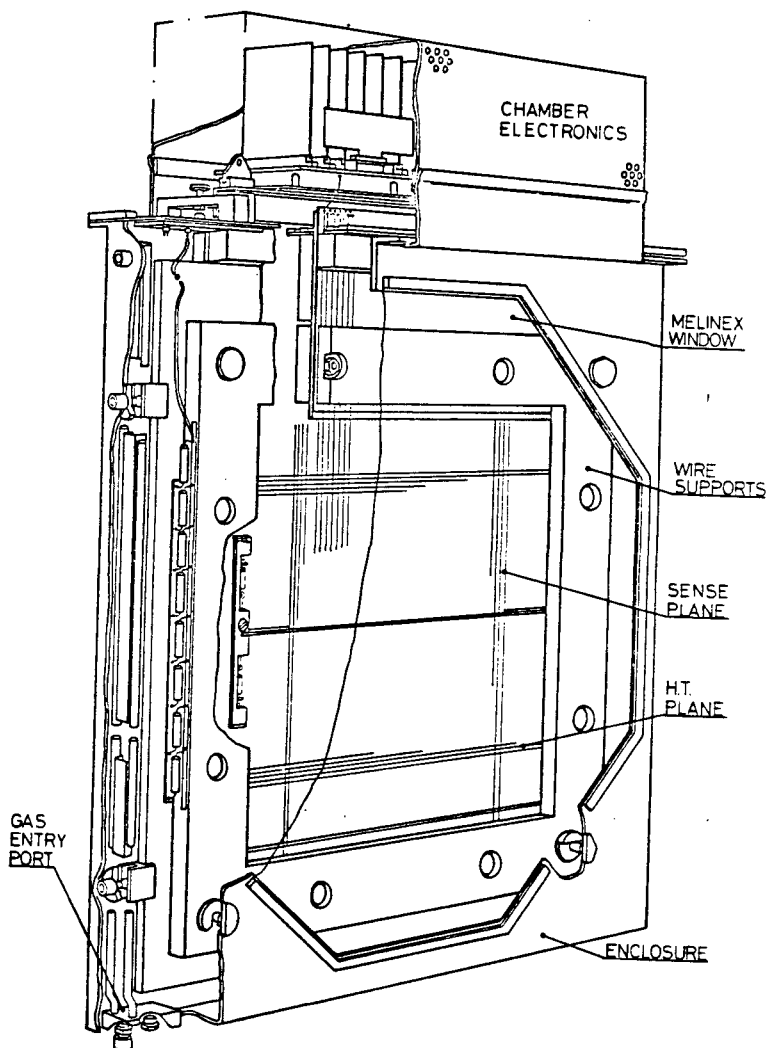


Fig 14. Multi-wire proportional chambers.  
The MWPC's were composed of sense wires sandwiched between two HT planes. The "magic" gas mixture was enclosed in the chamber by mylar windows and continuously circulated.

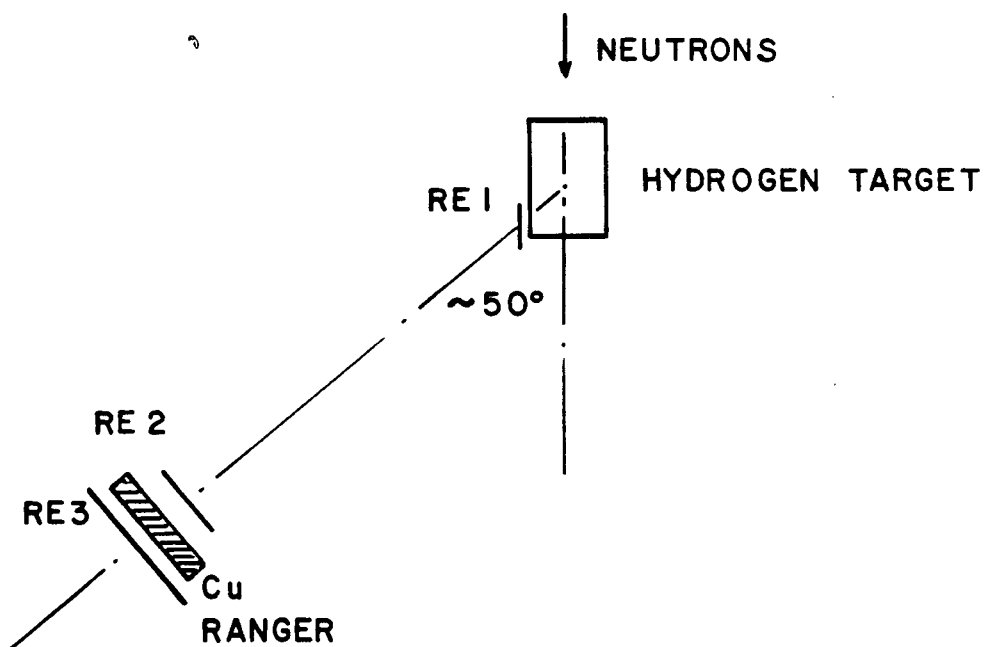


Fig 15. The recoil proton telescope.

The recoil protons in the elastic n-p scatters were observed in a three counter telescope. Low energy particles and pions were eliminated by copper ranger between RE2 and RE3.

Counter	Height (cm)	Width (cm)	Thickness (cm)
RE1	6.0	6.0	0.32
RE2	15.2	15.2	0.32
RE3	20.3	20.3	1.11

counters. Table 5. Dimensions of the recoil arm

### III.6 THE PROTON DETECTOR

Protons were detected for the measurement of the backward hemisphere of the differential cross section. The principal difficulty lies in particle identification: there is a variety of charged particles, protons, pions and deuterons, which can trigger the detector. Identification cannot be achieved by TOF alone - another independent kinematic quantity of the particle is necessary. This point is made clear by considering the standard relations for a relativistic particle of momentum  $p$  and mass  $m$

$$E^2 = p^2 + m^2$$

$$E = p / \beta$$

where  $\beta$  is the velocity of the particle ( $c=1$ ). The TOF method yields  $\beta$ , so that an independent measurement of  $p$  or  $E$  will determine the mass of the particle. Partly because of the equipment available to this experiment, momentum analysis was chosen for the second measure.

The magnetic spectrometer used to determine the momentum is shown in Fig 16. The frame of the spectrometer was the same as for the neutron detector, and kept the S2 counters at a radius of 2.317 m from the center of the

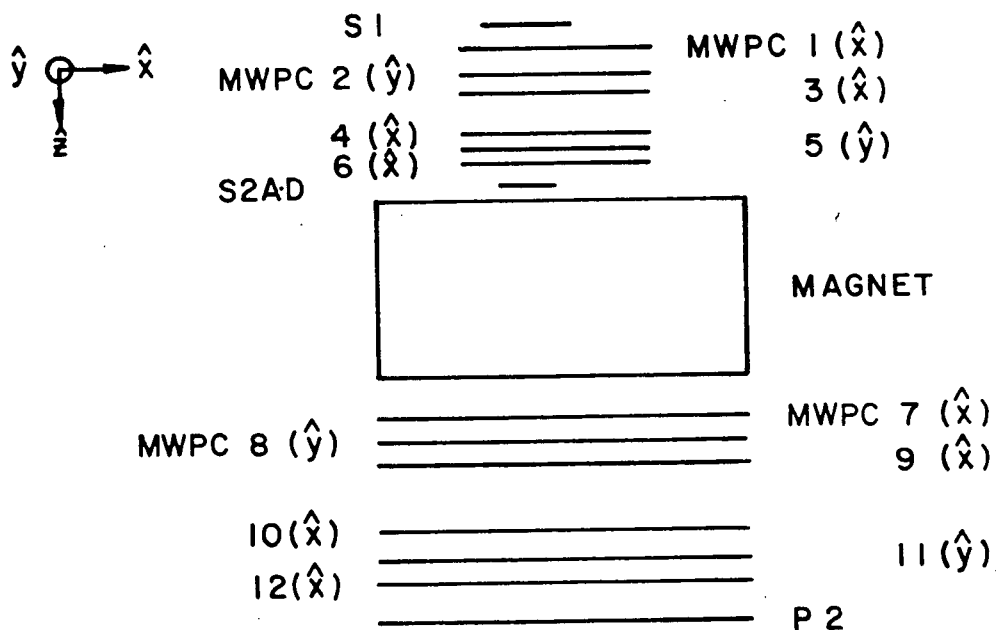


Fig 16. The proton spectrometer.

Scattered protons were detected in a spectrometer array consisting of scintillators to identify the passage of charged particles, a magnet to bend them, and MWPC's to determine the path of the particles through the system. Particle identification was made by correlating the TOF from S1 to P2 and the momentum for each particle.

liquid hydrogen target. The passage of charged particles through the detector was signalled by coincidental firings of the scintillators S1, S2 and P2. S1 and S2 are described in Table 6, while P2 is the same counter used in the neutron detector. S2 was composed of four small counters, S2 A-D, side-by-side, so that the solid angles of the angular bins defined by the counters would be determined by geometry. Six 1/2 m square MWPC's, otherwise identical to the previously described MWPC's, were used to determine the particle's track before entering the magnet, and six 1-m square MWPC's were used after it. Emphasis was placed on the particles' horizontal bend so that four of each set of six chambers were of horizontal readout. The remaining two were vertical. Ideally, the vertical component of the tracks would be unaffected by the vertical field. This was later verified in the analysis of the data.

In order to allow a greater bend through the spectrometer, the front scintillators and the magnet were offset to the right in the detector. The magnet had a 10 cm pole gap, with the pole faces of 50 cm diameter. The  $\int B \cdot dl$  was linear in the exciting current and was equal to 480.16 kG-cm at 1150 amps.

A thick scintillator, S4, was installed on the

Counter (cm)	Height (cm)	Width (cm)	Thickness (cm)
S1	25.0	25.0	0.30
S2 A-D	4.0	3.75	0.20
P2 A-F	74.4	36.5	0.30
P2 G-H	100.0	15.0	0.32
S4	10.0	15.0	10.0

Table 6. Dimensions of the spectrometer scintillators.

spectrometer, which could be inserted immediately downstream of the S2 counters. S4 was used at large angles where inelastic proton production was kinematically prohibited and the elastically scattered protons had typically less than about 100 MeV. In these cases, the use of S4 eliminated the additional loss of protons in the materials in the spectrometer downstream of S2. The scintillator was 10 x 10 x 15 cm<sup>3</sup>. When not in use, S4 was slid to the side of the spectrometer frame.

It was important that the detection efficiency of the spectrometer be as close to unity as possible. The efficiencies of the individual scintillators were estimated by measuring the number of coincidences recorded by two counters on either side of the scintillator in question, and comparing that number to the number of three-fold coincidences. The efficiencies were optimized to a level of better than 99.9% by adjusting the HT's of the scintillators.

A similar procedure was carried out for the MWPCs, using the scintillator trigger to determine the passage of charged particles through the chambers. By adjusting the MWPC HT's, typical efficiencies of about 99% were obtained. Due to the redundancy of the horizontal coordinate chambers, the expected fitting efficiency with

such individual efficiencies was virtually 100%, so that un-fit events were probably due to bad triggers, e.g. random coincidences in the scintillators.

### III.7 ELECTRONICS

The passage of particles of interest through the various detectors ("events") was signalled by fast electronic logic devices. The experiment was controlled by a PDP 11/34 computer, which communicated with the fast electronics through a CAMAC interface.

An event triggered the computer by the fast electronics sending a pulse to (strobing) an EG&G C212 bit pattern unit, which sent a Look-At-Me (LAM) interrupt to the computer. This interrupt caused the computer to inhibit the CAMAC and MWPC systems from recording further, and to proceed to record data for that event stored by the MWPC's, digital counters (scalers), time-to-digital converters (TDC's), analogue-to-digital converters (ADC's), and the C212 bit pattern unit. The C212 also recorded the firing pattern of all non-monitor scintillators. These data were transferred to 800 BPI magnetic tapes, and then used to form on-line histograms, which enabled experimenters to monitor the data as it was

being taken. These were viewable on either a Decwriter II hardcopy terminal or a Tektronix 4010 graphics terminal.

The CAMAC system was composed of two crates on a single branch. The first crate contained the C212, scalers, TDC's and ADC's, while the second contained the MWPC interfaces and a test controller (used to check the MWPC system).

As the electronics configurations for the three measurements were very similar, they will be described together. The logic devices used were NIM standard, and their configurations are shown in Fig 17-Fig 20.

Random coincidences in the various detectors were measured by utilizing the periodic RF structure of the cyclotron. The probability of detecting particles in any beam burst is assumed to be equal. Therefore, the coincidence rate of a count in a detector with a count in a subsequent burst would be a measure of the coincidence rate in a single burst.

It should be noted that the discriminator used for the monitor veto, CV, was used in the burst guard mode, in which the logic output pulse was extended until the input analogue pulse fell below the threshold level. This ensured that, for high rate conditions, multiple pulses in

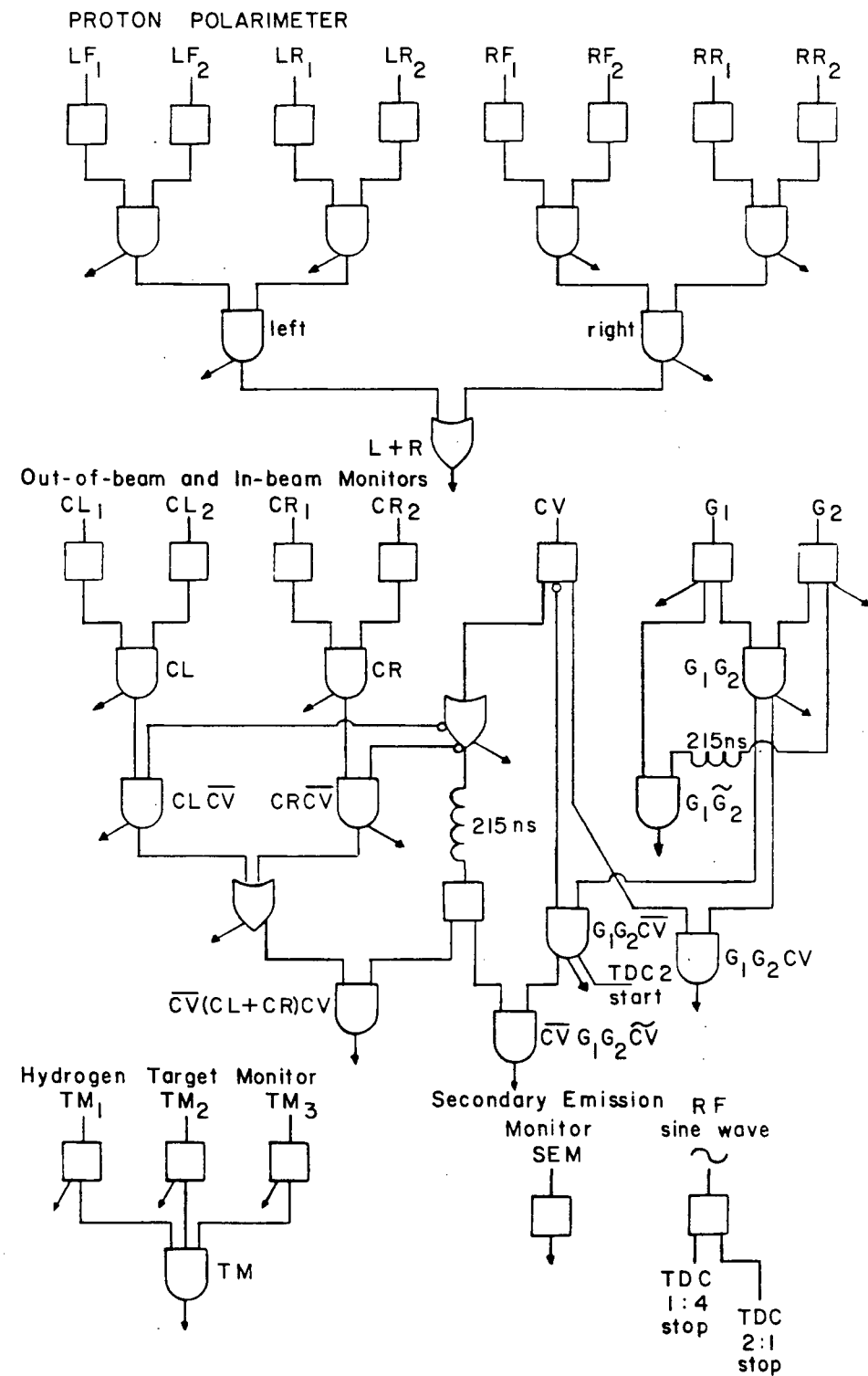


Fig 17. Electronics for the neutron monitors.  
See Fig 19 for the legend.

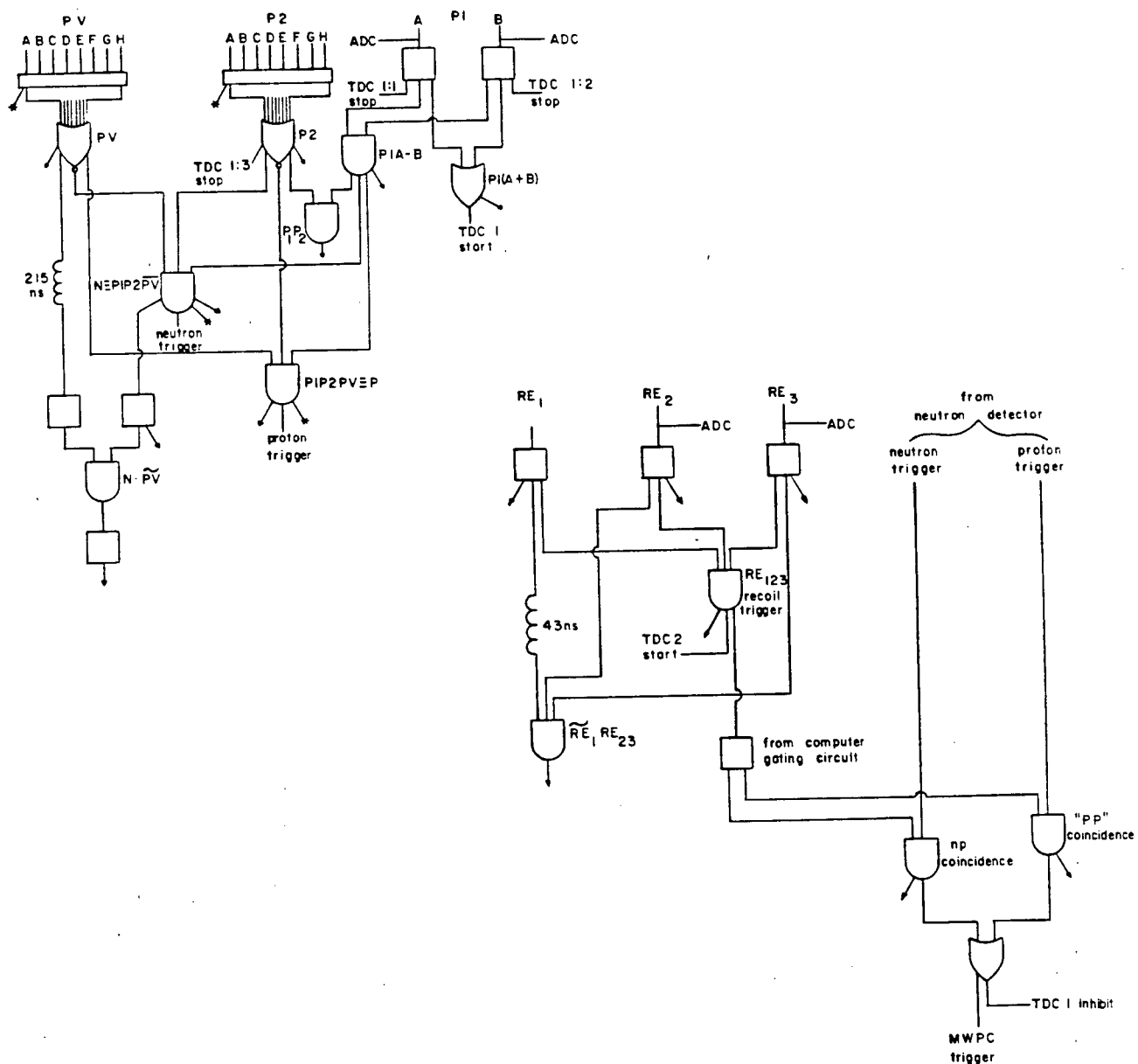


Fig 18. Electronics for the neutron detector.  
 Electronics for the recoil arm, when used in the calibration measurement are also shown. See Fig 19 for the legend.

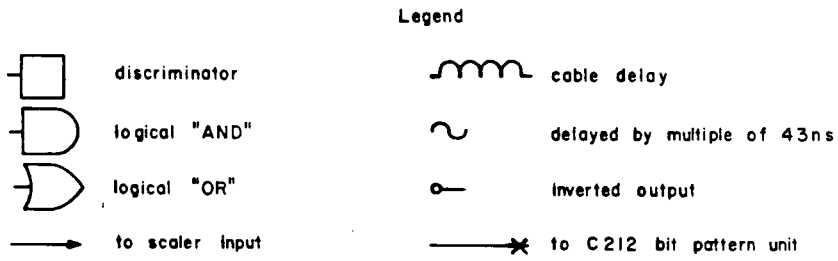
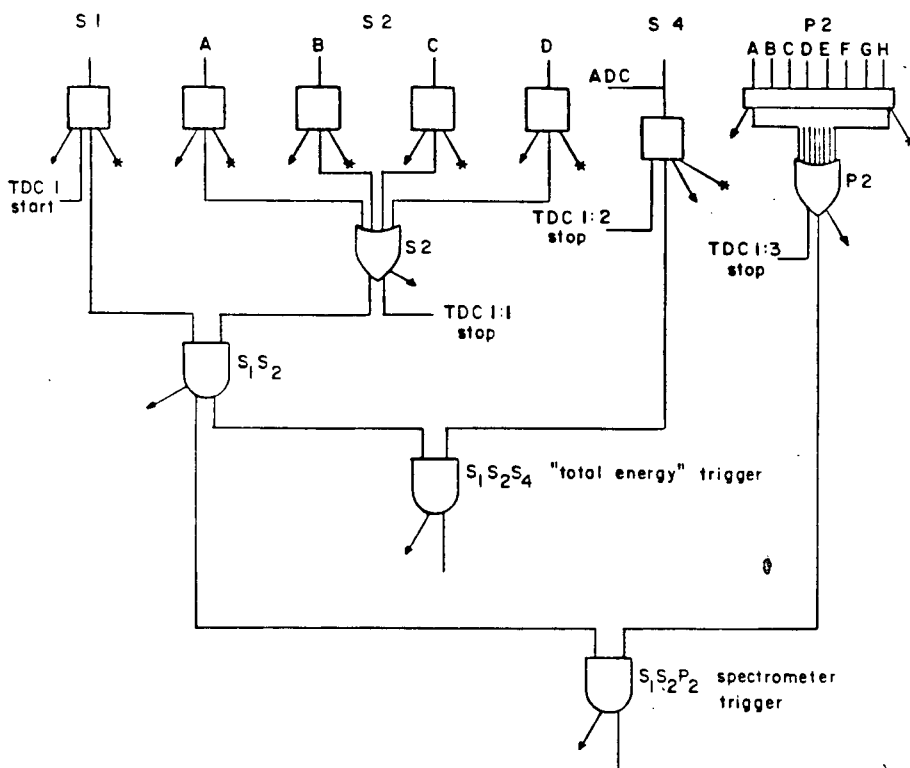


Fig 19. Electronics for the proton spectrometer.

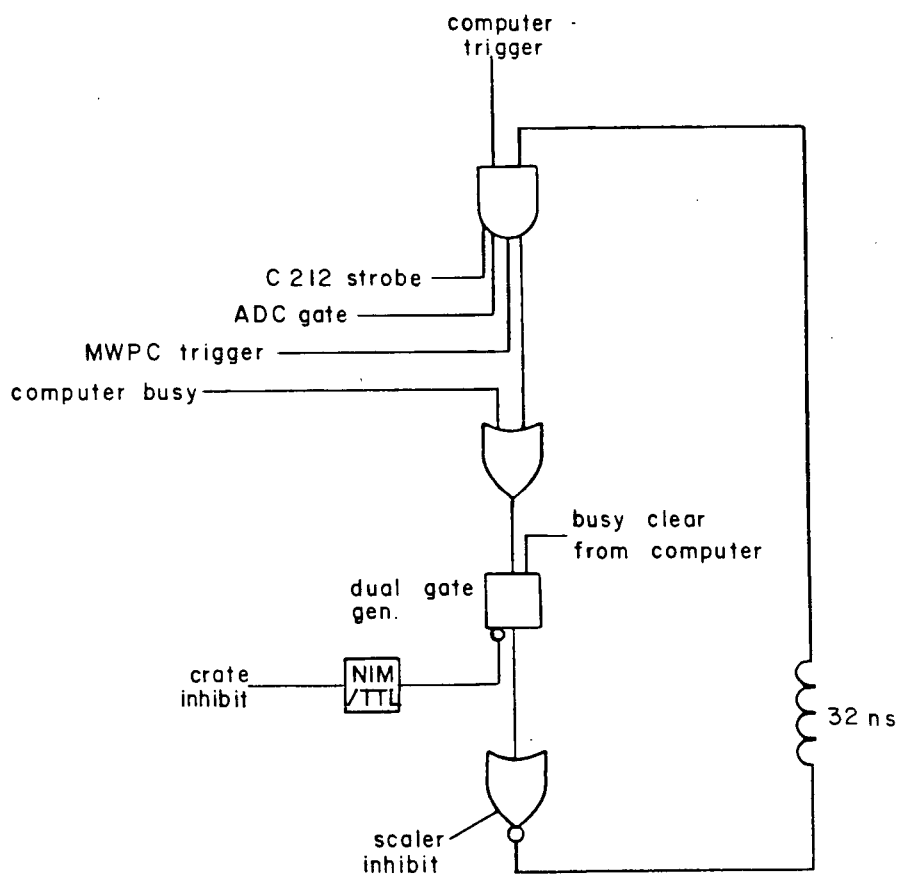


Fig 20. Electronics for the computer gating and event readout.  
See Fig 19 for the legend.

the counter would be properly vetoed.

All threshold levels were set to -100 mV and logic pulse lengths less than 43 ns were used to ensure that pulses from one beam burst could not overlap pulses due to an adjacent burst.

#### IV. ANALYSIS AND RESULTS

Analysis of the data breaks naturally into three categories: the calibration of the neutron detector and monitor; the forward hemisphere data, taken with the neutron detector; and the backward hemisphere data, taken with the proton spectrometer.

The data analysis consisted of taking the required information stored on data tapes, recorded during the experimental runs, for each event and reducing it to obtain the differential cross section. The necessary computations were performed on the University of British Columbia Amdahl 470/V6.

##### IV.1 ANALYSIS OF NEUTRON COUNTER DATA

As both the calibration and the forward hemisphere data were taken with essentially the same equipment, much of their description is necessarily similar.



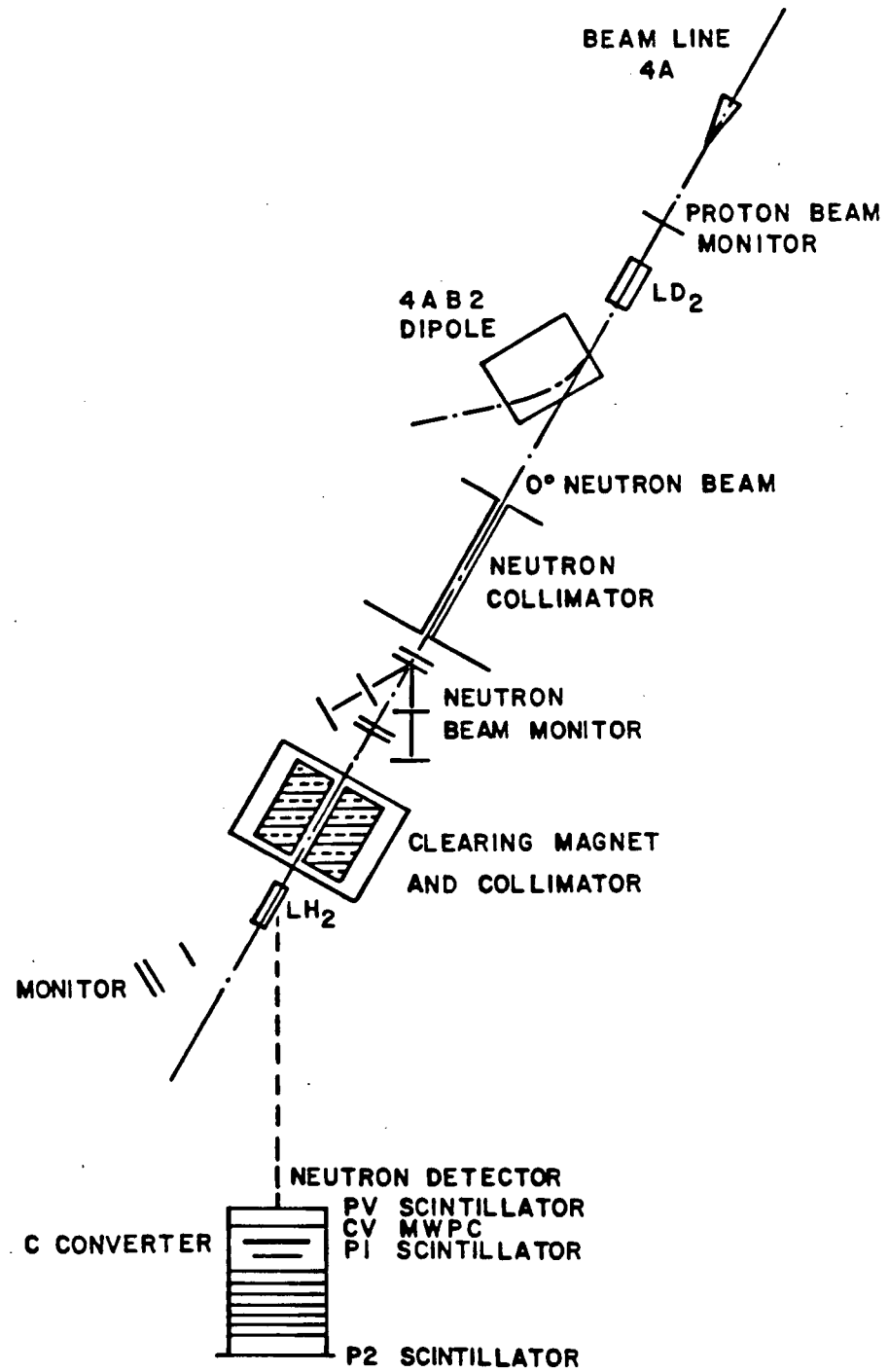


Fig 21. Measurement of the forward hemisphere of the differential cross section. Forward scattered neutrons were detected in this measurement.

this task were two time of flight spectra, and the MWPC track fitting capability.

#### IV. 1. 1. 1 Time Of Flight

This technique is used to determine the energy of a particle from the time it takes to traverse a known distance. One has that

$$\Delta t = \frac{s}{0.3\beta}$$

where  $s$  is the distance (in metres),  $\Delta t$  is the transit time (in ns), and  $\beta$  is the velocity of the particle. Fig 22 shows a plot of  $\frac{d(\Delta t)}{dT}$ , the change in  $\Delta t$  with kinetic energy, evaluated for protons, showing that as  $T$  increases, the resolution of the time of flight (TOF) method decreases rapidly. For example, at 200 MeV, a width of  $\pm 1$  ns, over a distance of 10 m, corresponds to an energy spread of 18 MeV, while at 500 MeV, the spread is 89 MeV, a change in resolution of from 9 to 18%. At these energies, TOF is clearly not a high resolution technique.

As mentioned previously, it was possible to time the arrival of the events to the cyclotron RF signal. This essentially gave the total transit time for the neutron to travel from the  $LD_2$  target to the detector. It is this

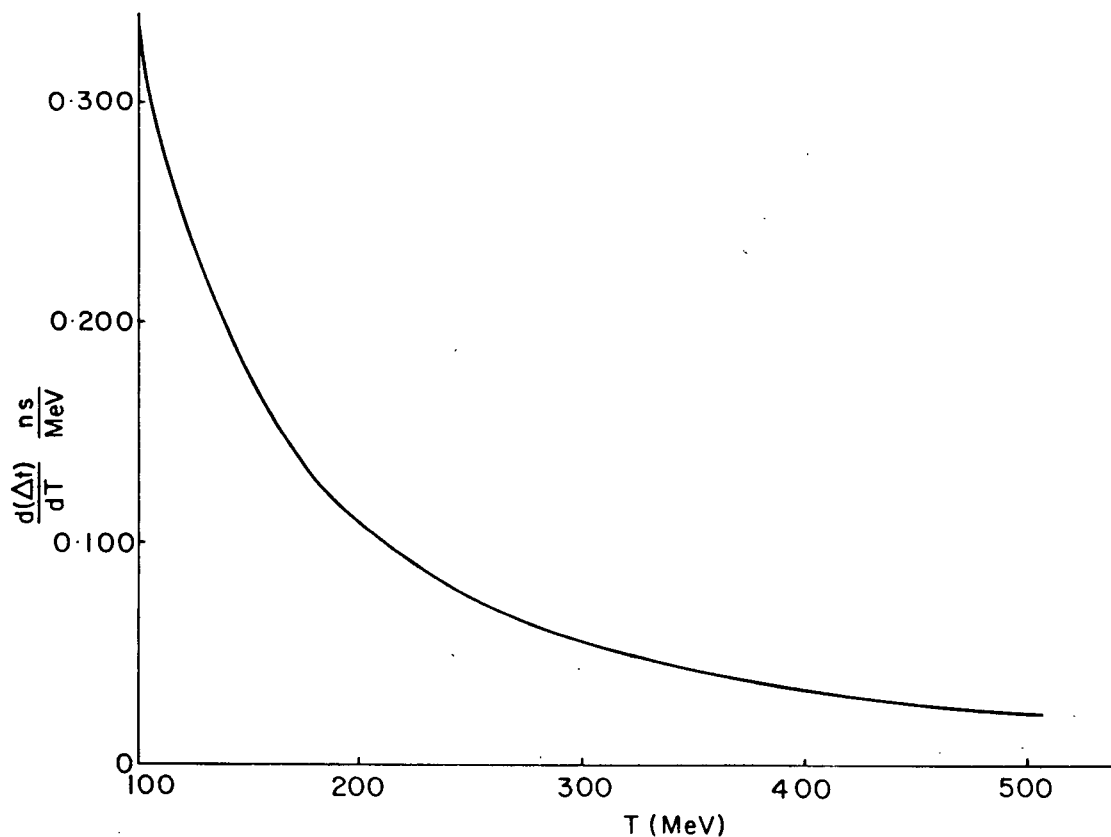


Fig 22. Resolution of the time of flight measurement as a function of kinetic energy. The resolution increases rapidly with decreasing kinetic energy, changing by more than a factor of six over the energy range of 100 to 500 MeV in which the detector accepted neutrons.

quantity which was used to eliminate neutral particles from background processes (1) and (2). Fig 23 shows the calculated time difference between elastically scattered neutrons and the most energetic inelastic neutrons possible, as a function of scattering angle. This illustrates that the inelastics are well separated in time, and, as is shown later, pose no problem.

The  $\gamma$  rays of process (2) can be eliminated in a similar fashion, since they travel so much more quickly than the elastic neutrons. Fig 23 shows the time difference between these two sources of events also.

A possible source of background was rescattering of neutrons from the floor and air into the neutron detector. A steel bar was placed between the hydrogen target and the detector to absorb almost all the neutrons coming directly from the target. All recorded events were then due to non-target associated sources. A contribution to these events from rescattered neutrons that had come from the liquid hydrogen would show up in a difference between target full and empty rates. A measurement of this effect yielded a null result, and so it was neglected in the analysis of of the data.

The 43 ns period of the cyclotron introduced another

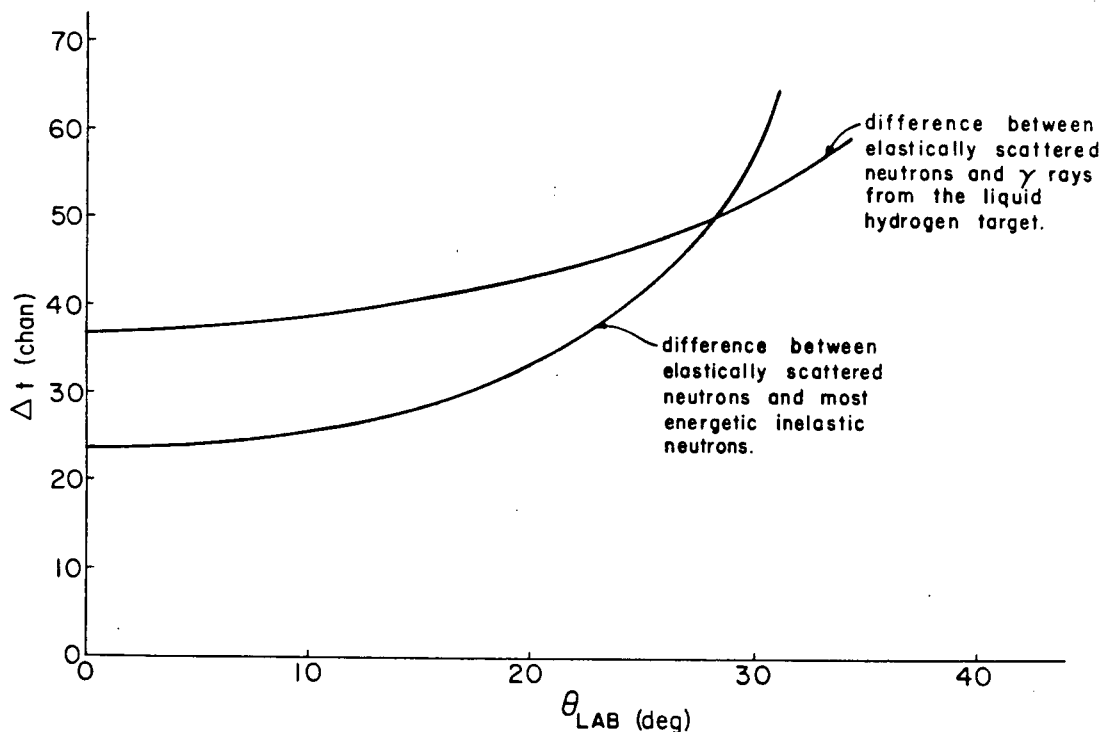


Fig 23. Time difference between elastically scattered neutrons and backgrounds.

The calculated time difference between elastically scattered neutrons and  $\gamma$  rays from the  $LH_2$  target shows that they are separable at all angles (ignoring the resolution of the TOF system and energy distribution of the beam). Separation of elastics and inelastics should be clean above  $20^\circ$  and good below. The contamination levels are discussed in the text.

source of background to the measurement. As discussed previously, neutral particles arriving at the detector a multiple of 43 ns after the elastic neutrons would be indistinguishable from the elastics. The 1:5 selector was used to investigate this background, with the result that no statistically significant contamination of the elastic neutron peak resulted from this low energy background.

The second piece of TOF information was the time required for the converted charged particles to travel from P1 to P2. A typical plot of the P1-P2 TOF is shown in Fig 24. The smaller peak in the plot corresponds to backward going particles through the detector, allowing the elimination of those backward going cosmons which triggered it. A narrow peak was found in the backward region of the P1-P2 TOF spectrum, which was attributed to electronic reflections, though this was never fully verified. All of these "backward" going particles were cleanly eliminated by applying a cut, discarding all the events in the smaller peak of the P1-P2 TOF plot. It was found that the number of elastic neutrons remaining was insensitive to this cut.

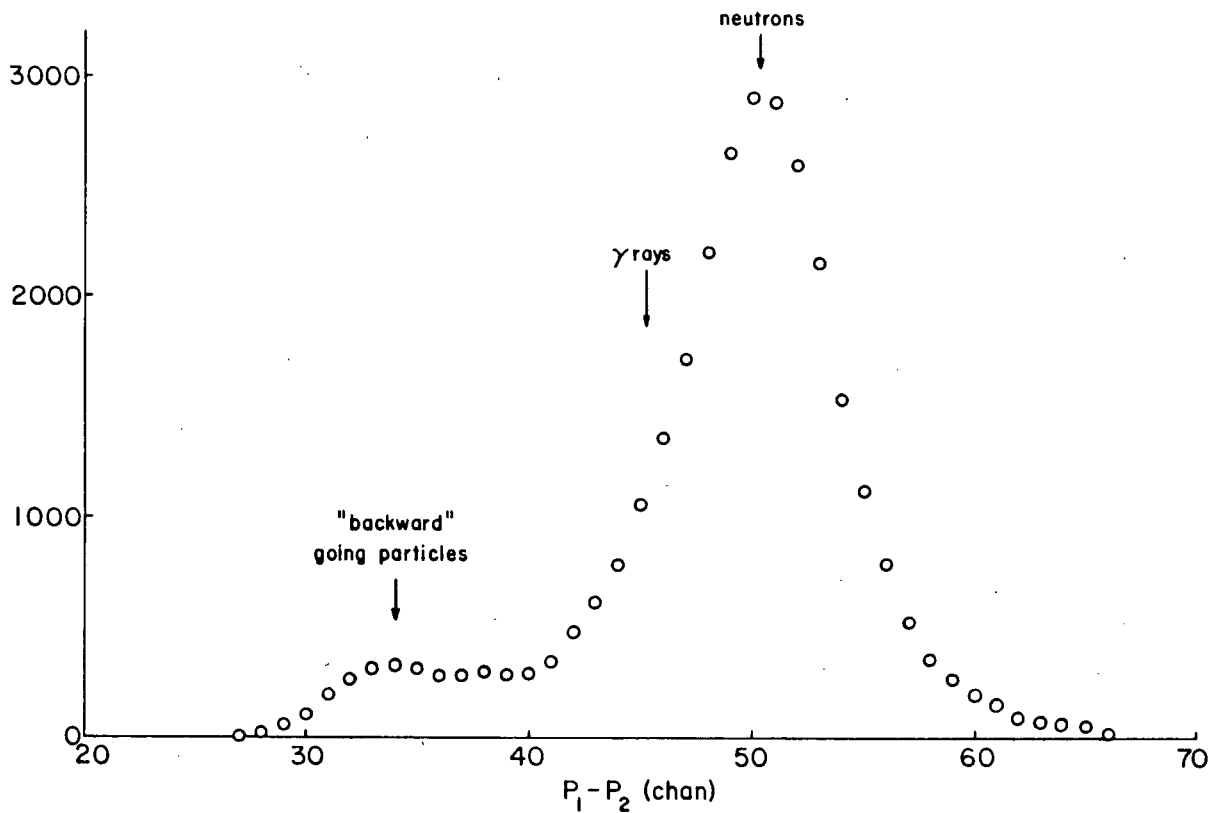


Fig 24. Time of flight of charged particles through the neutron detector.  
 A cut was applied near channel 40 to eliminate "backward" going particles. The yield of elastic neutrons was insensitive to reasonable variations of the cut.

#### IV. 1. 1. 2 MWPC Track Fitting

The procedure used to determine the charged particle tracks through the detector is described in some detail in Appendix A. The primary uses of the track information were to identify the position of the interaction in the carbon, and the angle of the track on exit from the carbon.

The MWPC's were used to define a "fiducial" region of the carbon converter. This requirement was made to eliminate any effects that might occur towards the edges. As an example, the probability of rescattering in the converter was on the order of 10%. Therefore, at the edges, neutrons rescattering towards the center of the detector would stand a much better chance of triggering the detector, while those rescattering away from the center would be lost, causing a drop in the detector's efficiency at the edges. The fiducial region was (somewhat arbitrarily) defined to be 40 cms square, removing 6.5 cm from all edges.

From purely geometrical considerations, it can be seen that the efficiency of detection varies across the face of the carbon converter. The solid angle subtended by P2 from any point on the converter is not constant. In

addition, the angular distribution of charged particles observed in n-C<sup>12</sup> scattering peaks near 20° lab, so that neutrons interacting in the center of the carbon would be more likely to trigger P2 than those at the edges.

The differential cross section is independent of the azimuthal scattering angle,  $\phi$ , so that, to a good approximation, for  $\theta > 50^\circ$ , the distribution of events originating from the converter should be uniform in the vertical direction, and should reflect itself in a flat profile of events, binned in horizontal strips. Any deviation from flatness indicates a variation in the efficiency, either due to geometry or equipmental bias. Such a profile is shown in Fig 25, and shows distinct drops towards the edges of the carbon. Only a central fiducial region of the carbon is shown, to eliminate edge effects. The profile reflects the geometrical drop-off in efficiency.

A cut was made on the exit track angle of the scattered track, so that all events accepted at the converter would have an equal chance of triggering P2, regardless of their point of origin within the fiducial region of the carbon. The choice of the maximum angle was determined by the geometry of the converter and P2, as shown in Fig 26, and was set to 17°. A typical vertical

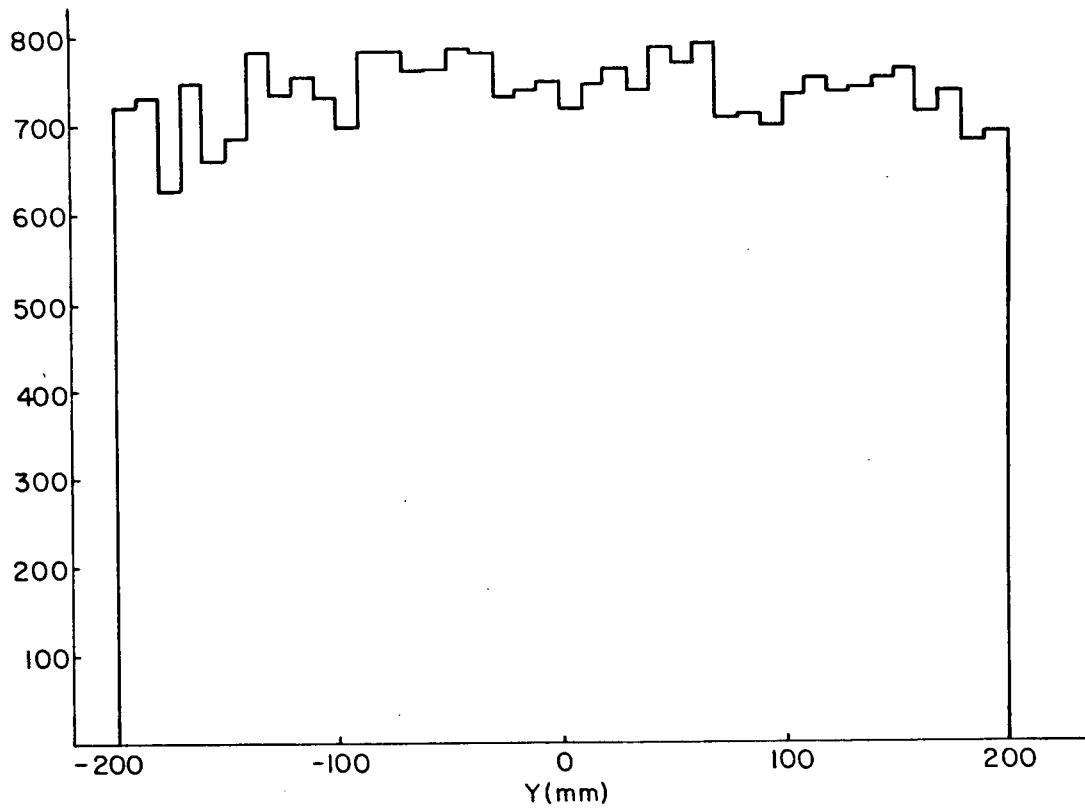


Fig 25. Vertical profile of events from the carbon converter with no exit track angle cut.  
The effect of the change of solid angle subtended by P2 from points on the converter is illustrated by the falling profile away from the center.

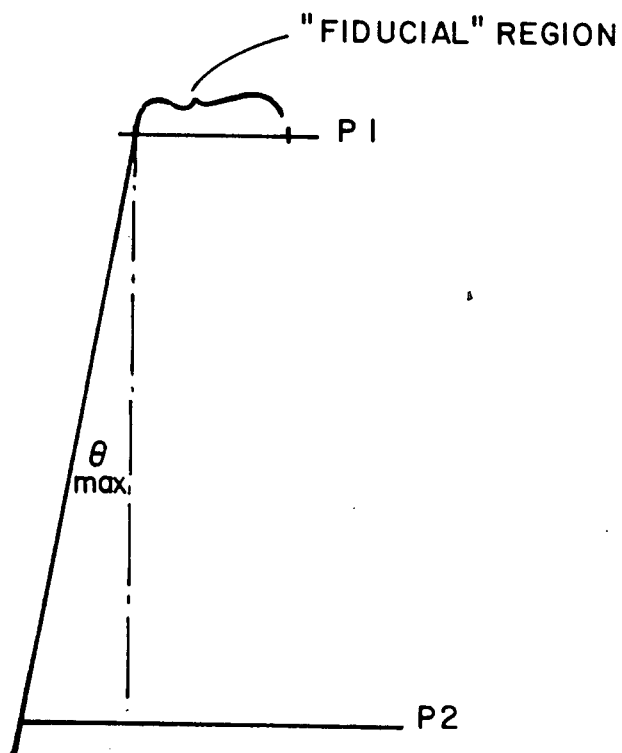


Fig 26. Determination of the maximum allowable exit track angle from the converter.  
The maximum angle was determined by the size of the "fiducial" region used on the carbon and the size of P2. The maximum angle chosen was  $17^\circ$ .

profile, incorporating this cut, is shown in Fig 27. The profiles were flat, within statistics, indicating that the inefficiencies were purely geometrical, and were eliminated by this cut. Therefore, the efficiency was independent of the position of interaction on the carbon converter, within the fiducial region. It should be noted that the price paid for this cut was the loss of approximately half the recorded triggers that survived the other cuts.

The efficiency of track reconstruction was approximately 98% at non-zero angles and 99% at zero degrees. The difference was attributed to a higher rate of bad triggers at non-zero angles, which were rejected by the MWPCs. Runs in which the reconstruction efficiency varied by more than about 1% were rejected from the analysis.

As discussed in Chapter III, an MWPC was included behind PV to act as an additional veto counter. If a vertical track, extrapolated to this MWPC, came within 5 cm of a hit wire, the event was rejected. The cut was made this loose as it had been observed that protons frequently underwent small angle scatters in the carbon, so that in these cases, a tight requirement would have been ineffective.

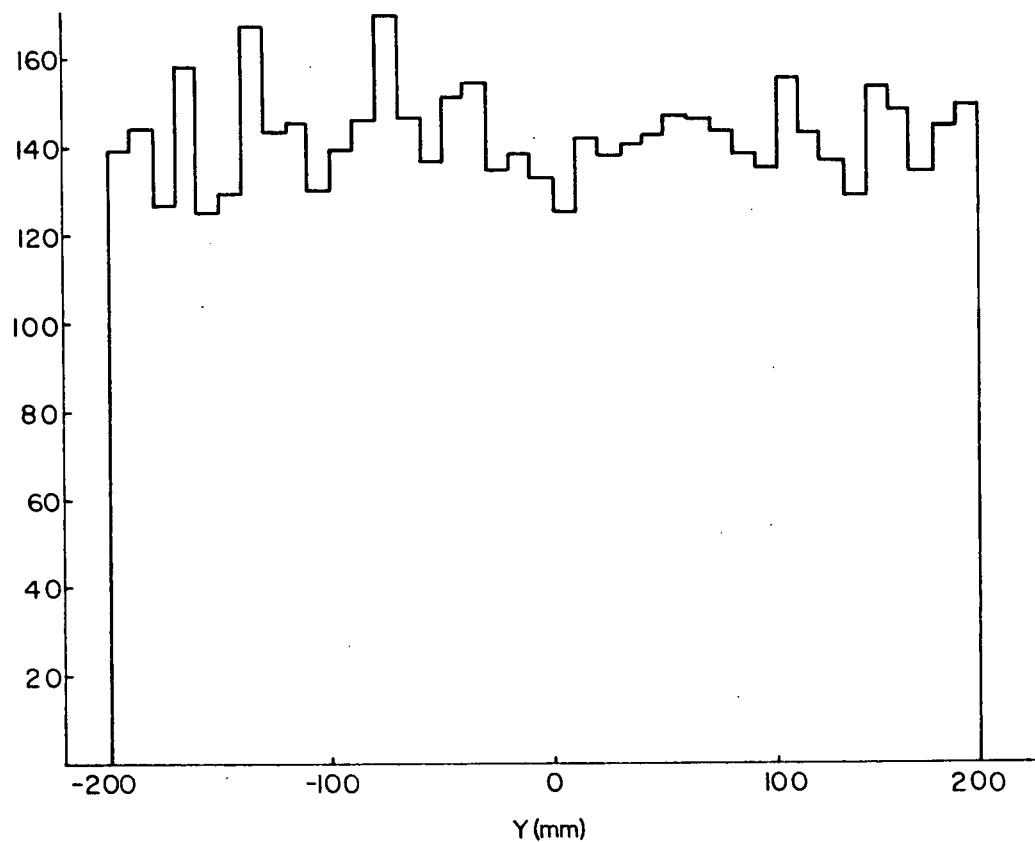


Fig 27. Vertical profile of events at the carbon with an exit track angle cut of  $17^\circ$ . With a cut of  $17^\circ$ , the profile is flat, showing that there are no geometrical or instrumental inefficiencies present in the neutron detector.

The track information was also found to be essential in the elimination of three sources of background. The (beam off) cosmic ray runs had a very low fraction of events with fitted tracks ("fitting efficiency"). Coupled with the requirements that tracks intersect the carbon and that the event not come in the "backward" region of the F1-P2 TOF spectrum, cosmic rays were, for all practical purposes, completely eliminated as a source of background. This also implied that these unfittable events were primarily due to cosmic ray showers from above, and not from particles travelling horizontally.

It was also noticed that up to 5-10% of the recorded events had no MWPC information associated with them at all. Investigations of the TOF and pulse height information for these events showed that they appeared to be  $\gamma$  rays that were uniformly distributed in time, i.e. they showed no correlation with the arrival times of normal events. It was felt that they were perhaps due to thermal neutrons being captured in the carbon and releasing low energy  $\gamma$  rays, which were incapable of triggering the MWPC's. These events were discarded.

The requirement that an event have a track fit was also strong protection against random coincidences of the

P1 and P2 counters.

#### IV. 1.2 The Neutron Beam

When the experiment began, it was found that background coming from sources other than liquid hydrogen was too severe. These sources were traced to insufficient secondary collimation of the incident neutron beam. Too many neutrons were scattering from the main collimator and monitors and causing a high background rate by rescattering from the aluminium target assembly. A secondary collimator was designed and placed inside the sweep magnet. Fig 28 shows profiles of the neutron beam in the horizontal and vertical directions. The profiles were obtained by placing the neutron detector in the neutron beam, 5.57 m downstream of the LH<sub>2</sub> target. Estimates of the beam properties at the liquid hydrogen target were obtained by geometrical extrapolation, and are shown in Table 7. The shape of the beam was not seen to change during the period of experimental running.

From other measurements on production of neutron beams using deuterium targets<sup>29</sup>, it is known that a nearly mono-energetic beam is produced, with a narrow peak of about 1% dT/T which is well separated from the lower

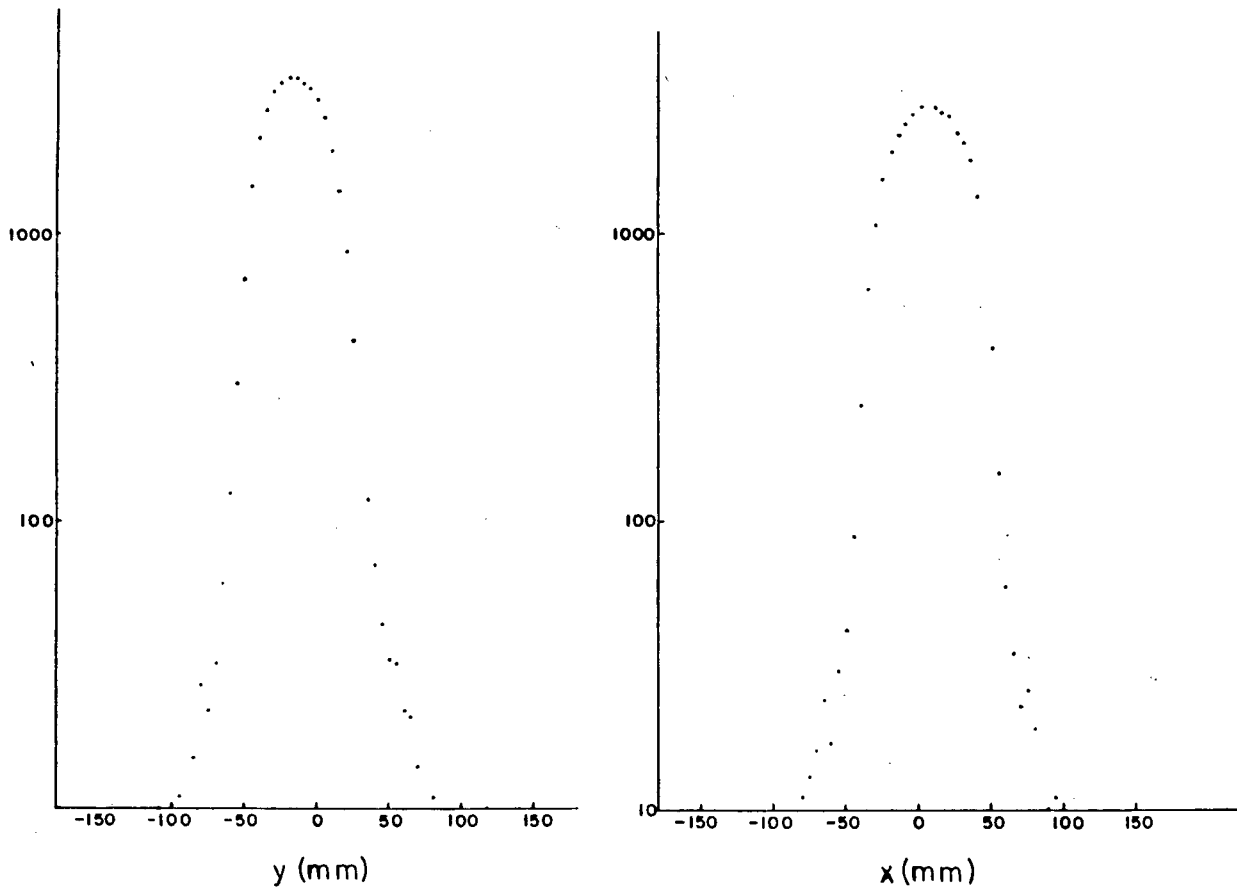


Fig 28. Vertical and horizontal profiles of the neutron beam.

Reconstructions of the horizontal and vertical distribution of events at the carbon converter, 5,57 m downstream of the LH<sub>2</sub> target are shown. The wings of the beam were at the 0.1% level 100 mm from the center of the beam. By geometrical extrapolation, this corresponds to approximately 50 mm at the target.

Proton Beam Energy (MeV)	Neutron Beam Energy (MeV)	Spatial Size FWHM (cm)	Neutron Flux (n/sec/namp)
$225 \pm 1$	$21.2 \pm 2$	2.5	8600
$429 \pm 1$	$41.8 \pm 2$	2.5	6200

Table 7. Neutron beam properties.

energy tail. The TOF measurement is insufficiently precise to check these properties on the neutron beam used in this experiment.

The average energy of the neutron beam was estimated by accounting for energy loss of the primary proton beam to the center of the  $LD_2$  target, the 2.22 MeV binding energy of the deuteron, and an estimate of the energy taken up by the spectator proton in the deuteron. This was done by calculating the average momentum using Hulthen's form of the deuteron wave function. The corresponding kinetic energy was 4.6 MeV. This was reduced by the final state interaction between the two protons, which should be less than the Fermi momentum, and greater than zero. The mean of these two values was taken.

For completeness, the neutron production rates are shown in Table 7 as well, calculated from estimates of the primary proton beam current and the absolute efficiencies of the monitors (described later in the text).

## IV.2 MEASUREMENT OF THE ABSOLUTE EFFICIENCY OF THE NEUTRON DETECTOR

### IV.2.1 Principle And Requirements Of The Measurement

The principle of this measurement is simply stated: if one has detected one of the two elastically scattered nucleons, then kinematics can be used to determine where the other member of the pair has gone. The absolute efficiency of the neutron counter can then be obtained by detecting the elastically scattered protons, and then interrogating the neutron detector as to whether a neutron had been observed (Fig 29) at the kinematically conjugate angle.

There are several complications to this ideal situation, some of which are intimately related. Put into two broad categories, they are: uncertainty of the paths of the two nucleons and possible losses; and background processes. These two categories can be dealt with separately.

Both the incident neutron beam and the LH<sub>2</sub> target

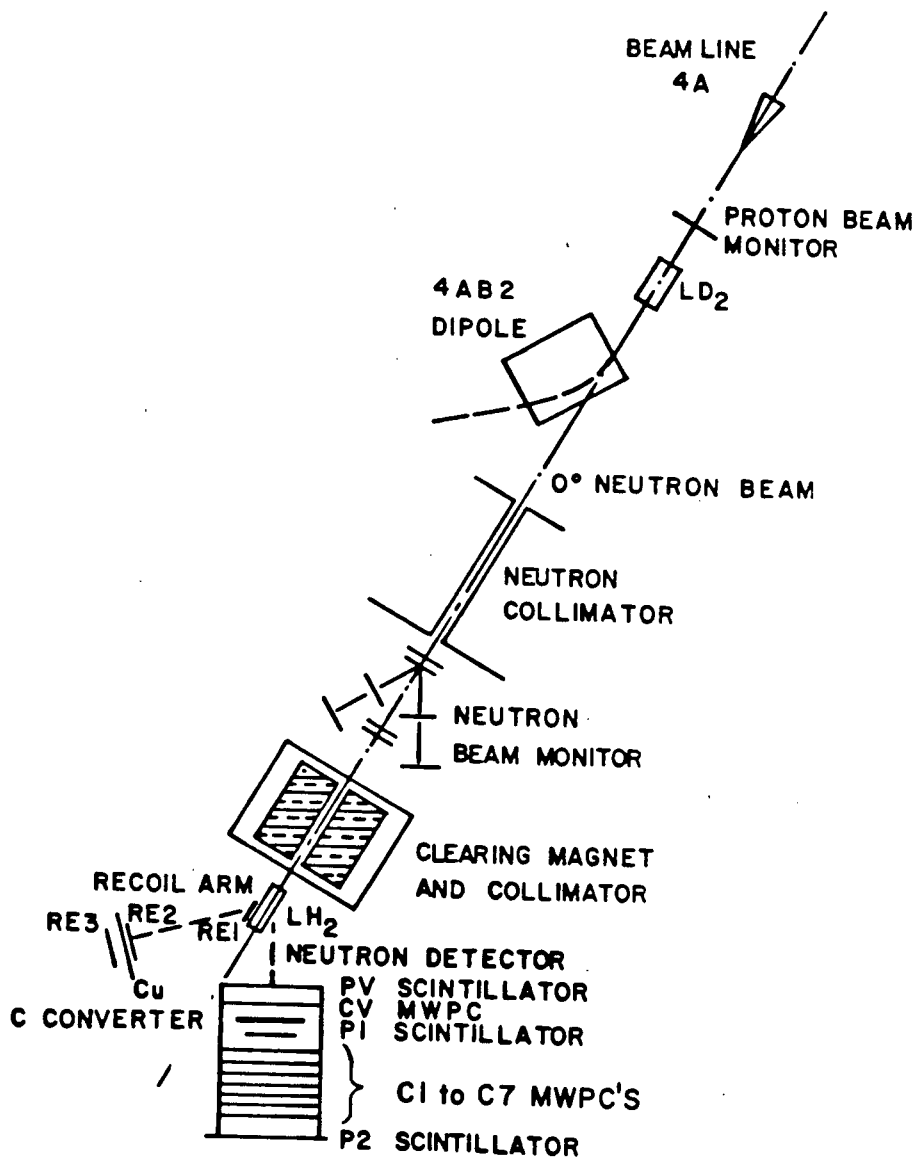


**Fig 29. Calibration of the neutron detector.**  
Elastically scattered recoil protons were observed in the recoil arm. The efficiency of the neutron detector was obtained by comparing this number of protons with the number of coincidentally observed neutrons in the neutron detector.

are of finite extent. As such, from geometry alone, there will be a considerable spreading of the "envelope" containing the scattered neutrons defined by the proton arm, as illustrated in Fig 30. This envelope is most sensitive to the length of the target, and, in fact, it was necessary to restrict the length of target from which protons were accepted by placing a small counter, R1, up against the target.

On the way to the recoil arm, the protons undergo multiple scattering after the original n-p collision, primarily in the liquid hydrogen itself, and in the aluminium surrounding the flask. As a result, the true, original, direction of the proton is obscured and, consequently, the uncertainty in the neutron direction is increased. Multiple scattering is a random process so that the amount of scatter can only be predicted to within a certain probability of occurrence.

The solution to both of these problems is to bring the neutron detector in as close to the  $\text{LH}_2$  target as possible. This must be offset by two factors: the physical size of the detector, as it is unwise to have it in the direct neutron beam; and the desire to match the running conditions as closely as possible to the data taking runs for  $d\sigma/d\Omega$ . This restricts the distribution of incoming

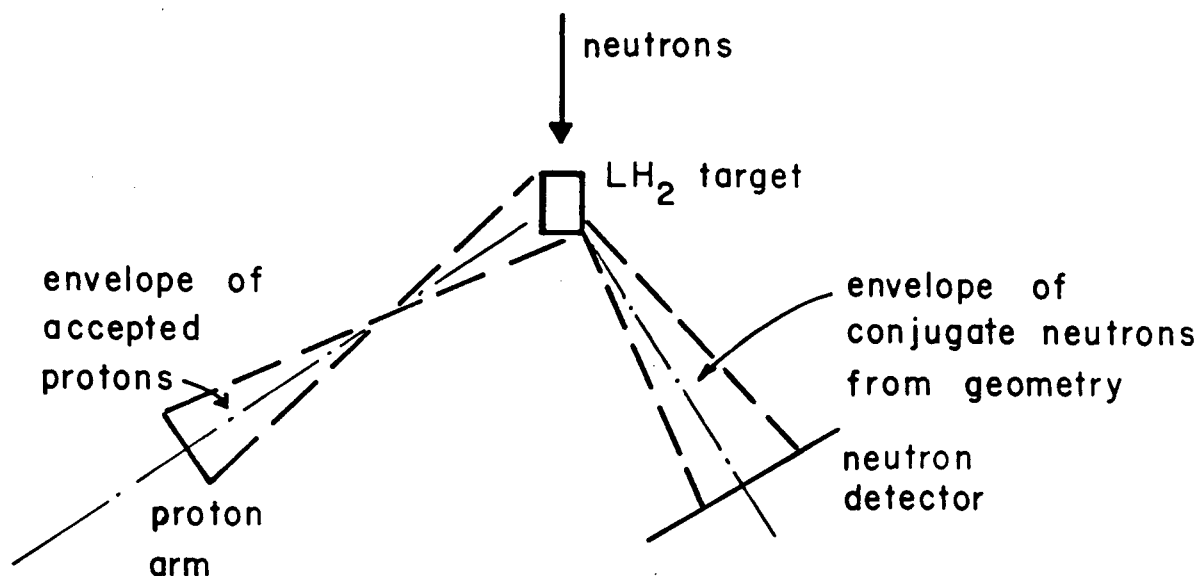


Fig 30. Envelope of accepted neutrons determined by the recoil arm.

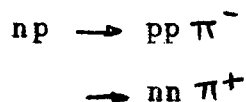
The envelope of protons accepted by the recoil arm fixes the distribution of neutrons at the neutron detector. To keep the size of the neutron "beam" at the carbon smaller than the fiducial region, the detector was moved close to the target, and the target length was restricted by a small trigger scintillator in the recoil arm up against the target.

neutrons to be approximately normally incident on the neutron detector.

The final compromise solution, satisfying these conditions, placed limits on the size of the recoil arm counters, the proximity of both detectors to the target, and the angles of scatter to be used. Table 8 describes the configurations used in the measurement.

Fig 31 shows a reconstruction of the horizontal and vertical profiles of the neutron envelope accepted at the carbon converter. It verifies that all the neutrons fell safely within the boundaries of the detector.

The second category of complications involved background processes. In the processes



The recoil arm could have been triggered by any of the charged particles. No inelastic protons from the liquid hydrogen were kinematically allowed at the angles defined by the recoil arm. Pions were eliminated by TOF. The  $\pi^-$ 's that came within the same TOF window as accepted for elastic protons were eliminated by the use of copper plates, whose thicknesses were chosen to range out the pions. The amounts of copper used for each configuration

Proton Beam Energy (MeV)	Recoil Arm Angle (deg)	Neutron Detector Angle (deg)	Copper Thickness in Recoil Arm (cm)
225	51	35	---
331	51	35	0.64
429	49	35	0.64
499	48	35	1.27
499	60	25	0.64

Table - 8. Recoil arm and neutron detector configurations.

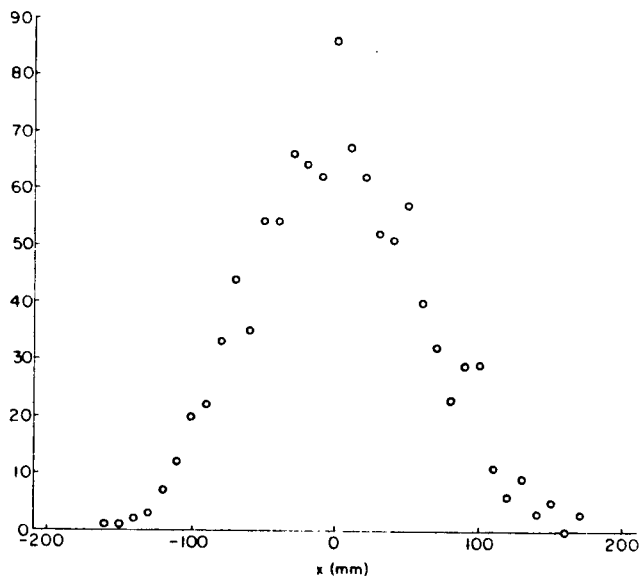
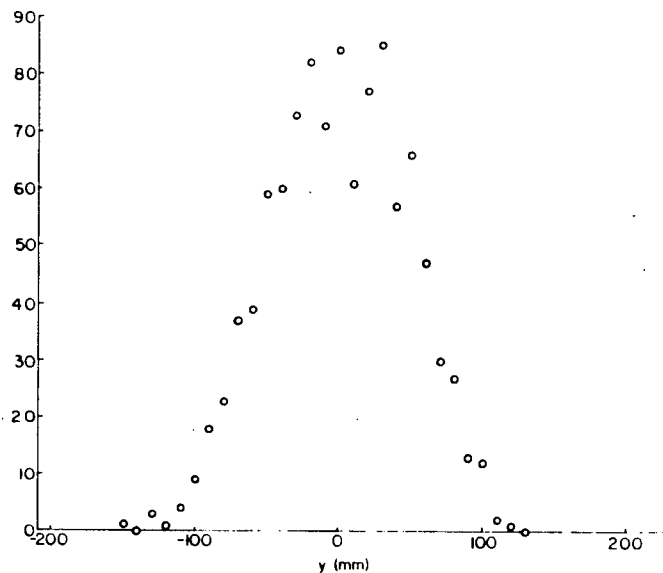


Fig 31. Horizontal and vertical profiles of neutrons at the carbon in the calibration.  
 The distribution of events across the face of the carbon converter was easily contained within the fiducial region of 40 cm square.

are also listed in Table 8.

The remaining sources of background are those not associated with the liquid hydrogen, and were primarily due to the target container. The effects of these backgrounds can be well estimated by taking data with the  $\text{LH}_2$  removed. This effect was greatly reduced by the small counter R1: the majority of possible background events, coming from the aluminium dome downstream of the flask, could not fire all three counters in the recoil arm. As a result, the "empty target" rate was typically less than 2% of the full rate.

#### IV.2.2 Data Taking

During the experimental running, an "event" occurred whenever all three scintillators in the recoil arm fired in coincidence. At such a time, the on-line computer delayed its acceptance of further events and recorded the TOF and pulse height (ADC) information. Furthermore, based on whether the neutron detector had also been triggered, it read the MWPC's and set a bit in a pattern word.

The philosophy in analyzing this data was to determine whether the TOF and ADC information verified

that the particle had indeed been an elastically scattered proton. If it had been, then the information regarding the neutron detector was investigated: if the pattern word bit had not been set, the neutron detector had missed the neutron; otherwise, the event was required to satisfy three cuts before it was classed as legitimate. The P1-P2 TOF timing was required to be in the forward region of the spectrum, a fit was required for tracks through the MWPC's giving a line intersecting the carbon converter, and the exit track polar scattering had to be less than the same limit as used in the differential cross section data.

Fig 32 shows histograms of typical TOF and ADC spectra for the recoil arm. Tight cuts were made, as shown, with the philosophy that, as long as background events were excluded, any cuts were acceptable. This was found to be the case upon varying the cuts.

After all the cuts had been made on the recoil arm and neutron detector events, the emphasis of the further analysis was to obtain the shape of the neutron detector efficiency as a function of energy for the forward hemisphere differential cross section data, and the absolute normalization of the efficiency to calibrate the neutron beam monitors.

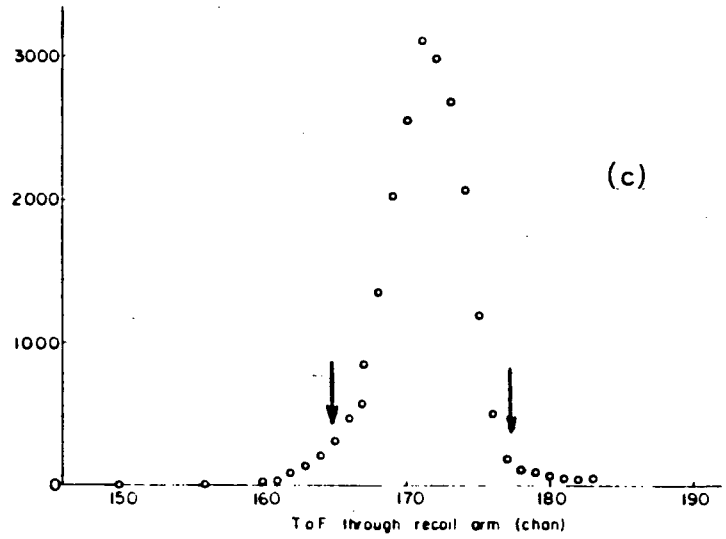
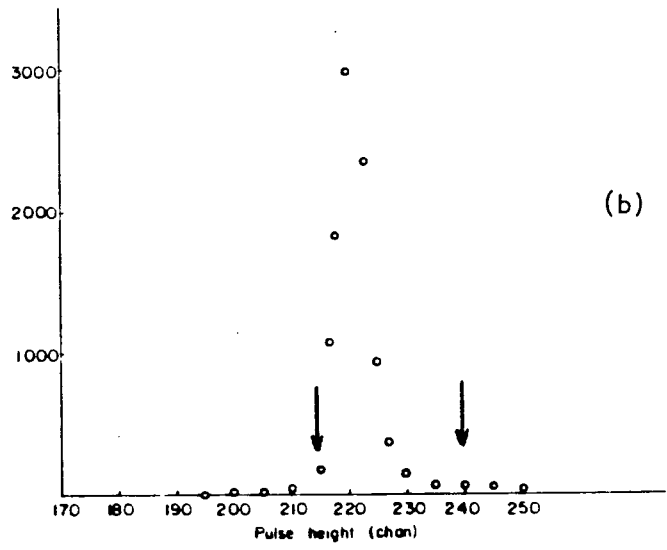
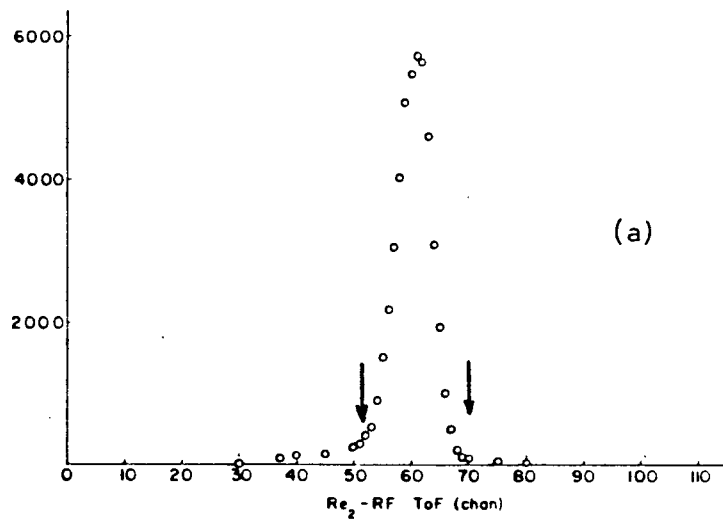


Fig 32. TOP and ADC spectra in the calibration measurement.  
 Fig(a) shows the TOP through the recoil arm. Fig(b) shows the TOP with respect to the BP, and Fig(c) shows the pulse height spectrum in RE3. The cuts applied are shown.

The data were analyzed in two ways: with no exit track angle cut and with a cut of  $17^\circ$  on the angle. The two analyses were required to check the consistency of the data and to better determine the efficiency function with the cut applied.

#### IV.2.3 Corrections To The Number Of Nucleons Incident On The Detectors

The measurement of the absolute efficiency of the neutron detector meant that a beam of neutrons was defined by the protons accepted into the recoil arm. Two effects distorted the result of the measurement: the neutrons were attenuated in the materials between the point of scatter and the detector; and the protons multiply scattered into the recoil arm such that the scattered neutrons were not necessarily directed towards the neutron detector.

Assuming that all interactions cause loss of the neutrons, the standard exponential loss calculation of

$$\exp(-n\sigma t)$$

with  $n$  the number of scattering centers/cm<sup>3</sup>,

$\sigma$  the total cross section, and

t the thickness of material

yields an attenuation of about 2% for the neutrons in approximately 0.8 g/cm<sup>3</sup> of hydrogen equivalent material, as discussed in Appendix D. This must be corrected for those neutrons which scatter forward and are still within the detector acceptance. These corrections are listed in Table 9. An error of about  $\pm 20\%$  has been assigned to the calculation of this correction due to uncertainty in the shape of the differential cross section from nuclei, fitted to existing data.

At energies above 200 MeV, the multiple scattering corrections are small, as the number of protons scattering out of the detector is approximately equal to the number scattering in. However, at lower energies, the cross section rises sharply, enhancing the number of rescatters from those protons which had originally undergone a wide angle scatter over those which had scattered more forward. This gives more protons scattering in from wider angles than scatter out from the nominal detector scattering angle.

This effect is small for forward angles, and

<u>Calibration Setting</u>	<u>Attenuation of Neutrons</u>	<u>Double Scattering of Neutrons</u>	<u>Double Scattering of Protons</u>	<u>Total Correction</u>
(Proton Beam Energy Neutron Detector Angle)	(%)	(%)	(%)	(Multiplicative)
(MeV, deg)				
(220,35)	2.6	0.44	0.59	1.036
(330,35)	2.0	0.36	0.55	1.029
(429,35)	1.8	0.41	0.68	1.029
(499,35)	1.7	0.44	0.67	1.028
(499,25)	2.0	0.16	0.21	1.023

Table 9. Multiple scattering and attenuation corrections.

The calculated values of the attenuation and multiple scattering of the neutrons on their way to the neutron detector, and of protons on their way to the recoil arm are listed as a functions of scattering angle.

approaches 1% at the wide angles. Table 9 also lists this correction to the data, and the overall correction applied.

#### IV.2.4 Analysis With No Exit Track Angle Cut

A typical histogram of the polar exit track angle from the carbon is shown in Fig 33. The efficiency with no cut on the angle was calculated by summing the entire range of this histogram, the results of which are listed in Table 10, and plotted in Fig 34. It was found that the data were well fit by a linear function of the inverse kinetic energy of the neutrons incident on the detector.

A least squares linear fit to the functional form

$$\xi'(T) = m/T + b$$

yielded the result

$$m = -4.511 \pm 0.058 \text{ (MeV)}$$

$$b = 0.03978 \pm 0.00035$$

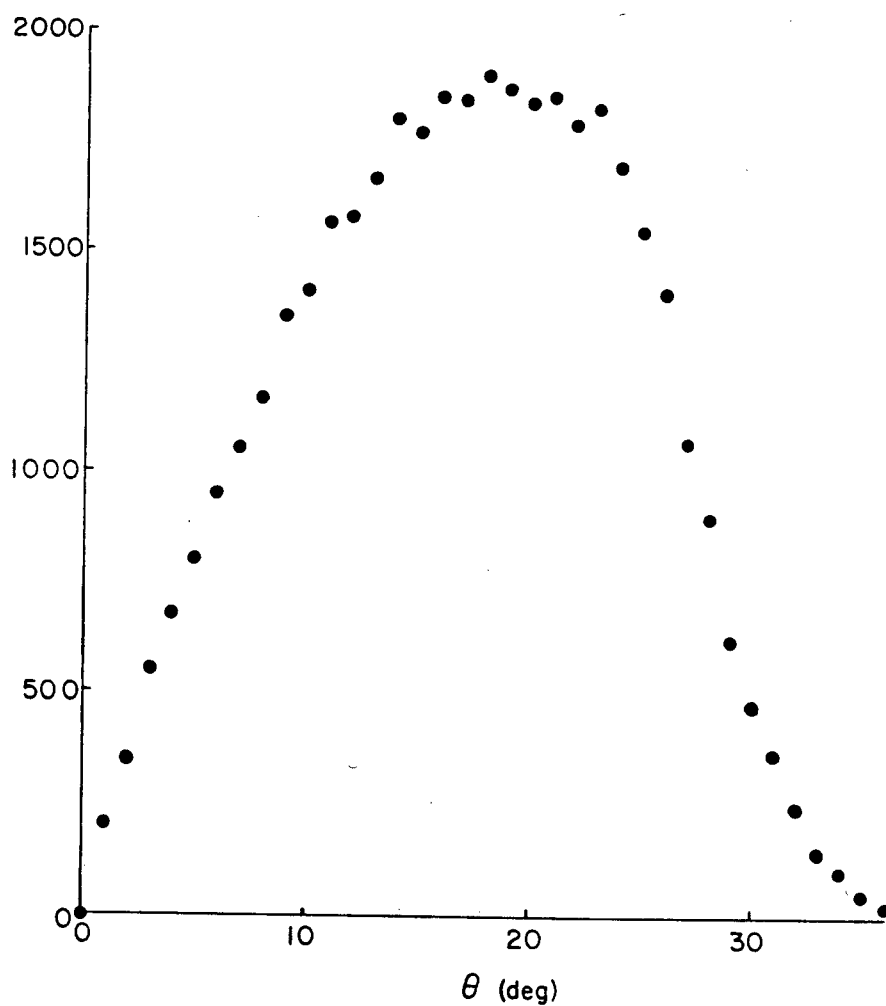


Fig 33. Exit track angle distribution.  
Neutrons incident on the carbon interacted to produce charged particles which scattered according to this distribution, as measured by the MWPCs.

Neutron Energy Incident on the Detector  (MeV)	Efficiency  $\epsilon'$ (T)
384.5	0.0278 $\pm$ 0.0004
302.8	0.0252 $\pm$ 0.0003
261.3	0.0224 $\pm$ 0.0003
203.3	0.0176 $\pm$ 0.0004
137.2	0.00692 $\pm$ 0.00014

Table 10. Neutron detector efficiencies  
without exit track cuts.

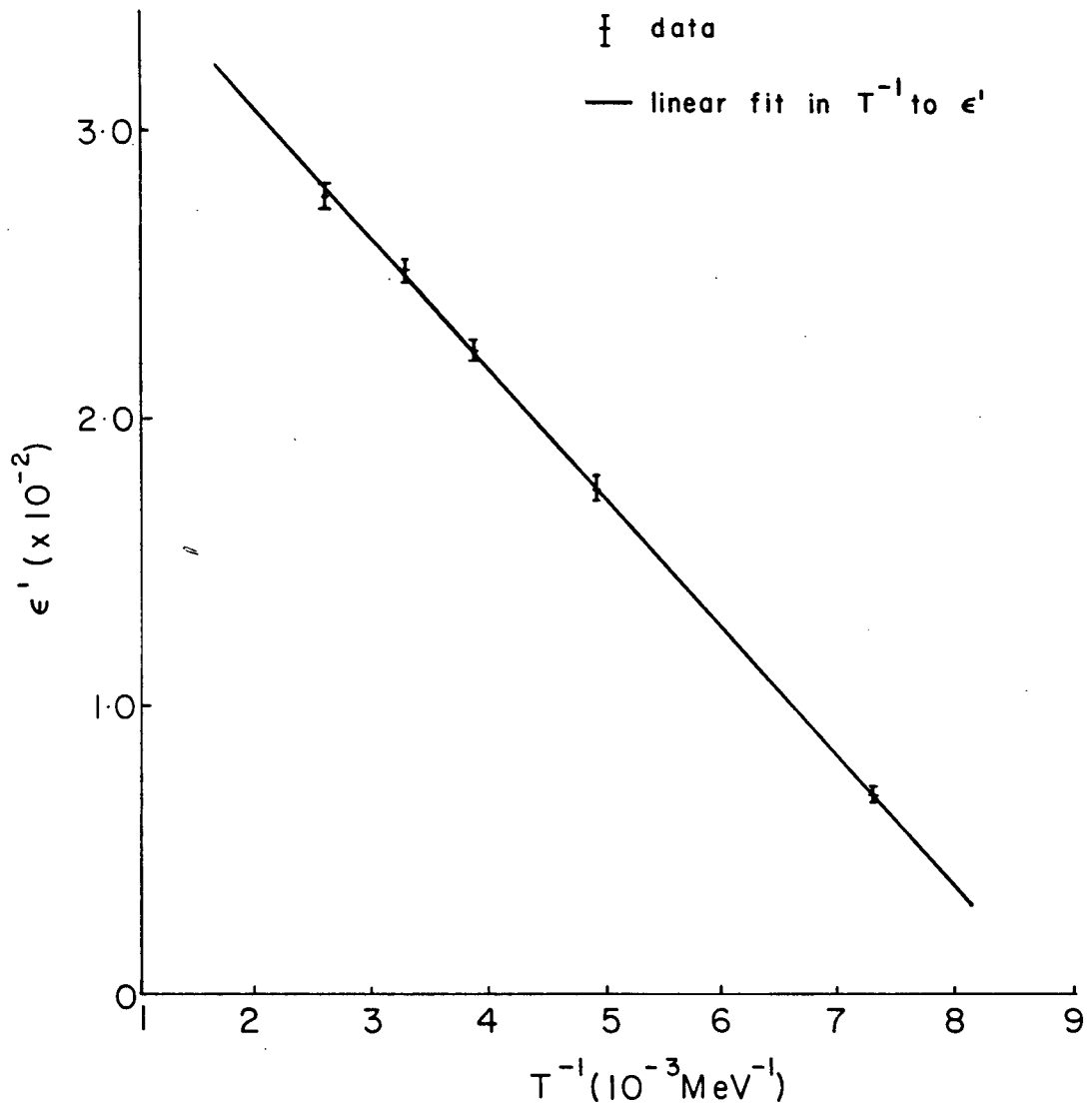


Fig 34. Neutron detector efficiencies without exit track cuts. The uncut efficiency was well fit by a line in  $T^{-1}$ . This fit was used to obtain values of  $\xi(T)$ , using the  $0^\circ$  data.

with the error matrix for the fit

$$\begin{array}{cc} 1.263 \cdot 10^{-7} & -1.973 \cdot 10^{-5} \\ -1.973 \cdot 10^{-5} & 3.396 \cdot 10^{-3} \end{array}$$

The fit had a  $\chi^2$  of 0.33 per point, showing that the form of the fitting function well describes the data.

#### IV.2.5 Analysis With A 17° Exit Track Angle Cut

This efficiency was obtained by integrating the distribution of Fig 33 up to angles less than 17°. As is common in scattering distributions, the exit track angle distribution becomes more forward peaked with increasing kinetic energy. Consequently, the 17° cut is energy dependent, as shown in Fig 35, where the ratio

$$R(T) = \frac{\int_0^{17^\circ} f(\theta_c) d\theta_c}{\int_0^{90^\circ} f(\theta_c) d\theta_c}$$

is plotted, showing a U shape with a minimum around 260 MeV. The exit track angle distribution is described by  $f(\theta_c)$ . This change is most likely due to the onset of range effects, where charged particles produced near the upstream edge of the carbon do not have sufficient energy

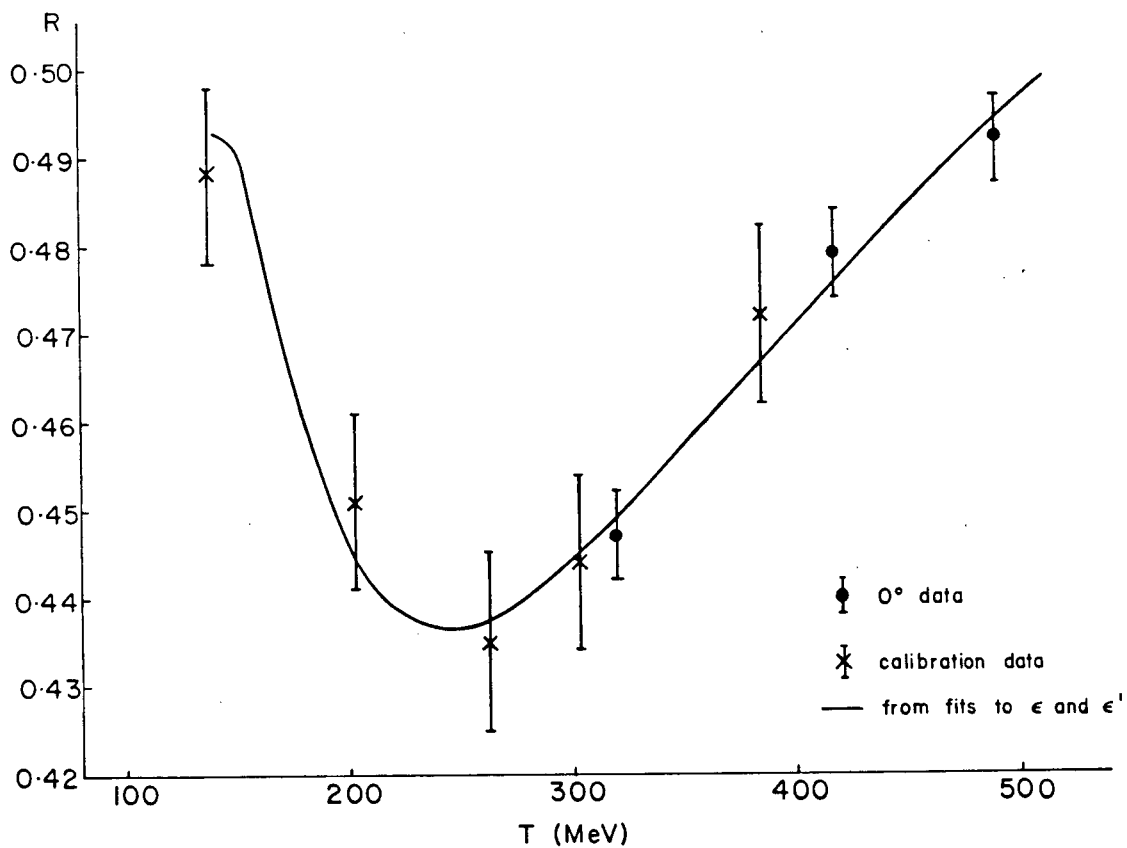


Fig 35. Ratio of efficiencies with and without the exit track angle cut.

The ratio shows that the  $17^\circ$  exit track angle cut is very energy dependent, and has a complicated form. It is this cut which complicates the form of  $\Sigma(T)$ .

to trigger the remainder of the detector.

As is discussed later in the text, data was taken with the neutron detector at zero degrees, sampling the neutron beam, at four energies: 212, 320<sup>33</sup>, 418, and 490<sup>33</sup> MeV. The energies of 418 and 320 MeV were close to those calibration settings of (499 MeV, 25°) and (429 MeV, 35°), so that comparisons of the exit track angle distributions were possible. It was found that the values of R at approximately equal energies were the same, within statistics, for the 0° and calibration data. This was possible since both data sets involved approximately the same area of the carbon converter, so that geometrical effects cancel. In addition, the exit track angle distribution fell off quickly for angles greater than about 25°, so that effects due to the tail of the distribution were minimized.

Using the fit for  $\xi'$ , the efficiency for the "cut" data  $\xi$ , was obtained by

$$\xi(T) = R(T) \xi'(T)$$

Since the 0° data gave good agreement with the calibration data for R at two energies, it was assumed to

also be the case for 490 MeV as well. The 212 MeV  $0^\circ$  data was not used due to the failure of P2E in the forward hemisphere data at that energy. The three values of  $B(T)$ , also shown in Fig 35, were used to determine values of  $\mathcal{E}$  to augment those from the calibration in order to better determine the functional form of  $\mathcal{E}(T)$  at high energies. All these points are shown in Fig 36, and listed in Table 11, illustrating a kink around 260 MeV. These data have been fit to a cubic polynomial in the inverse kinetic energy

$$\mathcal{E}(T) = A + B/T + C/T^2 + D/T^3$$

WHERE

$$A = .0269 \pm .0013$$

$$B = -7.85 \pm 1.05$$

$$C = 1169. \pm 265. .$$

$$D = -73317. \pm 19900. .$$

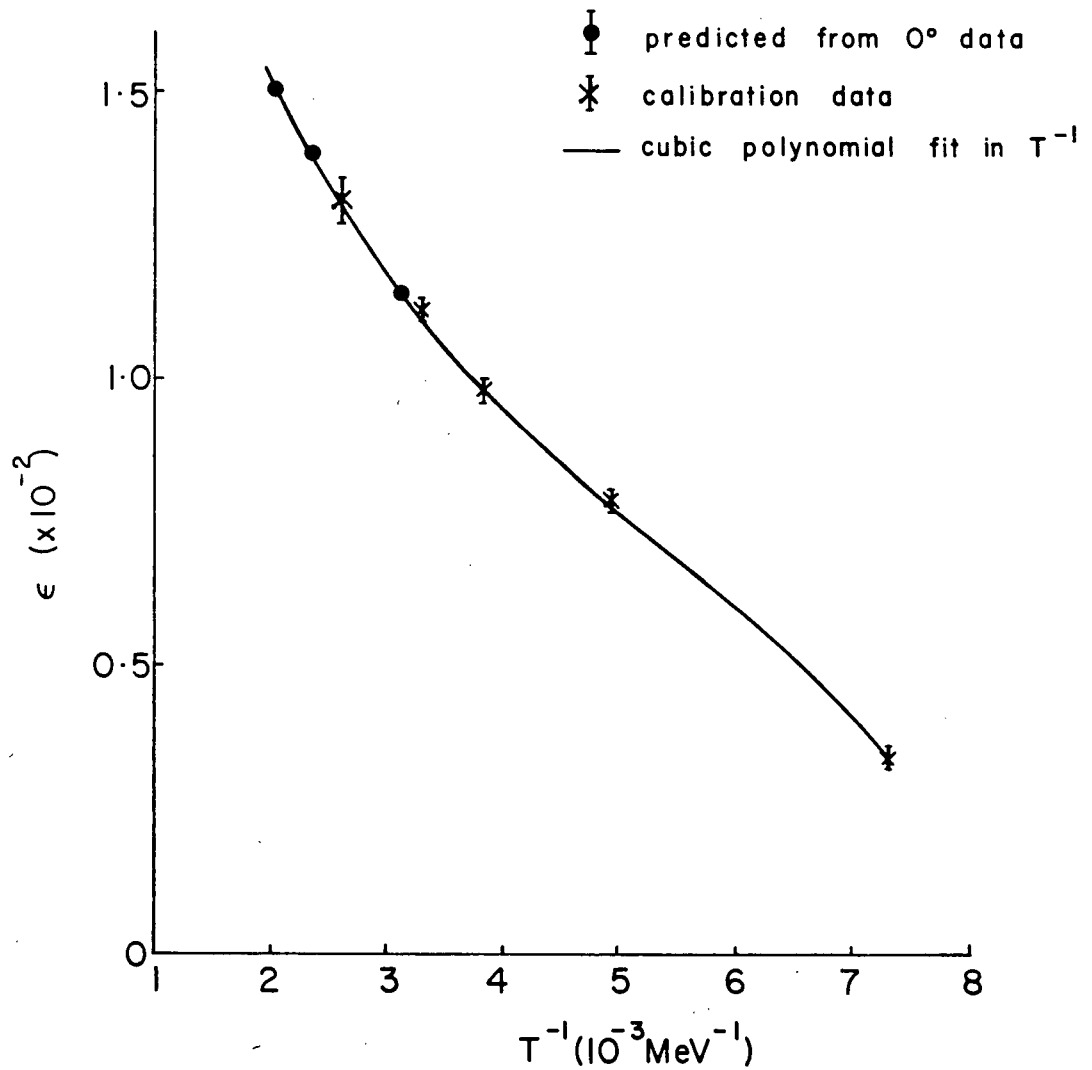


Fig 36. Neutron detector efficiencies with exit track cuts. The cut efficiency was well fit by a cubic polynomial in  $T^{-1}$ . Data obtained from the 0° data was used to help determine the functional form at the higher energies.

Neutron Energy Incident on the Detector  (MeV)	Efficiency  $\epsilon(T)$
490.*	0.0151 $\pm$ 0.0001
418.*	0.0139 $\pm$ 0.0001
384.5	0.0131 $\pm$ 0.0004
320.*	0.0115 $\pm$ 0.0001
302.8	0.0112 $\pm$ 0.0002
261.3	0.00976 $\pm$ 0.00021
203.3	0.00788 $\pm$ 0.00020
137.2	0.00337 $\pm$ 0.00010

Table 11. Neutron detector efficiencies with exit track cuts.  
Data marked by a \* are from 0° data.

The error matrix for the fit was

$$\begin{bmatrix} 0.167 \cdot 10^{-5} & -0.135 \cdot 10^{-3} & 0.333 & -24.5 \\ -0.135 \cdot 10^{-3} & 1.120 & -277. & 2.06 \cdot 10^4 \\ 0.333 & -277. & 7.00 \cdot 10^4 & -5.25 \cdot 10^6 \\ -24.5 & 2.06 \cdot 10^4 & -5.25 \cdot 10^6 & 3.96 \cdot 10^8 \end{bmatrix}$$

this functional form used four parameters to characterize eight data with a  $\chi^2$  per point of 0.25. Fits to lower order polynomials gave significantly higher  $\chi^2$ . This form of  $\xi(T)$  was used in the analysis of the forward hemisphere.

No model has been developed to describe this dependence, although some work has shown that it is primarily due to the energy dependence of the n-C<sup>12</sup> cross section coupled with the range effects of the 9 cm thick block of carbon.

#### IV.2.6 Error Analysis

No physically intuitive explanations have been put forward to justify the use of a linear fit in the inverse kinetic energy for the uncut calibration data, and a cubic polynomial fit to the cut data. Consequently, it is necessary to explore the use of other, possibly equivalent, functional forms for these fits.

Six fits were made in order to estimate this uncertainty. To test the assumption that  $\xi(T)$  could be obtained from  $\xi'(T)$ ,  $\xi'$  was fit to both linear and cubic polynomials in  $T^{-1}$ . This procedure changed the predicted values of  $\xi$  from the  $0^\circ$  data by less than 1%.

Furthermore, the efficiency  $\xi$ , with the  $17^\circ$  exit track angle cut applied, was refit to cubic polynomials in  $T^{-1}$  and  $p^{-1}$ , the inverse momentum. Each fit was performed using the predicted  $0^\circ$  points from the two fits to  $\xi'(T)$ , hence four fits to  $\xi(T)$ . The  $p^{-1}$  fits both gave higher  $\chi^2_{\nu}$  than the  $T^{-1}$  fits.

Most of the uncertainty in the fit to  $\xi(T)$  was in the energy region between 137 and 200 MeV, where there was no data. Using  $T^{-1}$ , this region becomes elongated, making extrapolation over it more questionable. It is in this

area that the  $T^{-1}$  and  $p^{-1}$  fits show a different shape, and so affect the efficiency ratios in the wide angle settings of the forward hemisphere data most seriously.

The  $p^{-1}$  fits were assigned a lesser weight in estimating the errors involved due to the relative pooriness of the  $\chi^2$ , (0.40 compared to 0.25 for  $T^{-1}$  fits). All four fits were compared, and half the worst difference of the efficiencies and for efficiency ratios for the fits adopted, and the remaining three fits were taken to be a good estimate of the error incurred by choosing those fits, i.e. a linear polynomial in  $T^{-1}$  for  $\xi'(T)$ , and a cubic polynomial in  $T^{-1}$  for  $\xi(T)$ . The results are shown in Table 12, listing the in the uncertain portion of the  $\xi(T)$  curve. The  $35^\circ$  point was well constrained by the lowest energy calibration point for all fits.

A second error incurred in the analysis was due to our knowledge of the incident neutron beam energy, which is known to about  $\pm 2$  MeV, due to the final state interaction of the protons in the  $p(d,n)2p$  reaction. This effect becomes most serious for the low energy end of the  $\xi(T)$  curve. Using the  $T^{-1}$  fit for  $\xi(T)$ , with an error  $dT$  on the incident neutron beam energy, with

$$R' = \xi(T) / \xi(T)$$

<u>Incident Neutron Beam Energy (MeV)</u>	<u>Polar Scattering Angle (Lab) (deg)</u>	<u>"Fitting" Error (%)</u>	<u>Error due to Energy Uncertainty (%)</u>	<u>R(T,θ)</u>	<u>Error calculated from error matrix (%)</u>	<u>Total Error</u>
418±2	0	(0.5)	(0.3)	-	(0.5)	(0.77)
	10	0.2	-	1.0235	0.10	0.22
	12.5	0.1	0.01	1.0370	0.14	0.18
	22.5	0.4	0.03	1.132	0.43	0.59
	37.5	0.8	0.09	1.489	1.29	1.52
	45	0.9	0.24	1.925	3.19	3.3
212±2	0	(0.3)	(0.94)	-	(2.3)	(2.5)
	7.5	0.1	0.02	1.0193	0.18	0.28
	15	0.5	0.12	1.0840	0.73	0.89
	22.5	1.5	0.38	1.224	1.6	2.3
	35	-	4.2	2.418	3.7	5.6

Table 12. Error estimates for the efficiency of the neutron detector.

The estimated errors involved in R were the choice of the fitting function, the error calculated from the error matrix of the fit, the error due to uncertainty in neutron beam energy, and the total error are listed. The quantities in brackets refer to the efficiencies  $\epsilon(T)$  calculated at 212 and 418 MeV.

the error in  $R'$  is

$$\delta R' = \frac{\partial R'}{\partial T_i} dT_i = \frac{2 \varepsilon(T_i)}{\varepsilon(T_s) \partial T_i} - \frac{\varepsilon(T_i)}{\varepsilon^2(T_s)} \frac{\partial \varepsilon(T_s)}{\partial T_s} \frac{\partial T_s}{\partial T_i}$$

with

$$\frac{\partial \varepsilon}{\partial T} = \sum_{j=0}^3 j a_j / T^{j+1}$$

$$\frac{\partial T_s}{\partial T_i} = \frac{T_s}{T_i} \left( 1 - \frac{T_s^2}{2m} \tan^2 \theta \right)$$

where  $T_s$  is the scattered neutron kinetic energy,  $\theta$  is the scattering angle, and  $m$  is the nucleon mass. The results for the efficiencies at 212 and 418 MeV, and for  $R'$  corresponding to the forward hemisphere data are also listed in Table 12. For all but the  $35^\circ$  point at 212 MeV, energy uncertainty contributes less than 0.5% error to  $R'$ . At this setting, the error is large- 4.2%, due to the low energy of the scattered neutrons at this angle.

These errors are systematic in nature, and must be added in to the errors calculated from the fit for  $\xi(T)$  itself. The values for  $R'$  and the total error are also listed in Table 12.

### IV.3 THE NEUTRON MONITORS

The purpose of these monitors, placed in the neutron beam, was to measure the flux of elastic neutrons incident on the liquid hydrogen target, while either the neutron detector or proton spectrometer was downstream of the target measuring the number of scattered neutrons. As such, the resulting cross sections depend heavily on the properties of the monitors.

The monitors used for the calculation of the differential cross section were the charged particle ones (CL+CR) and G1•G2, since it was felt unwise to base the monitors on the singles rate of the veto counter, CV.

#### IV.3.1 Monitor Stability

The data for the cross section measurements were taken over extended periods of time and often with very different primary proton beam intensities. Consequently, the count rates were required to be stable with time and be linear with the beam intensity. Fig 37 shows the ratio of count rates of the in-beam neutron monitor to the out-of-beam monitor. This figure shows that these monitors

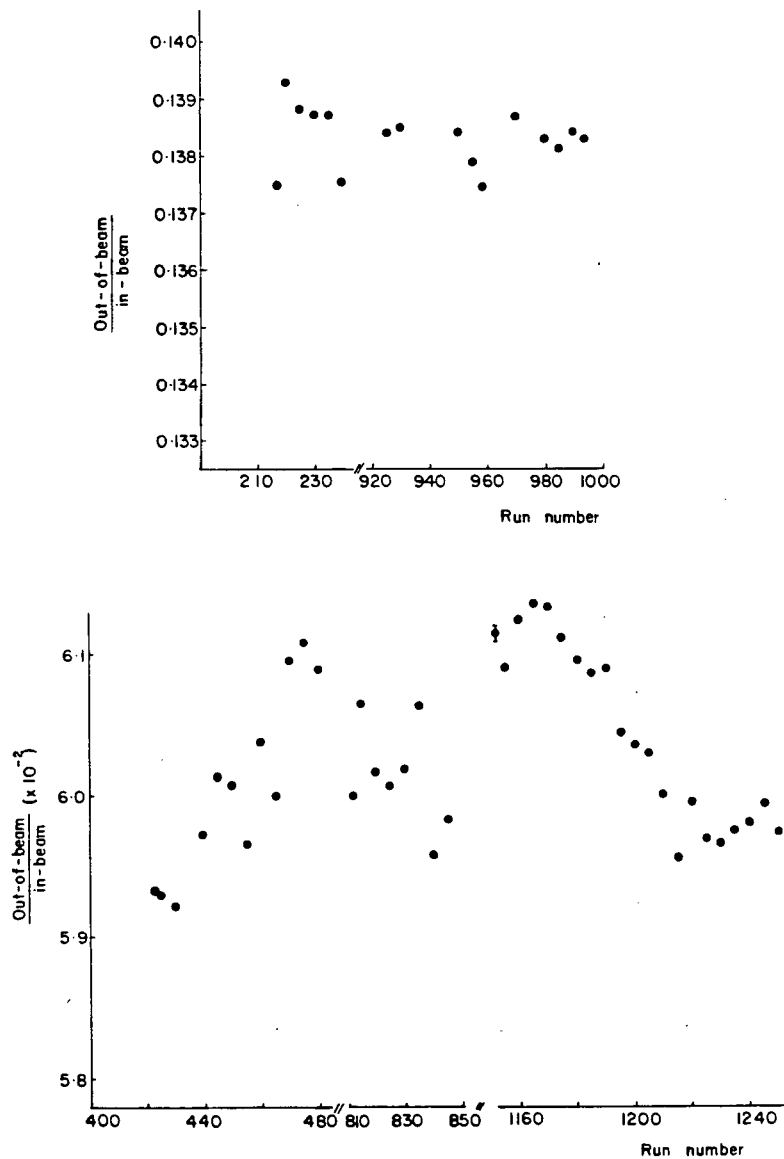


Fig 37. Ratio of in-beam to out-of-beam monitor counts as a function of time.

The ratio, plotted against data run number, stayed constant to a level of about 1% over the entire running period. The change in the ratio is attributed to the sensitivity of the in-beam monitor to running conditions.

were stable to a level of 0.5% at 212 MeV and 1% at 418 MeV. The higher instability at the higher energy is most likely due to the increased fraction of low energy background above the inelastic threshold.

It was found that the in-beam monitor was very sensitive to the high tension (HT) applied to its photomultipliers. A variation of 100 V gave about 15% variation in its count rate. This was due to the low energy components of the neutron beam incident on it, as well as to conversions of neutrons to charged particles in the monitor itself. Variations in the HT would indeed be expected to affect the pulse heights of those particles accepted by the discriminators for the counters in the monitor.

The out-of-beam monitor did not suffer from this problem, as copper plates were included to eliminate low energy background.

Programmable power supplies<sup>30</sup> were used to minimize the effects of variations in the HT. These supplies were able to hold the voltages to within about one volt of the nominal settings. This allowed the use of the in-beam monitor for analysis of adjacent runs where neither the HT nor the power supplies themselves might have been changed.

As both the P/S and HT's had been changed at certain times, it would be incorrect to use this monitor for the cross calibration of the monitors for the absolute normalization of the backward hemisphere data.

#### IV.3.2 Monitor Linearity With Neutron Flux

Fig 38 shows the variation of the monitor counts with those of the proton polarimeter. Within the stability of the polarimeter, there is no variation from linearity down to proton currents of about 50 nA. A deviation at low currents has been traced to the radioactivity of both the main collimator and the sweep magnet, having a half life of about 30 - 60 min. In addition, the counters themselves exhibited an induced activity. These three sources contributed a constant background at equilibrium with the beam on, and a slowly decaying background with it off. This effect showed up only for data taken with primary proton currents of a few nA: the zero degree runs taken for the forward hemisphere data. The corrections required were on the order of 6% for the in-beam monitor, and 3% for the out-of-beam one, and are listed in Table 13. It was found that the out-of-beam monitor was far less dependent on the previous history of beam current (which

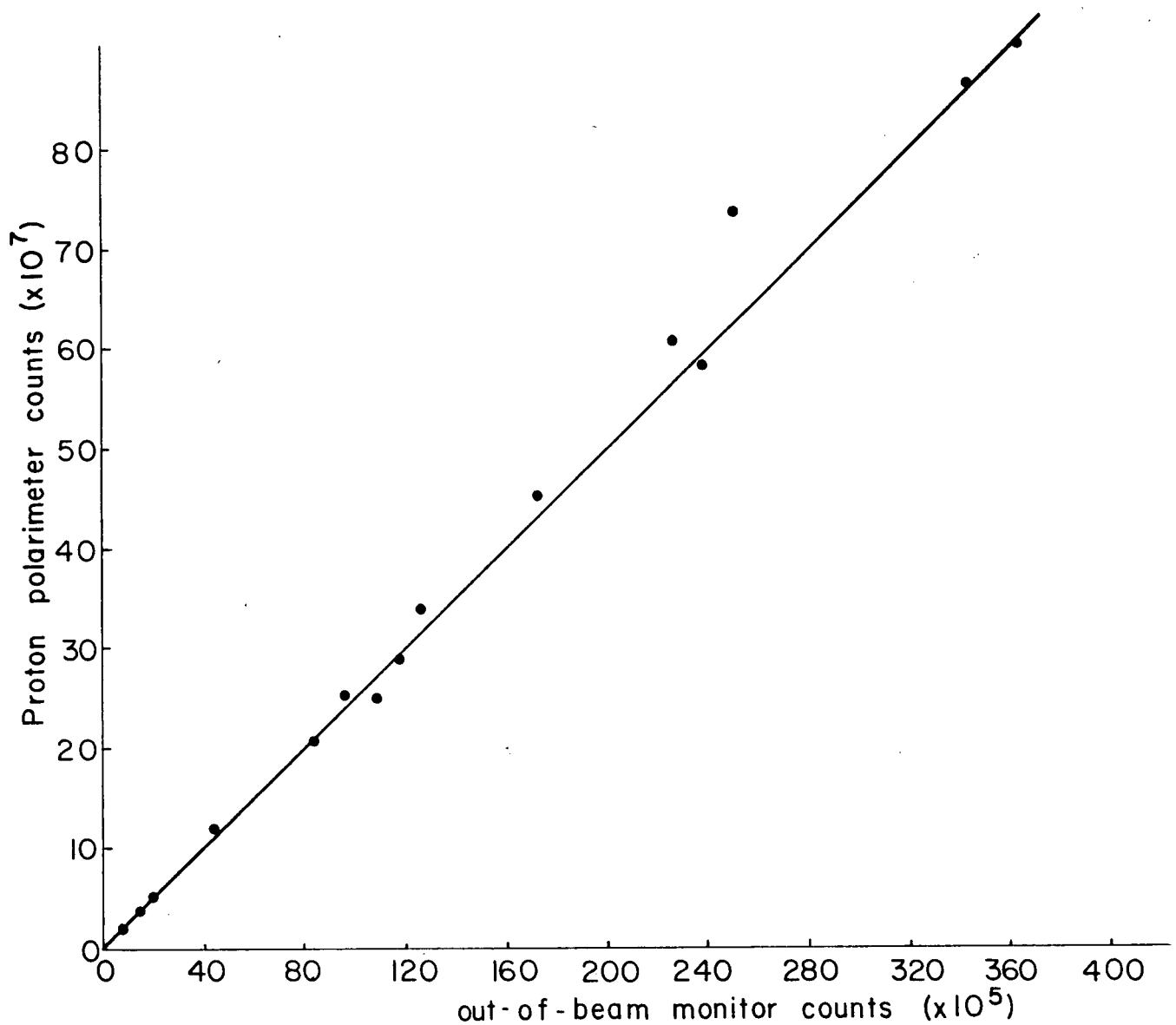


Fig 38. Relation between the out-of-beam monitor and proton polarimeter count rates. The linearity of the out-of-beam monitor with neutron intensity is shown. The scatter in the points is primarily due to the instability of the polarimeter as an intensity monitor.

<u>Neutron Beam Energy (MeV)</u>	<u>Monitor</u>	<u>"Beam Off" Count Rate (sec<sup>-1</sup>)</u>
212	in-beam	1.29 ±0.05
	out-of-beam	0.194 ±0.019
418 (early runs)	in-beam	17.3 ±0.1
	out-of-beam	0.311 ±0.01
418 (late runs)	in-beam	18.2 ±0.2
	out-of-beam	0.455 ±0.023

Table 13. Corrections to the monitors for induced activity.

determined the level of activity) than the in-beam monitor, making it much more stable in this respect.

#### IV.3.3 Random Coincidences In The Monitors

The count rates of the monitors were indeed rate dependent for large fluxes of neutrons. The probability that the coincidences were random (and not due to legitimate protons traversing the monitor) rises with increasing flux.

These effects were measured in all runs by the fast electronics, as discussed previously. This was achieved by delaying the signal from one counter in a coincidence by a multiple of the RF period. The random coincidence rate in the in-beam monitor was about 2%. This effect was negligible in the out-of-beam monitor.

#### IV.4 ANALYSIS OF THE FORWARD HEMISPHERE DATA

##### IV.4.1 Elimination Of Backgrounds

As discussed in Sec. IV.1.1.1, the principal sources of background from the hydrogen were neutrons and  $\gamma$  rays from inelastic reactions. These were separable from the elastically scattered neutrons by TOF with respect to the cyclotron RF. A typical P1-RF TOF spectrum is shown in Fig 39. To better illustrate the hydrogen-associated events, an empty target subtraction has been performed on this data. The background  $\gamma$  rays are off the high end of the scale, and the inelastics have no distinguishable onset. These backgrounds are well separated, as indicated by the fact that the results are insensitive to reasonable variations in the cuts on the P1-RF TOF spectrum. This will be dealt with later in the error discussion.

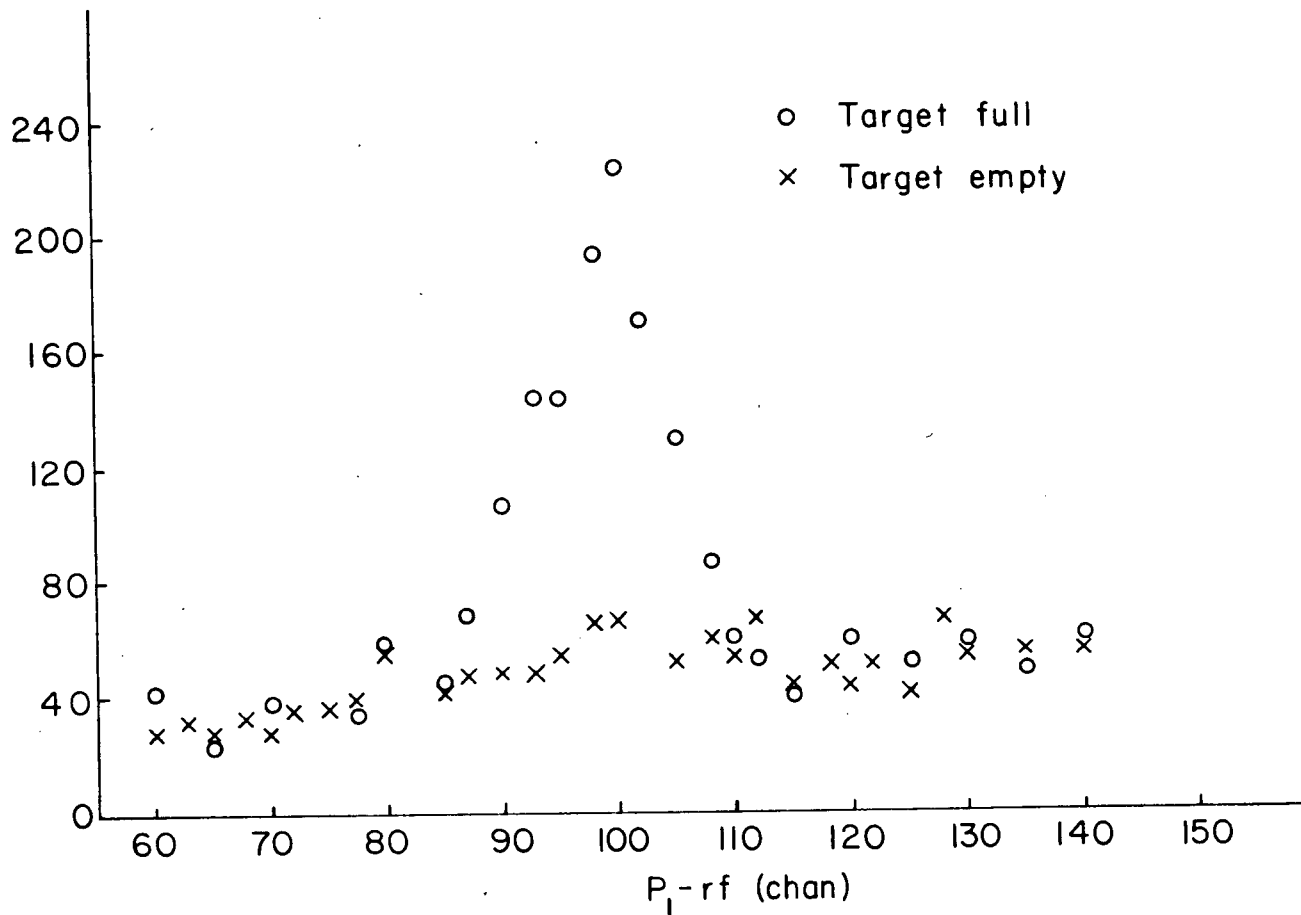


Fig 39. Typical P<sub>1</sub>-RF TOF spectrum for the neutron detector.

This data is from a run at 418 MeV with the detector at 22.5°. The empty target background accounts for the tails of the peak, and the  $\gamma$  rays are off the high end of the scale.

#### IV.4.2 Corrections Due To Equipment Problems

When analyzing the data at 212 MeV, it was found that all but one of the angular settings had been taken with the P2E counter almost inoperative. This introduced small errors in the determination of  $d\sigma/d\Omega$  as the geometrical inefficiency was slightly different for the data taken at  $0^\circ$  and those taken at non-zero angles. A procedure was devised to cut out any tracks which intersected P2 in the region of P2E, and then use a smoothing algorithm to fill in the area, based on the remainder of the data.

This procedure is discussed in some detail in Appendix B<sup>31</sup>. Briefly, the method can be described as follows. As mentioned previously, scattering cross sections depend only on the polar angle  $\theta$ . Therefore, the number of particles at angle  $\theta$  is

$$N(\theta) = \int_0^{2\pi} n(\theta) d\phi$$

assuming that the detector covers the entire  $2\pi$  range in  $\phi$  for  $\theta$ . If it does not, for all events at  $\theta$ , the fraction of  $2\pi$  allowed can be calculated from the geometry of the detector. This data is then weighted by that fraction to give the expected total number  $N(\theta)$ . The final number of particles detected is then given by

$$N = \int_{\theta_{\min}}^{\theta_{\max}} N(\theta) d\theta$$

The integration over  $\theta$  can be considered to have been evaluated by the distribution in  $\theta$  and sum of the actual data.

A region slightly larger than P2E was excluded from the data, and then this procedure was used to weight the data to account for the loss. In order to check the validity of the method, the unaffected setting at 212 MeV, and a setting at 418 MeV were subjected to it, i.e. the perfectly good data was artificially removed and then replaced. In both cases the "before" and "after" results agreed to better than 0.25%, giving confidence in the correction for the remainder of the data. Approximately 10% of the data was affected by this correction.

#### IV.4.3 Empty Target Subtraction

As discussed in Sec. IV.2, a significant fraction of the events accepted by the neutron detector originated in the material of the hydrogen target. Since it was a single arm detector, there was no recoil coincidence test available to constrain the background. As a result, background levels were on the order of that of the signal. Fig 39 showed a typical pair of full and empty runs, normalized to the same incident beam. This background

accounts for the large tail of the spectrum.

#### IV.4.4 Zero Degree Data

In order to provide normalization to the forward hemisphere data, data was taken with the neutron detector at  $0^\circ$ . At this position, it sampled the same neutron beam as the monitors. Due to the length of the helium bag, it was not placed between the  $\text{LH}_2$  target and the neutron detector for this measurement.

The intensity of the primary proton beam was reduced to a few nA for these runs, at which time the constant background from the activity around the monitors became significant. As discussed previously, beam-off runs were taken to estimate the effect.

Fig 40 shows a typical P1-RF TOF spectrum of the neutron beam, illustrating the quasi-elastic neutron peak and a small, but long, low energy tail, and the  $\gamma$  ray peak (due to  $\pi^0$  production at the deuterium target). The effect of the tail is to shift the average incident neutron energy slightly downward. The  $\gamma$  peak is cleanly separated from the elastics. As the  $\gamma$  rays were separable from the elastic neutrons, and the out-of-beam

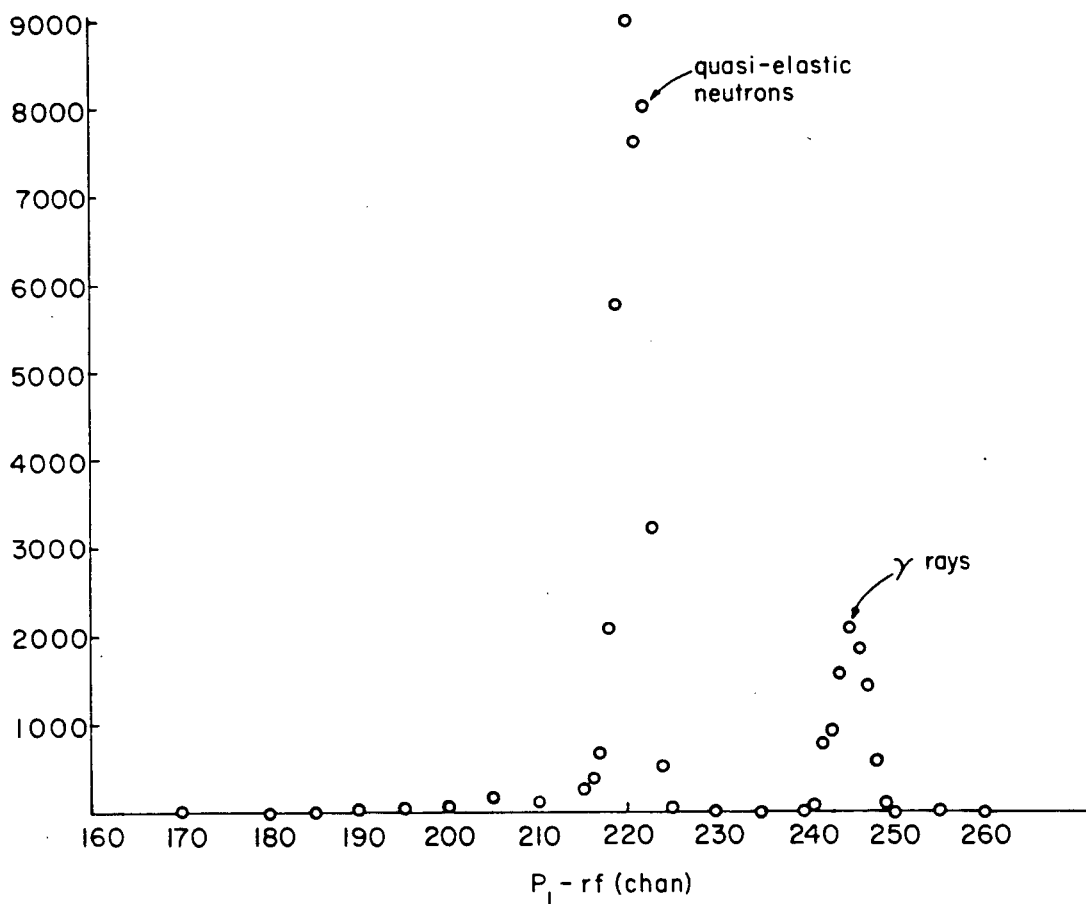


Fig 40. Neutron beam RF time of flight spectrum.  
 The RF spectrum shows a narrow quasi-elastic neutron peak, a small but long low energy tail, and the  $\gamma$  rays produced at the  $\text{LD}_2$  target. The  $\gamma$ 's are well separated from the neutrons.

monitor was insensitive to them, no absorber was placed in the neutron beam (upstream of the monitors) to eliminate  $\gamma$  rays, as had been done in other measurements of the n-p differential cross section.

#### IV.4.5 Time Of Flight Cuts On The Data

The events accepted by the neutron detector, for all the forward hemisphere data, was mono-energetic within the resolution of the TOF measurement. Therefore, the same cuts were applied with respect to the RF for the data at all angles. The cut used was  $\pm 20$  channels from the elastic peak. As is discussed later in the error analysis, the results were insensitive to reasonable variations in this cut. It should be noted that this RF width was almost entirely due to the cyclotron bunch width and not the spread in energy of the neutron beam.

#### IV.4.6 Corrections To The Raw Data

##### IV.4.6.1 Incident Beam

Some of the  $0^\circ$  runs were taken with the hydrogen target full. These were corrected, using the well-known values of the total cross section for free n-p scattering, to include them in the data set. Approximately 2-3% of the beam was attenuated by the hydrogen.  $\sigma_{np}$  is known to about 3% at these<sup>32 33</sup> intermediate energies, so that the error on the correction was on the order of 0.05%, which is completely negligible.

The number of neutrons accepted was corrected for attenuation in the material downstream of the liquid hydrogen in the flask. This increased the yield by about 1%.

#### IV.4.6.2 Data At Non-Zero Angles

Since the target was of non-zero length, the neutron beam was attenuated as it passed through. On average, the neutron flux at the center of the target was reduced by the value

$$\exp\left(-\frac{N_0 \rho t}{2A} \sigma_{tot}\right)$$

where the quantities refer to hydrogen. The number of events detected were scaled upwards to account for this loss, and amounted to corrections of

1.018

1.015

at 212 and 418 MeV respectively.

As discussed in length previously for the calibration data, there was a correction to be applied for the multiple scattering of the incident beam neutrons and attenuation along the path to the neutron detector. The method of calculation was the same as previously, except for the different geometry. The results are listed in Table 14 as a function of scattering angle. These corrections were typically of the order of 1-2%.

Neutron Beam Energy (MeV)	$\theta^*$ (degs)	Correction Multiplicative
212	10	1.034
	20	1.015
	30	1.015
	40	1.014
	50	1.014
	60	1.013
	70	1.013
	80	1.013
418	10	1.024
	20	1.011
	30	1.010
	40	1.010
	50	1.009
	60	1.008
	70	1.006
	80	1.006
	90	1.006

Table 14. Corrections to the forward hemisphere data.  
The calculated corrections for attenuation and multiple scattering are listed.

As for the  $0^\circ$  data, when the target was empty, there was gaseous hydrogen in the flask. The density of the gas was determined by the measured temperature, and is discussed in Appendix C. This gas caused some elastic scattering of neutrons into the neutron detector when it was at non-zero angles. The number of neutrons was determined by the ratio of the densities of the liquid and gas, giving a correction factor of 1.0077 for all the finite angle settings.

#### IV.4.7 Parameters Needed To Calculate $d\sigma/d\Omega$

As discussed in Chapter II, the differential cross section in the forward region is given by

$$\frac{d\sigma}{d\Omega_{cm}} = \frac{N_p(\theta)}{N_p(0)} \frac{\epsilon(E_i)}{\epsilon(E_s)} \frac{N_{mon}(0)}{N_{mon}(\theta)} \frac{A}{N_{opt} d\Omega} \frac{d\Omega_{LAB}}{d\Omega_{cm}}$$

where  $d\Omega_{LAB}/d\Omega_{cm}$  is the Jacobian for the transformation to the center of mass frame.

The quantities which remain to be given are the hydrogen target density and length, and the solid angle subtended by the neutron detector. An implicit quantity required is the average angle of scatter into the detector.

The density of the liquid is discussed in Appendix C, and was  $0.07005 \pm 0.00040$  g/cm<sup>3</sup>. The target length was discussed in Chapter III and was  $19.85 \pm 0.01$  cm.

The solid angle subtended by the detector is given by

$$d\Omega = \frac{\int \rho(r) r dr d\psi \int e^{-n_t \sigma_{tot} l} dl \int dx dy \hat{n} \cdot \hat{R} / R^2}{\int \rho(r) r dr d\psi \int e^{-n_t \sigma_{tot} l} dl}$$

integrated over the face of the detector, and over the spatial distribution of the incident beam and volume of the target. However, since the detector is so far from the target, this expression becomes the usual

$$A/r^2$$

for a point source, to high accuracy.

The average angle was calculated by evaluating

$$\langle \theta \rangle = \frac{\int \rho(r) r dr d\psi \int e^{-n_t \sigma_{tot} l} dl \int dx dy \theta}{\int \rho(r) r dr d\psi \int e^{-n_t \sigma_{tot} l} dl \int dx dy}$$

where  $(r, \psi)$  are cylindrical coordinates about the incident beam axis,  $l$  represents the target length, and  $(x, y)$  cover the face of the neutron detector. The shape of

the beam is taken as Gaussian with the measured width.  $\langle \theta \rangle$  was found to equal the nominal scattering angle for all settings greater than a few degrees. Therefore, all average angles for the forward hemisphere data were taken to be the nominal angles.

#### IV.4.8 Error Estimate

Aside from the purely statistical errors in making the measurements, some error is incurred in applying the cuts to the data, selecting the elastic events. In addition, the monitor instabilities and errors in geometrical and target parameters are involved in the uncertainty of the final result.

The effect of possible jitter in application of the cuts on the data was simulated by varying the cuts over reasonable limits, and reanalyzing the data for each variation. The cuts made on the forward hemisphere data were on the exit track angle, the active area of the carbon, and the two TOF spectra.

The error in determining the exit track angle is negligible, since the data is always analyzed in ratios. The determination of the active area also involves

negligible error, as binning effects at the edges should cancel from blurring of the interaction points of particles on either side of the cut. Table 15 shows a plot of the differential cross section for a variety of choices of these quantities.

The cross section varies by about 1% for the values of  $\theta_{\max}$  shown. The efficiency function shape is dependent on the choice of this angle, so that the majority of this variation is most likely due to not having re-evaluated the efficiency as a function of energy for the choices of  $\theta_{\max}$ . This error is also taken to be negligible.

Within statistics, there is no change in the differential cross section in shrinking the active area of the carbon from 40 to 30 cm in each plane.

Table 15 also shows the variation in the elastic neutron yield for different cuts on the TOF spectra. Even for large excursions of the P1-P2 TOF cut there is less than a 0.2% change in the signal.

A  $\pm 2$  channel jitter on the RF TOF gives a reasonable estimate of the possible error involved in this cut from run to run. Table 15 shows that an error of about 0.4% for non-zero angle data and 0.5% for  $0^\circ$  data is introduced. Since all the neutron data was taken at about the same

$\theta_{max}$ Cut			RF TOF Cut	
(deg)	$d\sigma/d\Omega$ (mb/sr)		lower limit + x (chan)	signal (arb. units)
17	4.73 $\pm$ 0.12		0	0.9177 $\pm$ 0.0439
16	4.78		2	0.9152
16.5	4.78		4	0.9056
17.5	4.72		6	0.9066
18	4.70		-2	0.9213
			-4	0.9275
			-6	0.9256

Carbon Active Area			P1-P2 TOF Cut	
x width (cm)	y width (cm)	$d\sigma/d\Omega$ (mb/sr)	lower limit +x (chan)	$d\sigma/d\Omega$ (mb/sr)
40	40	4.73	0	4.73
35	40	4.76	3	4.74
30	40	4.74	5	4.73
40	35	4.75		
40	30	4.73		

Table 15. Variation of  $d\sigma/d\Omega$  for various choices of the cuts.

The sensitivity of the results to the choice of RF cuts, the active area of the carbon, the exit track angle cut, and the TOF through the detector are shown.

time, the same RF spectrum was used throughout.

As discussed previously, the neutron beam monitor exhibited instability at the 1% level at 418 MeV, and 0.5% at 212 MeV. The uncertainty in the solid angle was about 0.4%, and 0.5% for the target density. The error in the target length was negligible.

In summary, the only non-negligible sources of error in the calculation of the forward hemisphere differential cross section were the solid angle, the target density, the RF cuts, and the monitor instability. Added in quadrature, these errors totalled 1.6% and 1.3% at 418 and 212 MeV, respectively.

#### IV.4.9 Angular Distributions

The differential cross sections for the forward hemisphere at 212 and 418 MeV are listed in Table 16. Qualitative aspects of the distributions will be discussed later with the presentation of the backward hemisphere data.

Neutron Energy (MeV) -----	$\theta$ * (deg) -----	$d\sigma/d\Omega$ (mb/sr) -----
212 $\pm$ 2	15.1	5.70 $\pm$ 0.12
	31.6	4.36 $\pm$ 0.08
	47.2	3.07 $\pm$ 0.08
	72.9	1.95 $\pm$ 0.12
418 $\pm$ 2	22.1	4.66 $\pm$ 0.08
	27.5	4.29 $\pm$ 0.10
	49.2	2.96 $\pm$ 0.06
	80.6	1.69 $\pm$ 0.04
	95.8	1.37 $\pm$ 0.06

Table 16. Results for the differential cross section at 212 and 418 MeV.

#### IV.4.10 Cross Calibration Of The Monitors

##### IV.4.10.1 Absolute Monitor Efficiencies

With the neutron detector at  $0^\circ$ , the number of neutrons detected is

$$N_p(0) = N_{mon}(0) \frac{\epsilon}{\eta}$$

where  $\eta$  and  $\epsilon$  are the absolute efficiencies of the monitor and detector, respectively. All these quantities are evaluated at the same incident kinetic energy  $T$ .

$N_p(0)$  has been determined in the data analysis in a fashion identical to that in which the efficiency  $\epsilon$  was measured. It includes an RF cut of  $\pm 20$  channels from the elastic neutron peak.

For the incident kinetic energies 212 and 418 MeV, the values of  $\eta$  for the two neutron monitors are listed in Table 17. Note that the dependence on energy of the cut-of-beam monitor is opposite to that of the in-beam monitor and the neutron detector. This is due to the use of different amounts of copper ranger in the out-of-beam monitor for the two energies.

Neutron Beam Energy (MeV)	Monitor	Efficiency
212	in beam	$(0.604 \pm 0.034) \times 10^{-2}$
	out-of-beam	$(8.38 \pm 0.32) \times 10^{-4}$
418	in-beam	$(1.22 \pm 0.68) \times 10^{-2}$
	out-of-beam	$(7.32 \pm 0.23) \times 10^{-4}$

Table 17. Absolute efficiencies of the neutron monitors.

The RF cut on the  $0^\circ$  data determines the manner in which the backward hemisphere data is to be analyzed: neutrons from the incident beam accepted in that measurement must also come from a  $\pm 20$  channel window about the quasi-elastic neutron peak. This cut therefore determines the energy acceptance in the measurement.

#### IV.10.2 Error Estimate

The monitor efficiencies are calculated from the ratio of the neutron detector efficiency and the quasi-elastic incident beam neutron yield, normalized to the monitors, at  $0^\circ$ .

The error introduced in the neutron yield was due to the cuts applied to the data, monitor stability, and statistics. The sources of error on the determination of the detector efficiency were the statistics on the calibration data, the choice of the fitting function, and the energy resolution of the neutron beam. These errors are listed in Table 12.

There was a third source of error which became apparent in the analysis of the backward hemisphere data.

This was change in the shape of the RF spectrum of the  $0^\circ$  neutron data from that of the proton data. This will be discussed more fully later in the text. The conclusion reached was that allowance must be made for up to  $\pm 2.5\%$  variations in the final results due to this effect. The final errors and normalizations are listed in Table 17.

It should be noted that the normalization errors quoted for the forward and backward hemisphere data are different. This is mostly due to the fact that the forward hemisphere data was taken consecutively with the  $0^\circ$  data and, so, had the same RF distribution. This eliminates the majority of the error assigned to the backward hemisphere data.

#### IV.5 ANALYSIS OF THE BACKWARD HEMISPHERE DATA

With the measurement of the absolute normalization of the neutron detector completed, the determination of the backward hemisphere of the n-p differential cross section became simple in principle: detection of elastically scattered proton (Fig 41), with 100% efficiency, gave the flux of scattered neutrons, while the neutron monitors gave the incident flux.

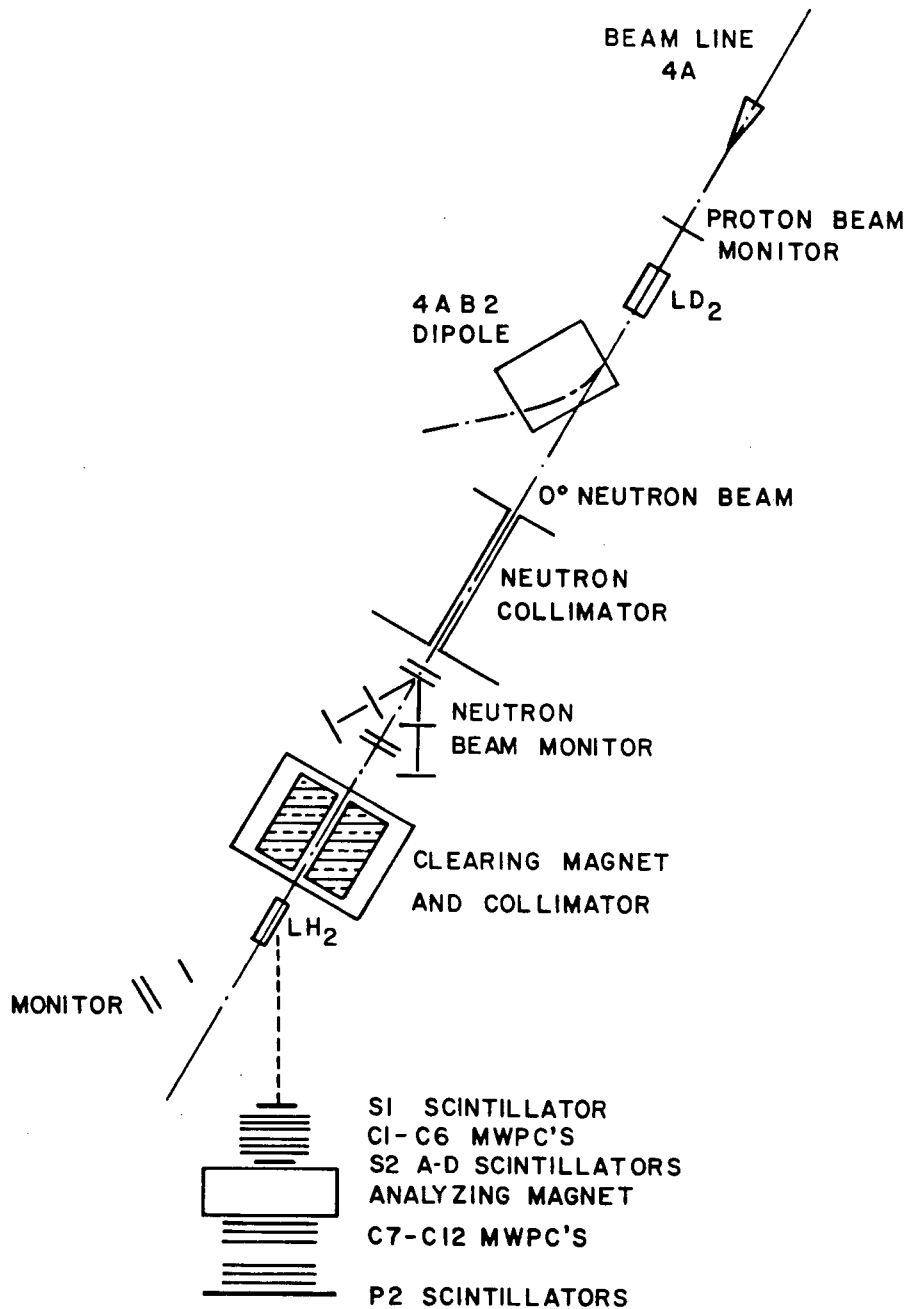


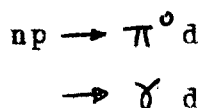
Fig 41. Configuration for the backward hemisphere measurement. Scattered charged particles were detected in a magnetic spectrometer. Elastic protons were identified by TOF through the spectrometer and momentum, and by RF TOF.

This section discusses the methods used to select the elastic protons from the spectrometer data.

#### IV.5.1 Selection Of Events

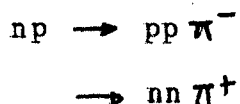
The problem was one of selecting elastically scattered protons from the flux of charged particles incident on the spectrometer. As discussed previously, the background of particles from non-hydrogen associated events was accounted for by the empty target subtraction. Of course, clean elimination of any of these backgrounds, by additional cuts on the data, would help reduce the dependence on the empty target subtraction.

The charged particle background was composed of the following: (i) deuterons from

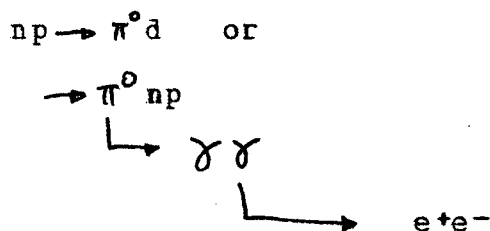


in the allowed kinematic region of typically less than  $12^\circ$  lab.

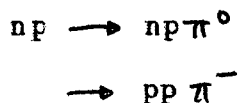
(ii) pions from the reactions



(iii) electrons from the decays of neutral pions



(iv) inelastic protons from the reactions



In the allowed kinematic region of typically less than 35° lab. There was no inelastic production of nucleons from hydrogen at 212 MeV.

The elimination of these backgrounds was achieved by independent measurements of the velocity and momentum of each particle detected. The particles' momenta were determined from the angle between the linear tracks before and after the magnetic field, as determined by the MWPCs,

$$p = \frac{0.3 \int B \cdot dl}{\Delta \theta}$$

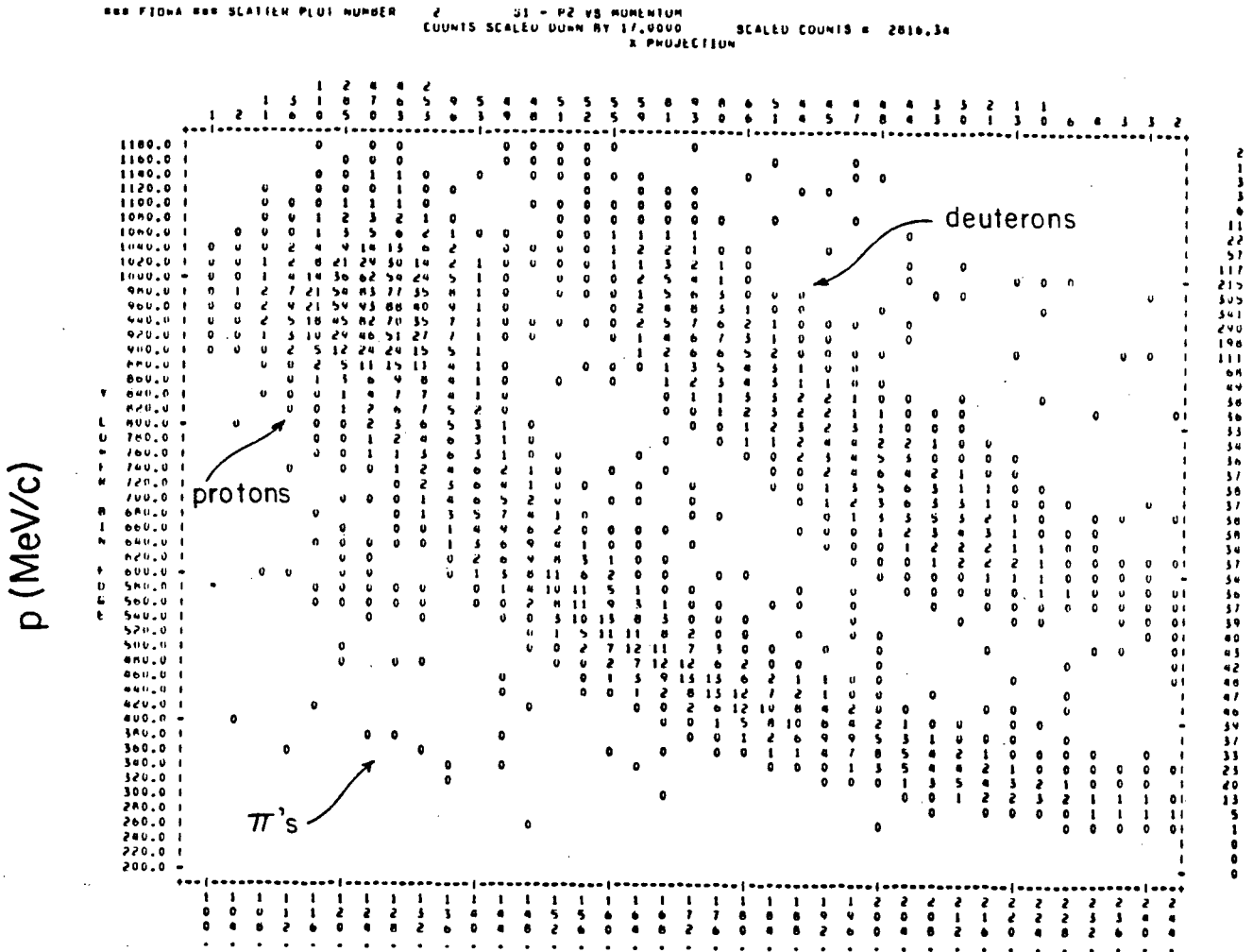
with  $\Delta \theta$  the angle between the tracks in radians,

$$\int B \cdot dl \quad \text{in units of kg-cm, and}$$

p                    the momentum in MeV/c.

In this way, backgrounds from processes (i), (ii), and (iii) were eliminated by correlating the TOF through the detector with the detector, as shown in Fig 42. Effectively, this was equivalent to calculating the mass of the particle. The figure shows a clean separation between the protons and deuterons.

Inelastic protons as well as pions and electrons, were eliminated by momentum analysis. Fig 43 shows the expected average momentum difference between the elastic and most energetic inelastic protons energies, at each angle, neglecting energy losses in the materials in the particles' paths. The elimination of the inelastics was complicated somewhat by the need to accept the same distribution of the neutron beam as was accepted for the calibration of the monitor. In the latter case, the energy determination was made via the TOF technique, which allowed a certain fraction of the tail of the neutron beam to be counted: consequently the TOF method was used to select the incident neutrons in this measurement. Thus, elastic scatters from these lower energy, but perfectly legitimate, neutrons could have been mistaken for inelastics from the elastic neutron peak in the momentum analysis. This possibility was eliminated by correlating



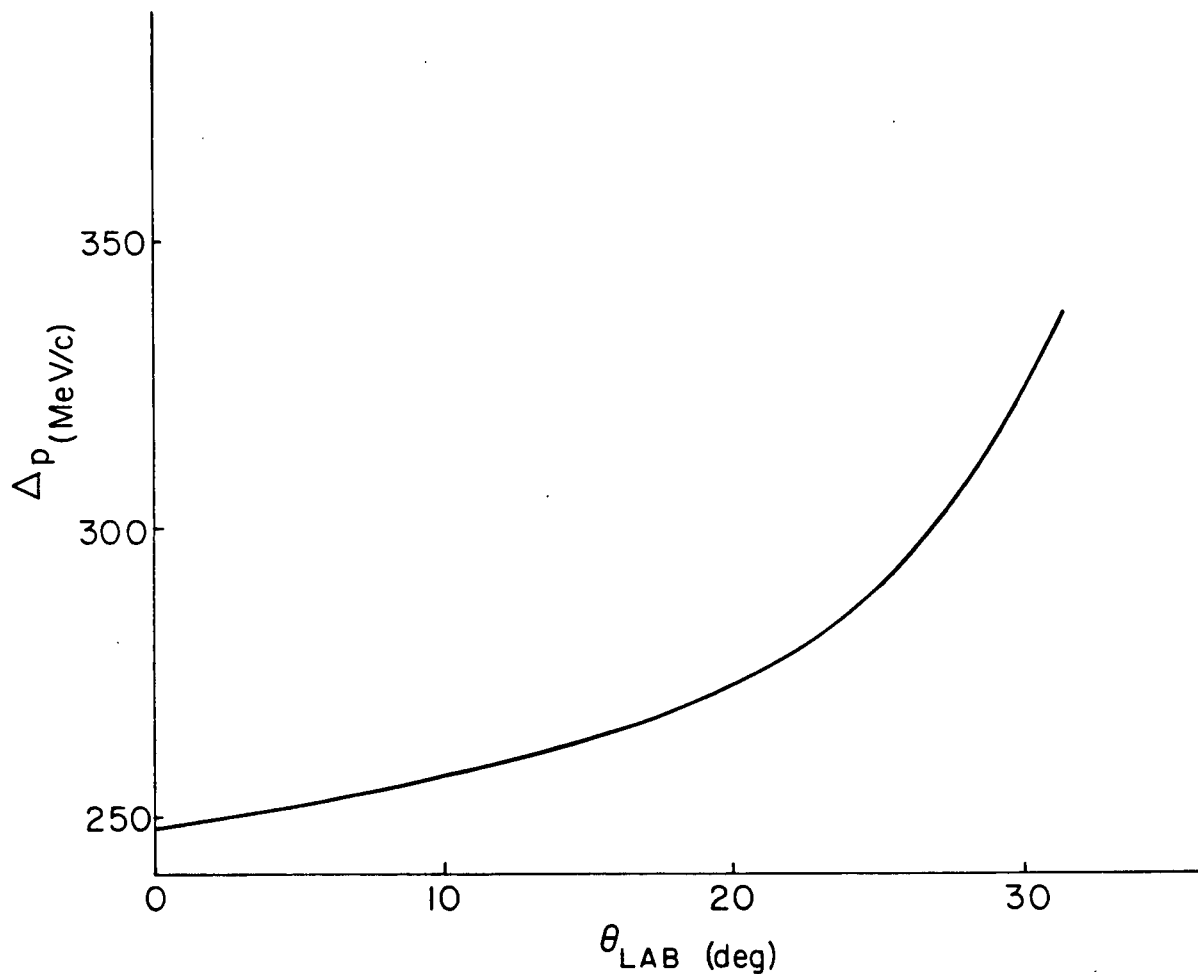


Fig 43. Momentum difference between elastic protons and most energetic inelastic protons. The difference is smallest near  $0^\circ$ , but is greater than the resolution of the spectrometer. As is discussed in the text, the separation was very clean.

the time of arrival of the incident neutron at the liquid hydrogen target with the momentum of the scattered particle, as shown in Fig 44. It is clearly shown that the tail of the beam separated from the inelastic protons from the liquid hydrogen.

The MWPC's performed a central role in the analysis of this data: their information was used to determine the momentum of each particle, as well as its path through the detector. The usage of the MWPC's was identical to that in the forward hemisphere measurement, except that the use of four MWPC's to determine the incoming and outgoing tracks to and from the magnet ensured enough redundancy to permit a very high efficiency for fitting tracks, typically 99.5%. Only horizontal coordinate information was used in the bulk processing; the vertical was used only for checks. The path information in the tracks helped eliminate three sources of background, as follows.

Profiles of the liquid hydrogen target were constructed with the front chamber data. As shown in Fig 45, the profiles were of sufficient resolution, at wider angles, to show the good subtraction of the empty target background. Loose cuts were applied to the profiles to eliminate obviously non-hydrogen associated events.

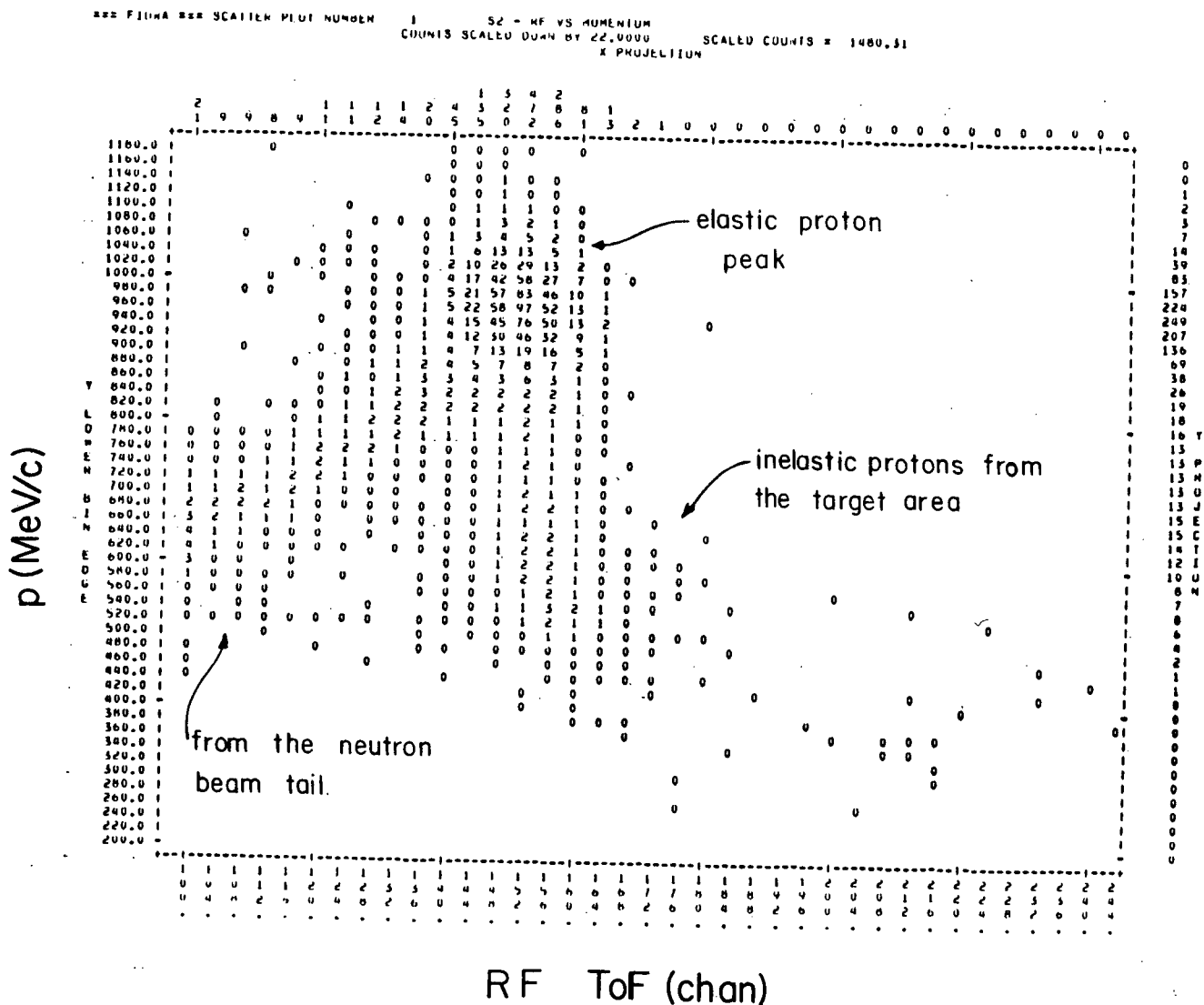


Fig 44. Correlation of momentum and RF-TOF. This data was taken at 10° and 418 MeV. The inelastic tail of the beam can be seen from the low TOF end approaching the elastic peak. The inelastics from the LH come directly down from the peak, with most of them being background events.

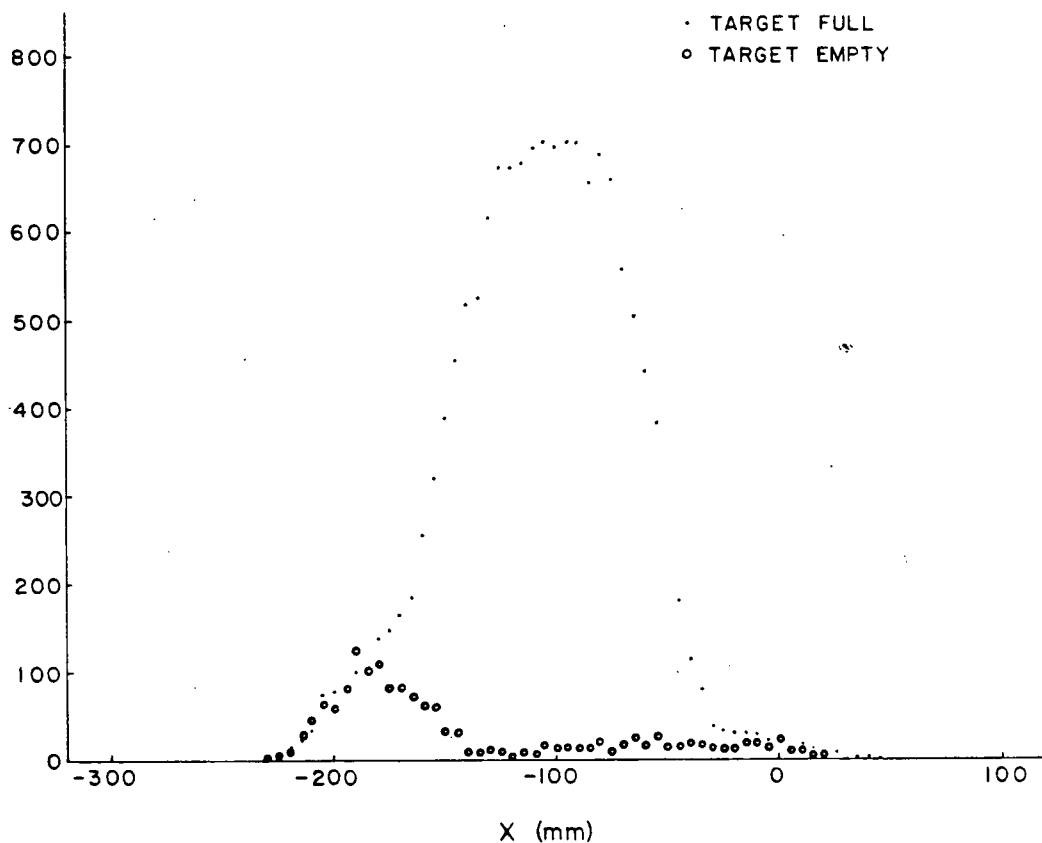


Fig 45. Profile of events from the liquid hydrogen target.

This profile shows that the majority of the background events from the target are due to the aluminium dome. The empty target data accurately measures the contamination of the target full data from this source.

It was also possible that particles would interact in the S2 counter, scatter into the magnet at some different angle of incidence, and give a false indication of its momentum. In a uniform magnetic field, the incoming and outgoing tracks, when extrapolated to the center of the field, would be very close to intersection. A test of this quantity would then indicate whether the incoming particle had deviated after the S2 counter. A plot of this intersection is shown in Fig 46.

It was found that the resolution of the spectrometer was approximately 8% FWHM. No improvement resulted in using the map of the magnetic field, so that a "block field" approximation was made in which the field was taken to be constant over the entire effective length. It was possible to remove the tail of the incident neutron beam artificially, via a RF TOF cut, to examine the inelastic events due to full energy neutrons. The momentum distribution is shown in Fig 47, illustrating that there is adequate separation between the two types, elastics and inelastics.

The calculated momentum was also used to correct the RF TOF for time of flight of the protons from the liquid hydrogen target to the detector. This was to permit the consistent usage of the calibrated monitors, in that the

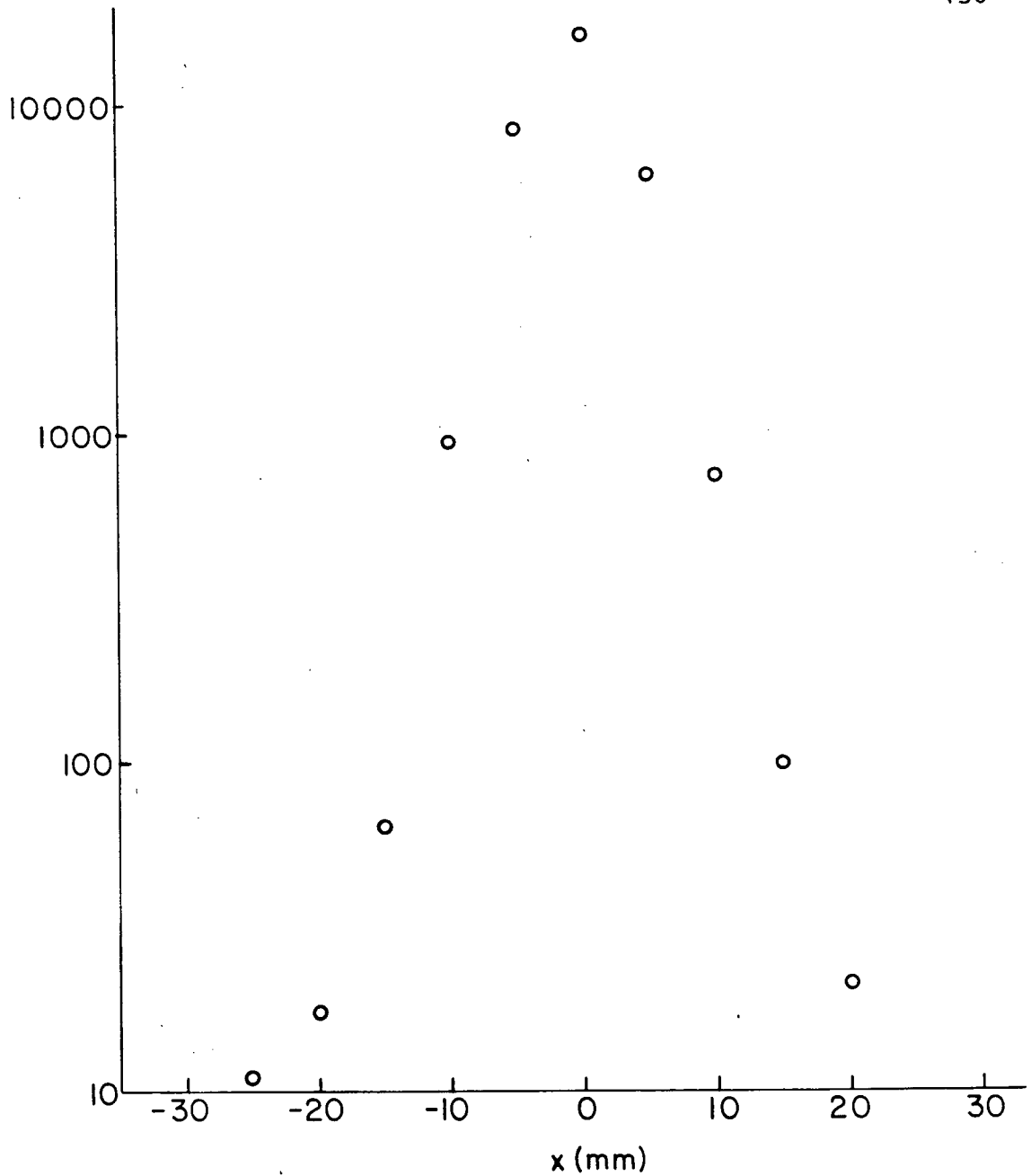


Fig 46. Intersection of tracks from the two halves of the spectrometer at the magnet center. Loose cuts were applied to the intersection of the front and back tracks to eliminate events where the particle interacted between the front and back MWPCs, which would give an inaccurate measure of the momentum. The cuts were applied at  $\pm 50$  mm.

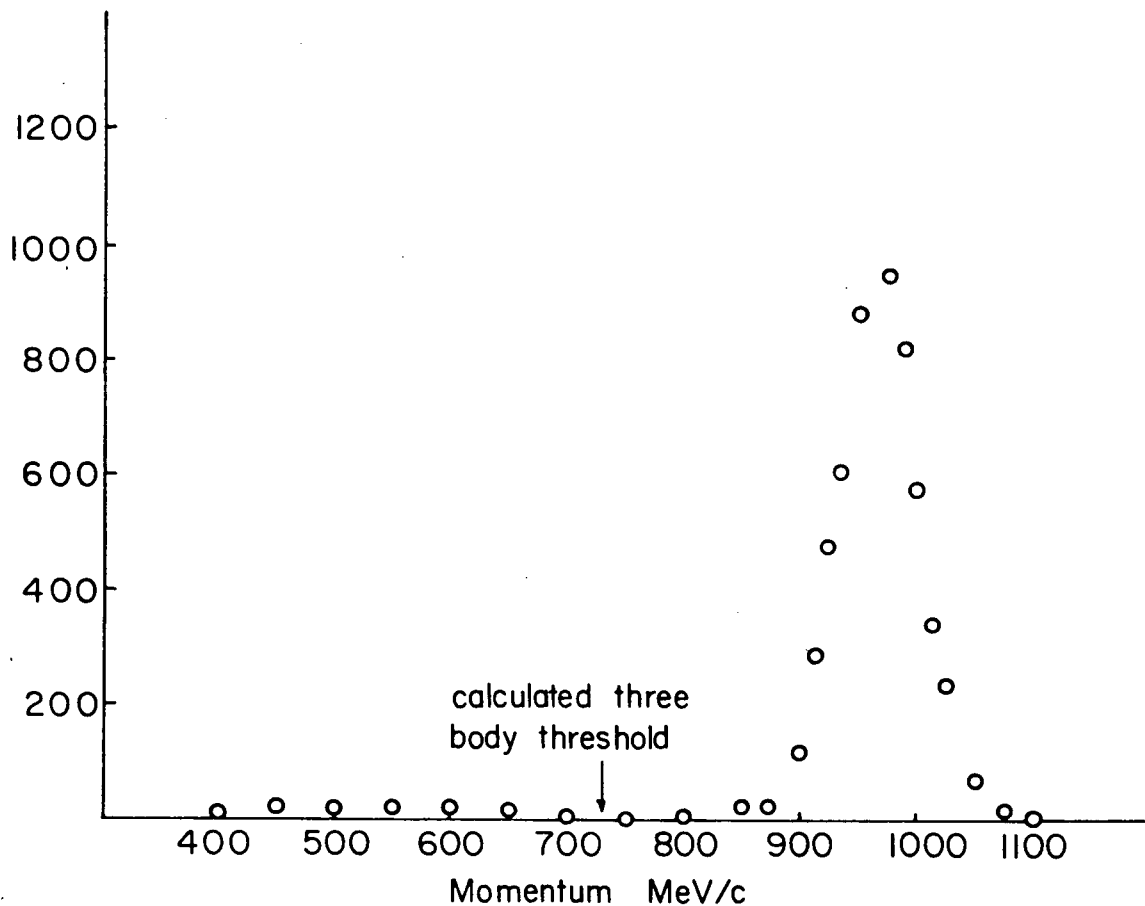


Fig 47. Momentum of the full energy elastic protons.

This data was taken at  $10^\circ$  and 418 MeV. The tail of the neutron beam was removed via an RF TOF cut, and a target subtraction was made to show the events coming from the liquid hydrogen. There is clean separation between the elastic and inelastic protons.

TOF cut in both cases referred to the incident beam distribution only.

#### IV.5.3 Total Energy Counter

As discussed previously, for large angles, the total energy counter S4 was used. Due to problems with the LH target at 212 MeV and range cutoffs for the large angle settings at 418 MeV, only the 60° (lab) setting at 418 MeV was actually used. The only source of background from the liquid hydrogen was due to pions, which were eliminated by correlating the pulse height in S4 with the TOF from S1 to S2. Fig 48 shows a typical scatter plot of these two quantities, illustrating the clean separation of the  $\pi$ 's from the protons.

Fig 49 shows a typical pulse height spectrum from S4. Only a small tail is evident, predominantly due to nuclear reactions in the scintillator.



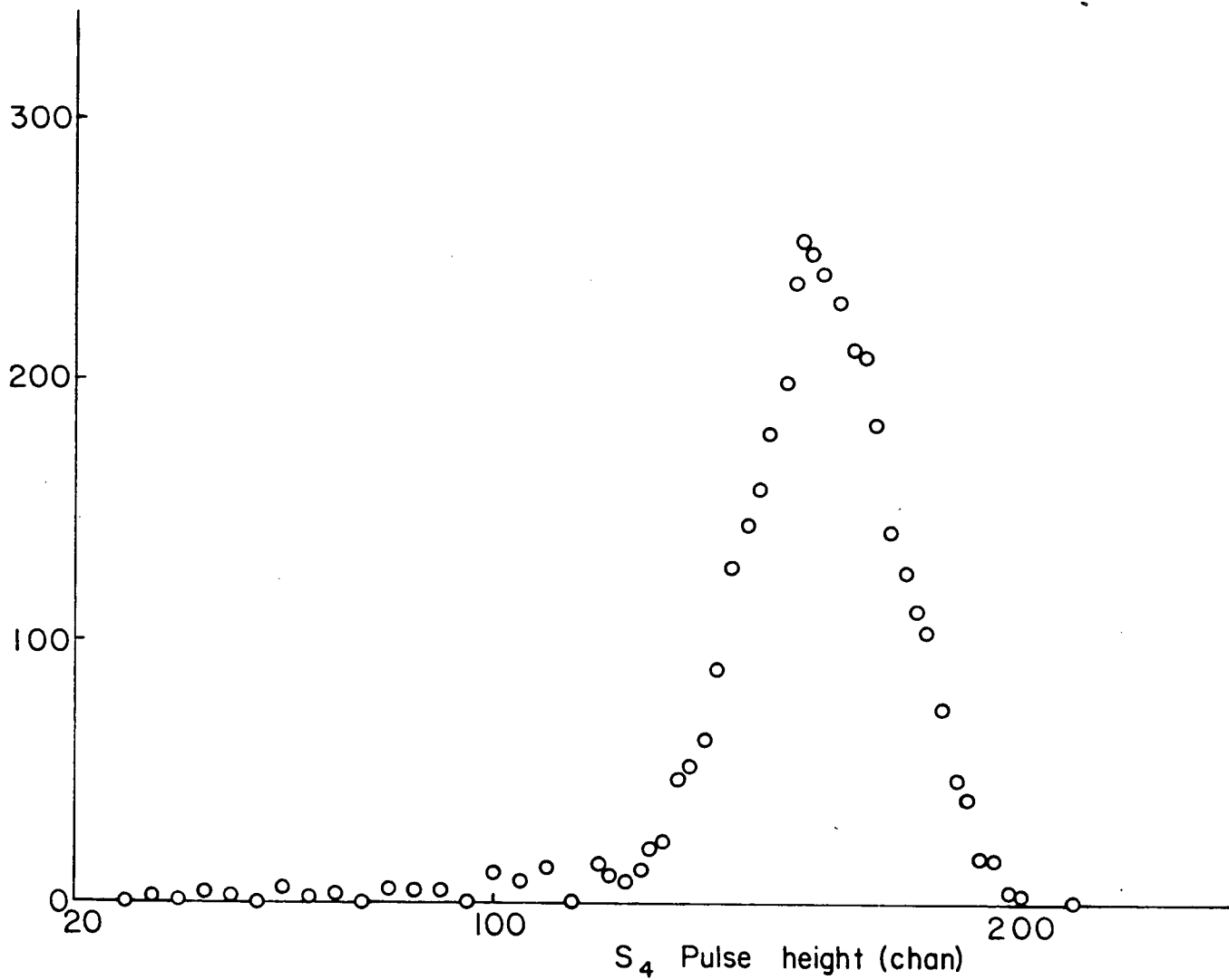


Fig 49. Pulse height in S4 for full energy protons.

#### IV.5.3 Reduction Of The Raw Data

The angular distributions were measured in 5° (lab) steps, from 2.5° - 60° at 418 MeV, and 5° - 55° at 212 MeV. Data runs which had known equipment failures and errors in the data taking were rejected in the analysis.

#### IV.5.4 Empty Target Data

A certain fraction of the events originated in the vessel supporting the hydrogen, as discussed previously for the forward hemisphere data. To a very good approximation, the rate for these events was independent of whether there was liquid in the flask or not. Fig 45 showed a typical pair of runs, normalized to the same incident flux, for the flask full and empty. The ratio of the empty to full rate was in the range 10-20%.

#### IV.5.6 Corrections To The Data Due To Equipment Aberrations

In the early runs of the 418 MeV data, it was found that the gas ballast region of the liquid hydrogen target was partially filling with liquid. The liquid level varied with time, decreasing with the target empty and increasing with it full. Thus the empty target data in those runs did not accurately measure the non-flask-hydrogen backgrounds which were present in the target full runs. Once this problem had been diagnosed and corrected, much of the 418 MeV data was retaken.

The variations in the target empty rates ranged from about 20-50%, and since this background formed about 10% of the signal, a 2-5% correction was required to account for the liquid in the ballast region. The effect was significant only in the angular range of about  $30^{\circ}$ - $60^{\circ}$  (lab), as data taking rates were lowest there. At small angles, the target was cycled often enough to erase the variation with time.

The problem was identifiable by two characteristics. When the target was empty, the event rate decreased rapidly with time. Also, histograms of the horizontal

profile of the LH target, from angles of greater than about  $40^\circ$ , showed a blurring of the events coming from the hydrogen, so that they appeared to merge with those from the aluminium dome. These two criteria were used to determine whether the effect was present.

It was found that this effect was not correctable. The settings which were affected were all of the total energy counter data at 212 MeV, and the first data sets of  $30^\circ$ ,  $35^\circ$ , and  $40^\circ$  at 418 MeV. These data have been removed from the analysis.

As the spectrometer was wheeled through the angular ranges for all the energies, the front of the detector became offset from the nominal scattering angles, by typically 5 cm. This offset was measured at every angle, allowing calculation of the scattering angles. The effect on the solid angle of rotating the counters slightly in this way was completely negligible.

#### IV.5.7 Corrections To The Raw Data

The data represent the fraction of the incident neutron flux which was scattered into the spectrometer. As discussed previously for the calibration data, corrections were required for this data to account for multiple scattering and attenuation of the protons. These corrections are listed in Table 18.

On average, the spectrometer range cutoff was about 60-65 MeV, i.e. protons scattered from the center of the hydrogen target with less than about this value would have insufficient energy to reach P2. Range cutoffs were calculated to begin at 73° and 52° CM at 212 and 418 MeV, respectively, well beyond the range of data used in this analysis.

As for the forward hemisphere data, these data were corrected for attenuation of the neutron beam to the target center, and for gas in the target when it was nominally empty.

Neutron Beam Energy (MeV)	$\theta^*$ (deg)	Correction (Multiplicative)
212	60	0.995
	70	0.986
	80	0.985
	90	0.990
	100	0.995
	110	0.999
	120	1.0033
	130	1.0064
	140	1.0087
	150	1.011
	160	1.012
	170	1.014
	180	1.016
418	50	1.0086
	60	1.0018
	70	0.998
	80	0.995
	90	0.995
	100	0.993
	110	0.992
	120	0.998
	130	1.003
	140	1.008
	150	1.011
	160	1.014
	170	1.017
180	1.019	

Table 18. Calculated corrections to the data.

The multiple scattering and attenuation corrections as functions of scattering angle for the spectrometer data are listed.

#### IV.5.8 Parameters Needed To Calculate $d\sigma/d\Omega$

As discussed in Chapter II, the differential cross section is calculated from the expression

$$N_p(\theta) = \frac{N_{mon}(\theta)}{\eta(E_i)} n_t t \frac{d\sigma}{d\Omega_{CM}} \frac{d\Omega_{CM}}{d\Omega_{LAB}} d\Omega$$

where the transformation to the center of mass has been made via the Jacobian  $d\Omega_{CM}/d\Omega_{LAB}$ .

The quantities remaining to be determined are  $d\Omega$  and  $\langle\theta\rangle$ , the average laboratory scattering angle for each angular bin. The area density and length of the target has already been discussed.

The angular binning of the data was determined by the geometry of the four S2 counters. This avoided the necessity of calculating the acceptance of the spectrometer, with the angles determined by the MWPC's. It introduced the problem of calculating the average scattering angles for each counter. The average angle was obtained by performing a similar integration to that of the forward hemisphere data and is shown as a function of nominal angle in Fig 50.

The solid angle subtended by the detector counters was calculated in a similar fashion to that for the

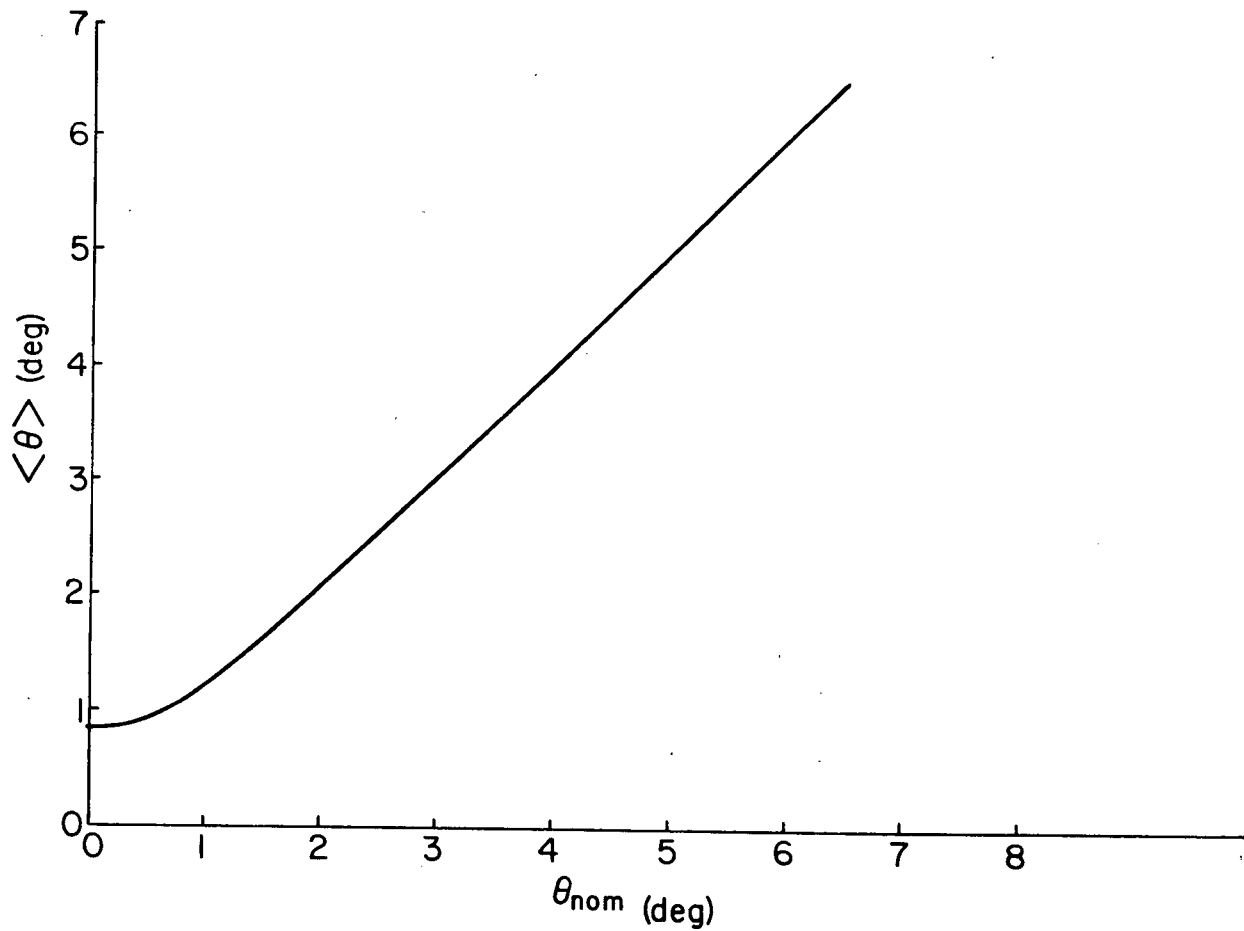


Fig 50. Average polar scattering angle.  
The average polar scattering deviates from the nominal scattering near  $0^\circ$ . This variation disappears above  $5^\circ$ .

forward hemisphere data.  $d\Omega$  was closely  $A/r^2$ , i.e. the solid angle subtended by an area  $A$  at a distance  $r$  from a point, and was calculated to be 2.794 msr for each S2 counter.

#### IV.5.9 Error Estimation

As demonstrated in the discussion of the analysis, particle identification and selection of elastically scattered protons from liquid hydrogen were unambiguously performed. As such, there was negligible error involved in those cuts.

As for the forward hemisphere data, the sources of error were the RF cuts, monitor stability and the solid angle determination. Table 19 shows a plot of the change in the proton yield for variations in the RF cut. An error of about  $\pm 0.5\%$  was associated with a  $\pm 2$  channel jitter on the cut. Adding the three sources of error in quadrature gives an error of 1.2% and 0.8% at 418 and 212 MeV, respectively. As will be discussed later in the text, the phase shift analysis of the two 418 MeV data sets indicated that the second set involved more internal jitter than was expected from the sources listed above. A further error of 1% was added in to this data in order to

<u>RF TOF Cuts</u>	
<u>lower cut limit</u>	<u>signal</u>
<u>+ x (chan)</u>	<u>(arb. units)</u>
0	0.4949 $\pm$ 0.0075
2	0.4911
4	0.4875
6	0.4824
-2	0.4979
-4	0.5000
-6	0.5021

Table 19. Sensitivity of the backward differential cross section to the RF cuts.

reduce its  $\chi^2$ , close to unity in the fit. The 212 MeV data was also found to require this correction. The sources of this error remain unknown, although it could well have been due to small instabilities in the cyclotron or the monitors.

The RF distribution was found to be the dominant source of error in the normalization of the backward data. The 55° (lab) settings in both data sets differ by about 7% in normalization. The only cause found for this difference was a slightly different shape of the RF distributions for the two data sets.

The phase shift fits indicate that the two 418 MeV data sets have overall normalizations that differ by about 2%. Removing this 2%, and halving the remainder of the difference yields an estimate of  $\pm 2.5\%$  error in the normalization to the RF distribution.

#### IV.5.10 Angular Distributions

The backward hemisphere results are listed in Tables 20 and 21. The full angular distributions are shown in Figs 51 and 53, while the previous data are shown in Figs 52 and 54, for 212 and 418 MeV, respectively. These data will be discussed and compared in the next chapter.

The distributions are asymmetric about  $90^\circ$  CM and show peaking in the extreme forward and backward regions. In addition, structure can be seen in the backward hemisphere.

The asymmetry is due to the contributions of the  $I=0$  and  $I=1$  amplitudes. Were one absent, the distributions would be as those for identical particles - symmetric. The peaking can be attributed to the exchange of pions:  $\pi^0$  in the extreme forward peak, and  $\pi^\pm$  in the extreme backward (or charge exchange region). The structure in the backward region suggests the exchange of heavier mesons as the scattering becomes less peripheral.

C OF E ANGLE	CROSS SECTION	ERRCR
119.2	3.054	0.061
121.1	3.306	0.064
123.1	3.344	0.064
125.1	3.466	0.066
119.2	2.786	0.058
121.1	3.102	0.061
123.1	3.258	0.062
125.1	3.397	0.065
129.5	3.916	0.060
131.4	4.104	0.062
133.4	4.250	0.063
135.4	4.411	0.065
140.3	5.002	0.076
142.2	5.123	0.077
144.2	5.341	0.080
146.2	5.608	0.083
150.7	5.981	0.090
152.7	6.219	0.093
154.7	6.396	0.095
156.7	6.680	0.098
161.4	7.491	0.110
163.4	7.857	0.115
165.4	8.373	0.121
167.4	9.016	0.130
171.8	10.398	0.187
173.7	11.038	0.197
175.6	11.393	0.201
177.4	11.708	0.206
98.8	1.876	0.030
100.7	1.925	0.031
102.6	1.980	0.031
104.5	2.080	0.033
88.6	1.608	0.034
90.4	1.589	0.034
92.3	1.639	0.034
94.3	1.650	0.034
108.8	2.413	0.041
110.7	2.530	0.042
112.7	2.649	0.044
114.7	2.738	0.044

Table 20. Backward hemisphere differential cross section at 212 MeV.

	C OF $\theta$ ANGLE	CROSS SECTION	ERROR	C OF $\theta$ ANGLE	CROSS SECTION	ERROR	
	138.6	3.072	0.048	138.2	3.049	0.055	
	140.6	3.255	0.049	140.2	3.214	0.058	
	142.7	3.416	0.051	142.3	3.371	0.059	
	144.8	3.611	0.054	144.4	3.673	0.064	
	149.5	3.951	0.061	149.3	4.009	0.072	
	151.5	4.144	0.063	151.3	4.228	0.076	
	153.6	4.304	0.065	153.4	4.420	0.079	
	155.7	4.541	0.067	155.5	4.727	0.083	
	127.5	2.234	0.040	126.5	2.180	0.041	
	130.0	2.330	0.041	128.9	2.384	0.044	
	132.0	2.508	0.043	131.0	2.505	0.046	
	134.0	2.625	0.044	133.0	2.681	0.048	
	160.4	5.191	0.075	116.6	1.613	0.032	
	162.5	5.438	0.078	118.6	1.731	0.034	
	164.6	5.753	0.082	120.6	1.778	0.035	
	166.6	6.461	0.090	122.6	1.921	0.036	
	86.5	1.489	0.042	106.5	1.396	0.028	
	88.4	1.355	0.040	108.5	1.412	0.028	
	90.3	1.303	0.039	110.4	1.505	0.029	
	92.2	1.366	0.040	112.4	1.498	0.029	
1st set	171.3	6.003	0.132	95.7	1.367	0.027	2nd set
	173.4	6.924	0.144	97.6	1.327	0.027	
	175.4	9.688	0.153	99.5	1.390	0.027	
	177.2	10.361	0.161	101.5	1.395	0.027	
	66.5	1.997	0.042	160.3	5.096	0.093	
	68.7	1.943	0.041	162.4	5.438	0.098	
	70.5	1.838	0.039	164.5	5.927	0.105	
	72.4	1.750	0.037	166.5	6.485	0.113	
	57.3	2.413	0.045	165.7	6.135	0.121	
	59.1	2.346	0.044	167.8	6.624	0.129	
	60.5	2.350	0.043	169.8	7.774	0.148	
	62.7	2.191	0.041	171.9	8.451	0.159	
	76.8	1.651	0.035	171.3	7.980	0.181	
	78.7	1.575	0.035	173.4	6.740	0.201	
	80.5	1.534	0.034	175.4	9.841	0.219	
	82.4	1.523	0.033	177.2	10.137	0.228	
	117.2	1.515	0.034	176.6	10.179	0.210	
	119.2	1.648	0.035	177.9	10.547	0.216	
	121.2	1.788	0.037	176.4	10.010	0.207	
	123.2	1.808	0.037	65.9	2.174	0.046	
	106.6	1.432	0.028	67.7	2.083	0.044	
	108.8	1.483	0.029	69.5	2.000	0.043	
	110.8	1.508	0.029	71.4	1.925	0.041	
	112.8	1.522	0.029				
	* 57.2	2.419	0.055				
	** 59.0	2.311	0.052				
	* 60.8	2.292	0.052				
	* 62.7	2.163	0.049				

Table 21. Backward hemisphere differential cross section at 418 MeV.

The two sets of data taken at this energy are shown. Data taken with the total energy counter are marked with a \*.

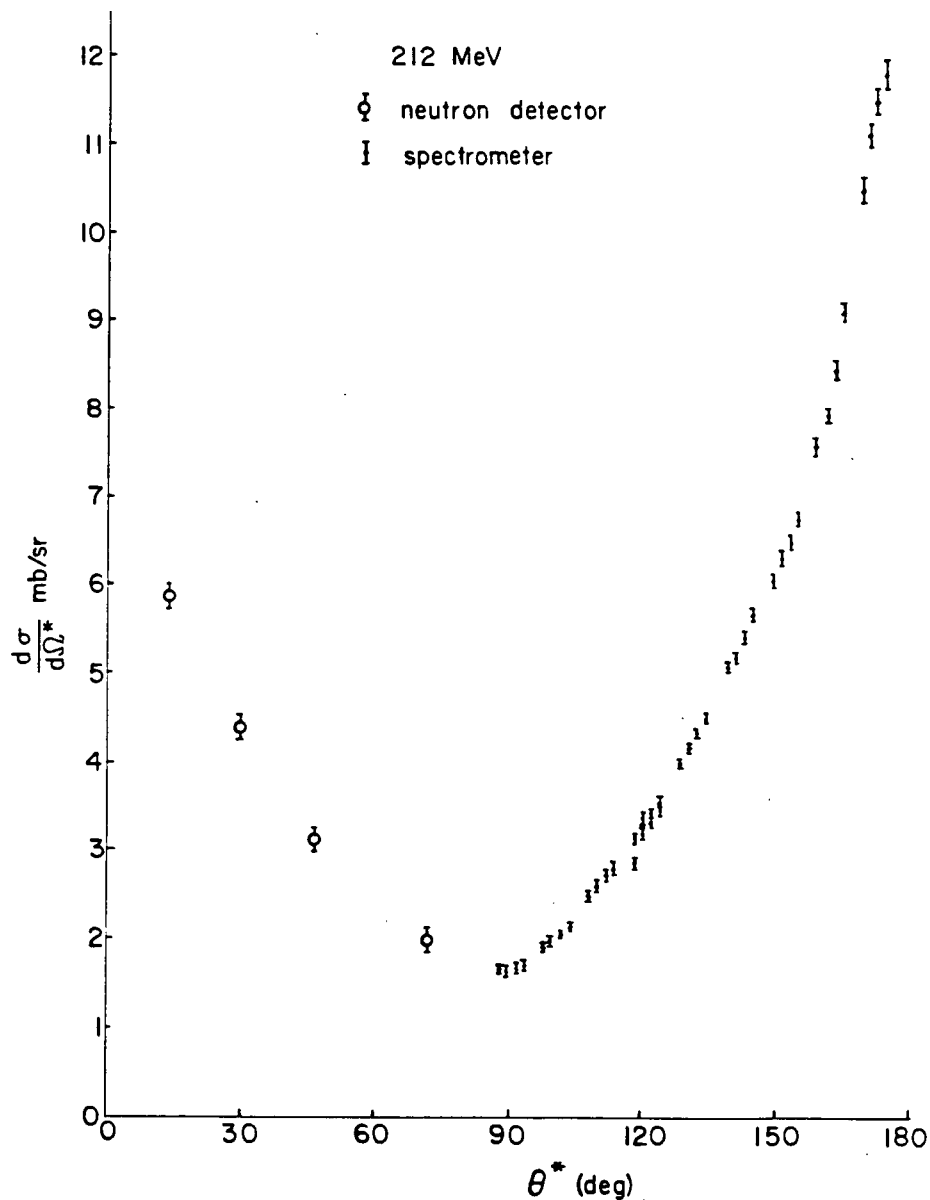


Fig 51. Backward hemisphere differential cross section at 212 MeV. There was no overlap of the forward and backward hemisphere data sets due to problems with the hydrogen target. Phase shift analysis fits indicate that the two sets are consistent in their normalization.

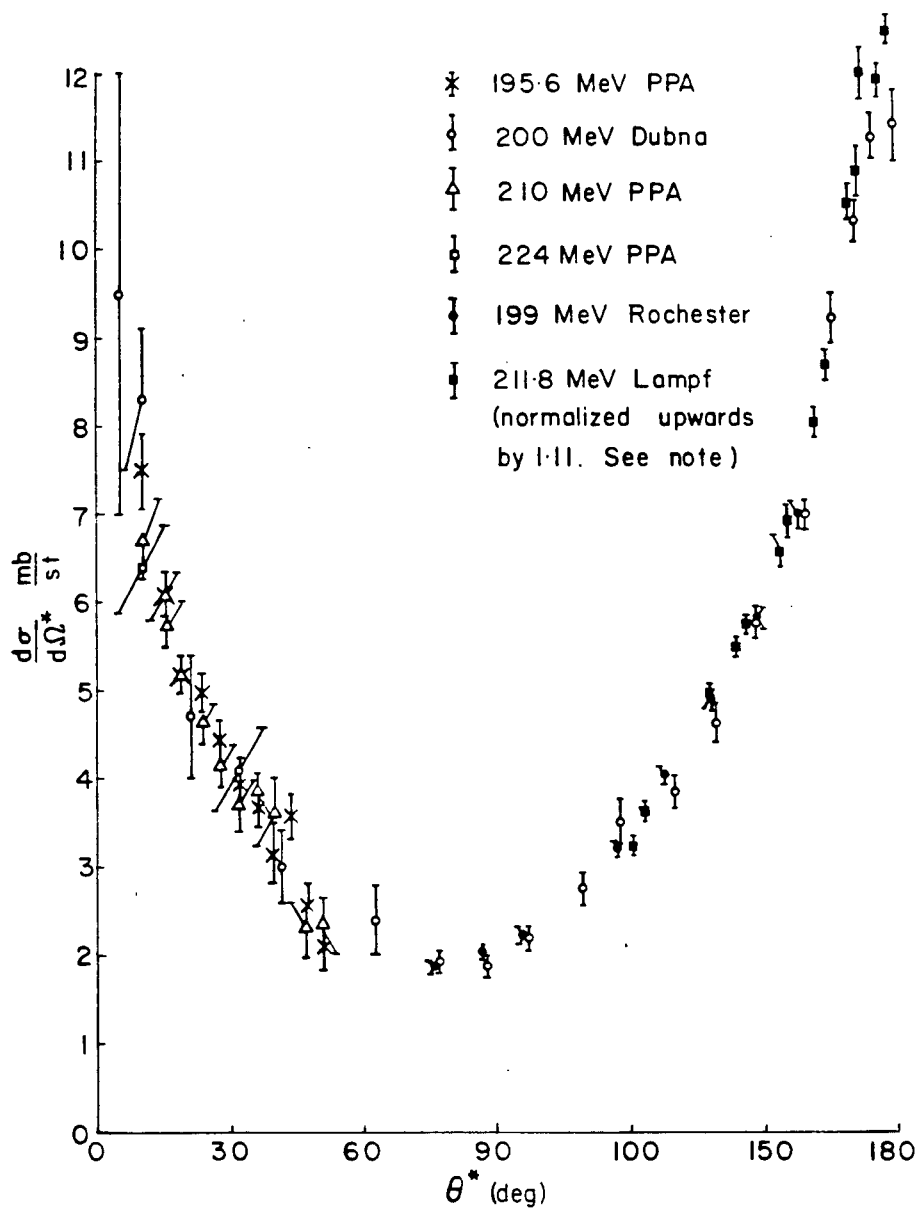


Fig 52. Previous backward hemisphere differential cross section data near 212 MeV.  
 Phase shift analysis of the data set indicates that the relatively normalized Lampf data should be renormalized upwards by 11%.

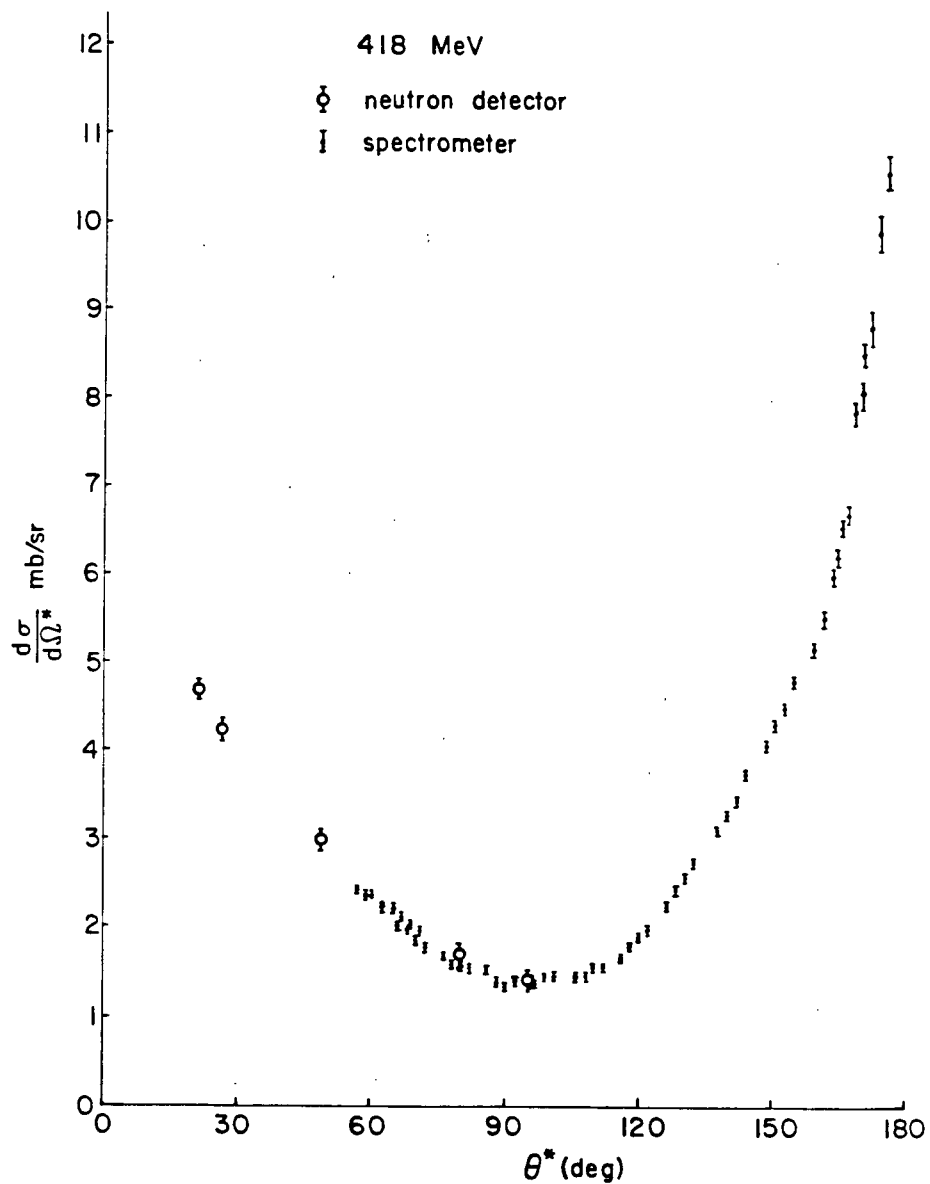


Fig 53. Backward hemisphere differential cross section at 418 MeV.

Due to the amount of data in the backward hemisphere, only one set of data is shown for each laboratory angle setting. There is good overlap of the forward and backward hemisphere data sets.

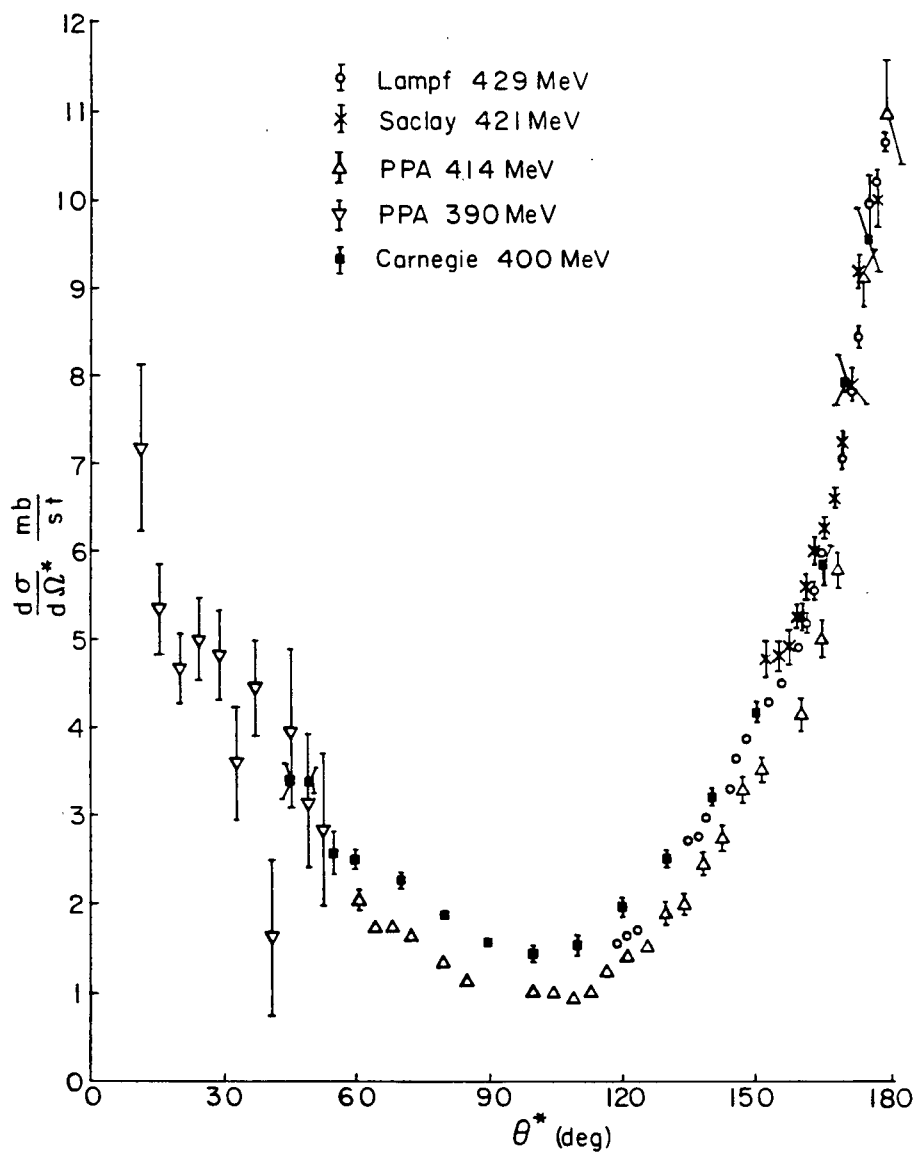


Fig 54. Previous backward hemisphere differential cross section data near 418 MeV.  
 The PPA data at 414 MeV disagree strongly in shape and normalization with other data. They have been removed from the data set.

#### IV.6 IN RESTROPECT

Looking back on the experiment, it is clear that there were features of it which could have been improved. Overall, the results were limited by the stability of the cyclotron and of the neutron beam monitors.

The results depended on the constancy of the RF bunch widths between the forward and backward hemisphere data taking. A competing factor here was the wide bunch width required for high intensity production of mesons on BL 1, so the solution to this problem would probably lie in dedicated running for neutron experiments or the (doubtful) introduction of a medium intensity beamline in the meson hall so that running conditions would be well matched and allow a narrow, stable bunch width. The monitor stability could likely be improved by including one or two more scintillators in each arm. This would reduce the monitors' sensitivity to low energy backgrounds.

An unfortunate drawback to the technique used in the forward hemisphere measurement was the very low efficiency of the neutron detector, which fell from about 1.4% at the highest energy to about 0.3% at the lowest. This as a factor 4 less than what was expected from the Los Alamos

data for a similar setup<sup>34</sup> (on which the technique for this experiment was based). The efficiency could be increased by using a CH<sub>2</sub> converter, which partially avoids the "nuclear screening" of carbon nucleons by having the "free" hydrogen. This could give a factor 2-4 increase.

A significant source of background in the experiment originated from the aluminium dome surrounding the hydrogen target. As shown with the spectrometer, most of the background of protons came from there. If that was also true for neutrons in the forward hemisphere measurement, the removal of this dome would greatly reduce the backgrounds. Self-supporting mylar-and-styrofoam targets are now available.

#### IV.7 COMPARISON OF EXPERIMENTAL TECHNIQUES

It is instructive to make a comparison of the techniques used in the experiment with those previously used to perform similar measurements.

Previous measurements of the forward hemisphere used either thick scintillators or a conversion method, as done here. Use of scintillators has two advantages: the detection efficiency can be high (typically 20%) and it

has only a slow variation with energy over the range 100-500 MeV. This is to be contrasted with the low, very energy-dependent efficiencies obtained with a converter.

The converter method gains the overall advantage in other areas. The active area can be limited, eliminating edge effects. This also gives an accurate determination of the solid angle subtended by the counter. The active area can be measured to about  $\pm 1$  mm, whereas by timing in large scintillators, accuracies of cm's are obtained. Finally, the trigger timing from the converted charged particles will have less jitter than from a large volume scintillator.

Turning now to the detection of protons, the techniques used are either thick scintillators, magnetic spectrometers, or range telescopes. Below the inelastic threshold, all three techniques are comparable, though the scintillators suffer somewhat from straggling and nuclear reactions. Above the threshold, the range technique fails to provide particle identification and good energy resolution for selecting elastic protons. At high energies, the spectrometer is best due to its simplicity.

## V. INTERPRETATION OF THE DATA

As discussed in the Introduction, information can be obtained on the N-N scattering amplitudes through phenomenological phase shift analyses. This chapter will describe the current state of the PSA and the inclusion of the data from this experiment into the world data set.

### V.1 PRINCIPLE OF PHASE SHIFT ANALYSIS

The formalism of scattering theory has been extensively described<sup>35</sup>, and an excellent summary of the formalism describing the R-matrix and N-N phase shifts has been given in Ref. 36, in which the possible transitions between the allowed states in the N-N system is parametrized by scattering phase shifts.

It is convenient to describe the scattering theory in terms of an angular momentum expansion: all approximations are automatically unitary, and the expansion can be cut off at a given l-value with the higher phases calculated from heavy boson exchange (HBE) theory<sup>37</sup>.

The Hamiltonian for N-N scattering conserves total angular momentum, parity, time reversal (TRI) and isospin. As a consequence of these symmetries, it follows that total spin is conserved as well. From the extended Pauli exclusion principle, the total wave-function for the N-N system must be totally anti-symmetric, which leads to the condition

$$(-1)^{\ell+s+I} = -1$$

Coupled with the symmetries of the Hamiltonian, this equation gives the allowed states of the N-N system and the possible transitions. In spectroscopic notation these are, for  $I=0$

$${}^3S_1, {}^1P_1, {}^3D_1, {}^3D_2, {}^3D_3, {}^1F_3, {}^3G_3, {}^3G_4, {}^3G_5, {}^1H_5, {}^3I_5, {}^3I_6, {}^3I_7, \dots$$

and for  $I=1$

$${}^1S_0, {}^3P_0, {}^3P_1, {}^3P_2, {}^1D_2, {}^3F_2, {}^3F_3, {}^3F_4, {}^1G_4, {}^3H_4, {}^3H_5, {}^3H_6, {}^1I_6, \dots$$

The notation used is

$${}^{2s+1}l_j$$

with  $l = 0, 1, 2, 3, 4, 5, \dots$  corresponding to S, P, D, F, G, H,  $\dots$

The allowed transitions are for the cases of

scattering of the state  $|pjls\rangle$  into the state  $|p'jl's\rangle$  of

$$l'=j \quad \langle \text{----} \rangle \quad l=j \quad ; \quad s=0$$

$$l'=j \quad \langle \text{----} \rangle \quad l=j \quad ; \quad s=1$$

$$l'=j\pm 1 \quad \langle \text{----} \rangle \quad l=j\pm 1 \quad ; \quad s=1$$

$$l'=j\pm 1 \quad \langle \text{----} \rangle \quad l=j \mp 1 \quad ; \quad s=1$$

The amplitudes for these last two transitions are equal if TRI holds. Furthermore, the last four are not diagonal with respect to the angular momentum,  $l$ , which results in mixing of the states involved, i.e. those of equal  $j$  and  $s$  but unequal  $l$ . Two new eigenstates can be generated by a unitary transformation, which involve a mixing parameter,  $\xi_j$ , for each  $j$  value<sup>30</sup>.

The phase shifts describing the scattering are quoted in the same spectroscopic notation as for the states. The two new eigenstates are quoted by their  $l'$  value of either  $j-1$  or  $j+1$ .

Above the pion production threshold, there can be inelastic scattering, which is characterized by the phase shifts becoming complex. As they are written as

$$e^{i\delta}$$

when complex they become

$$\eta e^{i\delta}$$

where

$$0 \leq \eta \leq 1$$

Therefore, the N-N scattering can be described by phase shifts as in the above notation, mixing parameters and inelasticities.

The most general form of the scattering matrix satisfying the previously discussed symmetries can be written in the form<sup>39</sup>

$$M = a + b (\sigma_n^{(1)} - \sigma_n^{(2)}) + c (\sigma_n^{(1)} + \sigma_n^{(2)}) + m \sigma_n^{(1)} \sigma_n^{(2)} + g (\sigma_p^{(1)} \sigma_p^{(2)} + \sigma_k^{(1)} \sigma_k^{(2)}) + h (\sigma_p^{(1)} \sigma_p^{(2)} - \sigma_k^{(1)} \sigma_k^{(2)})$$

where  $a, b, c, m, g$  and  $h$  are the complex Wolfenstein amplitudes,  $n, K$ , and  $P$  form an orthogonal vector set in the center of mass system, and the  $\sigma_i$  are the Pauli spin matrices. The amplitude  $b$  expresses the degree of isospin violation in the N-N system (primarily due to electromagnetic effects).

Hoshizaki<sup>39</sup> has compiled the formulae required to calculate N-N observables using this form of  $M$ . The object of the phase shift analysis is to calculate the observables from initial guesses for the phase shifts and iterate the guesses until the best fit is obtained for the

data. The fitting criterion is the  $\chi^2$

$$\chi^2 = \sum \left( \frac{\text{fitted}}{\text{observables}} - \text{data} \right)^2 / (\text{error})^2$$

which is to be minimized.

## V.2 CURRENT STATUS OF THE PHASE SHIFT ANALYSIS

A phase shift analysis has been developed to incorporate the TRIUMF N-N elastic scattering data into the world data set to determine the phase shifts. Single energy analyses have been performed which group data around four energies in the energy range 200-500 MeV. The ones at 212 and 418 MeV will be described here. The details of the analysis have been well described in Refs 40 and 41, with the world data used listed in Ref 41. The PPA<sup>47</sup> data at 414 MeV has been excluded since it differs significantly in shape and normalization from those of Bonner et al.<sup>42</sup> and Bizard et al.<sup>43</sup>. Recent spin correlation data from SIN<sup>55</sup> at 446 MeV has been added to the data set.

The angular momentum expansion was cut off at H waves for the I=0 phases and I waves for I=1. The higher waves were fixed at the prescription of Vinh Mau et al.<sup>37</sup>, using OPE and HBE potentials.

At 212 MeV, below the inelastic threshold, no inelasticity was allowed. At 418 MeV using the isobar model<sup>44</sup>, all inelasticity is assumed to be in the I=1 phases via delta production. Assuming that the delta and N are in a relative s state, the lowest available N-N state which can couple to it is the  $^1D_2$  state. Inelasticities have been calculated from the model of Green and Sainio<sup>45</sup>. Only the  $^1D_2$  phase was allowed to have variable inelasticity. It has been found that if more phases are permitted to have variable inelasticity, the phase shift analysis becomes unstable and cannot unravel the correlations between the various inelasticities.

The phase shifts which result from this analysis are listed in Table 22. The errors quoted are calculated from

$$\sqrt{\chi^2_{\nu} \epsilon_{jj}}$$

where  $\chi^2_{\nu}$  is the  $\chi^2$  per point of the fit and  $\epsilon_{jj}$  is the diagonal element of the error matrix for the j th parameter. Since the  $\chi^2_{\nu}$  of the fit were always greater than unity, the errors in the parameters were increased to account for the quality of the fit. The large values of  $\chi^2_{\nu}$  suggest that there is still some erroneous data in the set. Note that using  $\epsilon_{jj}$  gives only an estimate of the

212 MeV

Phase	l	Value (deg)	Phase	l	Value (deg)
$^3S_1$	0	$17.71 \pm 0.84$	$^3P_0$	1	$-1.83 \pm 0.56$
$\epsilon_1$		$4.08 \pm 0.49$	$^1S_0$		$4.53 \pm 0.59$
$^3D_1$		$-18.94 \pm 0.68$	$^3P_1$		$-22.69 \pm 0.21$
$^1P_1$		$-23.50 \pm 0.89$	$^3P_2$		$16.18 \pm 0.16$
$^3D_2$		$28.00 \pm 0.64$	$\bar{\epsilon}_2$		$-2.87 \pm 0.10$
$^3D_3$		$5.11 \pm 0.42$	$^3F_2$		$1.03 \pm 0.24$
$\bar{\epsilon}_3$		$5.15 \pm 0.27$	$^1D_2$		$7.34 \pm 0.22$
$^3G_3$		$-3.05 \pm 0.38$	$^3F_3$		$-2.66 \pm 0.17$
$^1F_3$		$-2.27 \pm 0.40$	$^3F_4$		$1.69 \pm 0.13$
$^3G_4$		$4.94 \pm 0.44$	$\bar{\epsilon}_4$		$-1.17 \pm 0.06$
$^3G_5$		$0.36 \pm 0.33$	$^3H_4$		$0.33 \pm 0.05$
			$^1G_4$		$1.06 \pm 0.08$
			$^3H_5$		$-0.86 \pm 0.05$
			$^3H_6$		$0.19 \pm 0.05$

418 MeV

Phase	l	Value (deg)	Phase	l	Value (deg)
$^3S_1$	0	$-6.36 \pm 0.94$	$^3P_0$	1	$-20.35 \pm 0.58$
$\epsilon_1$		$7.33 \pm 0.63$	$^1S_0$		$-19.58 \pm 0.46$
$^3D_1$		$-25.32 \pm 0.53$	$^3P_1$		$-35.85 \pm 0.30$
$^1P_1$		$-38.69 \pm 1.13$	$^3P_2$		$18.26 \pm 0.17$
$^3D_2$		$22.64 \pm 0.71$	$\bar{\epsilon}_2$		$-2.29 \pm 0.16$
$^3D_3$		$4.09 \pm 0.37$	$^3F_2$		$0.30 \pm 0.19$
$\bar{\epsilon}_3$		$7.35 \pm 0.30$	$^1D_2$		$11.61 \pm 0.14$
$^3G_3$		$-4.88 \pm 0.42$	$^3F_3$		$-2.60 \pm 0.19$
$^1F_3$		$-4.97 \pm 0.27$	$^3F_4$		$3.54 \pm 0.10$
$^3G_4$		$6.78 \pm 0.51$	$\bar{\epsilon}_4$		$-1.68 \pm 0.10$
$^3G_5$		$-1.68 \pm 0.29$	$^3H_4$		$0.75 \pm 0.07$
			$^1G_4$		$2.22 \pm 0.10$
			$^3H_5$		$-1.28 \pm 0.10$
			$^3H_6$		$0.66 \pm 0.07$

Table 22. Phase shifts predicted from the previous data at 212 and 418 MeV. These analyses included all the BASQUE spin dependent data.

error. The errors also do not account for possible inconsistencies in the treatment of the inelasticities at 418 MeV.

### V.3 NEW DATA IN THE PHASE SHIFT ANALYSIS

The phase shift analysis of data provides not only an estimate of the phases, but also a quantitative comparison of the individual data sets used in the analysis. This will be used to discuss the the shape and normalization of the various cross section data near 212 and 418 MeV.

#### V.2.1 Data Near 212 MeV

In the forward hemisphere alone, data is from PPA<sup>46</sup> entirely. In the backward hemisphere, there is data from EPA<sup>47</sup>, Rochester<sup>48</sup>, and relatively normalized data from Lampf<sup>42</sup>. Over the entire range, there is a measurement from Dubna<sup>49</sup>, which was normalized to their measurement of the total cross section.

In the analysis, data sets are assigned an overall normalization (and error) which can be varied to give an overall fit to the data. From a calculation of the  $\chi^2$  of

individual data from the fit, a quantitative measure of the agreement between the data sets is obtained.

Our forward and backward hemisphere data sets were put into the analysis with separate normalizations in order to verify that the fits would leave them equal, within the error limits set.

In the fit, our backward hemisphere data had a  $\chi^2$  of 1.3, indicating that there was some jitter in the data not yet accounted for. The error bars were increased by 1% to lower the  $\chi^2$  close to unity.

Without our data, all the cross section data sets are in reasonable agreement, whereas the introduction of our data shows up disagreement with the two data sets which cover the 75°-125° (cm) range. These are the data from Dubna and Rochester. The shape of our data is in good agreement with the Lampf data down to 120°, suggesting that the older data sets are faulty. This is not surprising for the Dubna data where the separate measurements of the forward and backward hemisphere were made to be equal at 67°. Any error in this data would show up as a shape error in this region.

The final phase shift analysis at this energy was performed leaving the Dubna data out entirely, and

excluding the Rochester data in the  $75^{\circ}$ - $125^{\circ}$  range. Our recent measurement of the total cross section was also included. The fit gave a  $\chi^2_{\nu}$  of 1.6 for 271 data and 25 parameters, indicating that there are still some internal inconsistencies in the data set. The total cross section provides a strong constraint on the normalizations of the differential cross section data, since the analysis will attempt to shift them so that the integrated differential cross section fits the measured value. In order to do this, the analysis renormalized upwards all the  $d\sigma/d\Omega$  data, by 3% for the Rochester and PPA data, 11% for the relatively normalized Lampf data, 1% for our forward hemisphere data, and 4% for our backward hemisphere data. Table 23 lists the fitted normalizations for each differential cross section data set.

The normalizations obtained for our two data sets are in agreement, within the error limits set, and with the other absolutely normalized differential cross section data also. This lends good confidence to the normalization of our data.

The phase shifts which result from the analysis are listed in Table 24. Comparing these to the ones obtained from the previous analyses, one finds that there are some changes in the phases by several quoted standard

<u>Data Set</u>	<u>Normalization</u>
BASQUE (forward data)	1.01
BASQUE (backward data)	1.04
PPA	1.10
Dubna	1.00 (not floated)
Rochester	1.02
Lampf	1.11

Table 23. Phase shift fitted values of the normalizations for data near 212 MeV.  
 The Dubna data was not included in the fit.

Phase	Isospin	Value (deg)	Difference	Phase	Isospin	Value (deg)	Difference
$^1S_0$	0	17.14 $\pm$ 0.69	0.57	$^3P_0$	1	-2.12 $\pm$ 0.45	0.29
$\epsilon_1$		3.24 $\pm$ 0.41	0.84	$^1S_0$		4.32 $\pm$ 0.49	-0.21
$^3D_1$		-19.65 $\pm$ 0.59	0.71	$^3P_1$		-22.82 $\pm$ 0.16	-0.13
$^1P_1$		-25.39 $\pm$ 0.76	2.26	$^3P_2$		16.22 $\pm$ 0.13	-0.04
$^3D_2$		24.76 $\pm$ 0.63	3.24	$\epsilon_2$		-2.86 $\pm$ 0.08	-0.01
$^3D_3$		3.60 $\pm$ 0.34	1.51	$^3F_2$		1.07 $\pm$ 0.19	-0.04
$\epsilon_3$		5.72 $\pm$ 0.19	-0.57	$^1D_2$		7.41 $\pm$ 0.18	-0.04
$^3G_3$		-4.23 $\pm$ 0.32	1.18	$^3F_3$		-2.67 $\pm$ 0.14	0.01
$^1F_3$		-3.42 $\pm$ 0.31	1.16	$^3F_4$		1.71 $\pm$ 0.11	-0.02
$^3G_4$		6.07 $\pm$ 0.33	-1.13	$\epsilon_4$		-1.18 $\pm$ 0.01	0.01
$^3G_5$		0.45 $\pm$ 0.30	-0.09	$^3H_4$		0.34 $\pm$ 0.04	-0.01
				$^1G_4$		1.06 $\pm$ 0.07	0.0
				$^3H_5$		-0.86 $\pm$ 0.05	0.0
				$^3H_6$		0.20 $\pm$ 0.04	-0.01

Table 24. Phase shifts from the current analysis at 212 MeV.

The differences from the previous analysis are also shown.

deviations. This points out the fact that the error bars do not yet accurately represent the true error in the phases. The changes in the phases will be discussed in more detail in connection with their energy dependence.

### V.2.2 Data Near 418 MeV

Again, all the data in the forward hemisphere was performed at PPA<sup>46</sup>. In the backward hemisphere, there are statistically precise measurements from Lampf<sup>42</sup> and Saclay<sup>43</sup>. These latter two sets were normalized to the deuteron production from neutrons, and, so, have overall normalization uncertainties of about  $\pm 7\%$ . There is also a measurement from PPA<sup>47</sup> which has been found to disagree seriously with both the Lampf and Saclay results, and has been excluded from the analysis. Finally, there is a measurement over the full range from Carnegie<sup>50</sup>.

In addition to giving our forward and backward hemisphere data sets separate normalizations, the two backward sets were each given a separate normalization. The fitted normalizations for all the differential cross section data are listed in Table 25. Within the error limits, our three data sets agree in normalization.

<u>Data Set</u>	<u>Normalization</u>
BASQUE (forward)	1.01
BASQUE (backward, 1st set)	1.04
BASQUE (backward, 2nd set)	1.02
PPA	0.99
Carnegie	1.00
Saclay	1.00
Lampf	1.04

Table 25. Phase shift fitted normalizations  
for data near 418 MeV.  
The fitted normalizations for each differential cross  
section data set are listed.

The 1st backward data set was well fit in the analysis, having a  $\chi^2_\nu$  of about 1, while the 2nd set showed a much higher  $\chi^2_\nu$  of about 2. This indicates a source of instability in this set which has not been accounted for in the error estimate. To account for this an error of 1% was added to bring the  $\chi^2_\nu$  close to 1.

The 177.99° point had a very bad individual  $\chi^2$  of about 10, and was rejected from the data set on this basis. There is mild disagreement of our data and those of Lampf and Saclay at angles greater than 170°. No reason has been found for this.

The agreement among the data sets is acceptable, with some small shape disagreements among the three statistically precise data sets. This is an indication that the internal consistency of the data has been overestimated. Most of the data lie within one standard deviation of the fit, while none lie more than three standard deviations away. The total cross section was fit to within one standard deviation of the value measured at 418 MeV.

As for 212 MeV, the  $\chi^2_\nu$  of the overall fit was much larger than unity. The phase shifts which result from the fit are listed in Table 26. They will be discussed in

relation to the ones at other energies.

### V.3 ENERGY DEPENDENCIES

Using results from Ref. 33, differential cross section and phase shift results at 325 MeV, the energy dependencies of these quantities can be shown. Previously, the phase shift predictions for the differential cross section at forward angles did not show a smooth energy dependence. Fig 55 shows that this situation has been remedied by our data.

Figs 56 and 57 show the energy dependences of the phase shifts that are left free in the analysis. Our data has little effect on the  $I=1$  phases, and they are included only for completeness, showing the effect of the new p-p data.

The results of the previous analysis is also shown, indicating that the new data has improved the energy dependence of the  $\bar{\xi}_3$  mixing parameter and the  ${}^3G_3$  phase.

The  ${}^1F_2$  phase shows a poor energy dependence and indicates that, as in previous analyses, the real part of the forward spin-averaged scattering amplitude will have to be included to constrain the phase shift fits at 325 MeV. This amplitude will have to be re-evaluated,

Phase	Isospin	Value (deg)	Differ- ence	Phase	Isospin	Value (deg)	Differ- ence
$^3S_1$	0	$-4.78 \pm 0.77$	-1.58	$^3P_0$	1	$-20.88 \pm 0.47$	0.53
$\Sigma_1$		$7.05 \pm 0.51$	0.28	$^1S_0$		$-20.25 \pm 0.29$	0.67
$^3D_1$		$-24.77 \pm 0.41$	-0.55	$^3P_1$		$-34.76 \pm 0.22$	-1.09
$^1P_1$		$-39.03 \pm 0.83$	0.34	$^3P_2$		$18.31 \pm 0.14$	-0.05
$^3D_2$		$22.62 \pm 0.49$	0.02	$\Sigma_2$		$-2.11 \pm 0.13$	-0.18
$^3D_3$		$3.74 \pm 0.36$	0.35	$^3F_2$		$0.38 \pm 0.15$	-0.08
$\Sigma_3$		$8.49 \pm 0.20$	-1.14	$^1D_2$		$11.61 \pm 0.12$	0.0
$^3G_3$		$-5.48 \pm 0.31$	0.60	$^3F_3$		$-2.99 \pm 0.13$	0.39
$^1F_3$		$-5.12 \pm 0.18$	0.15	$^3F_4$		$3.44 \pm 0.08$	-0.10
$^3G_4$		$6.78 \pm 0.41$	0.0	$\Sigma_4$		$-1.64 \pm 0.05$	-0.04
$^3G_5$		$-1.47 \pm 0.25$	-0.21	$^3H_4$		$0.80 \pm 0.06$	-0.05
				$^1G_4$		$2.42 \pm 0.07$	-0.20
				$^3H_5$		$-1.23 \pm 0.06$	-0.05
				$^3H_6$		$0.65 \pm 0.05$	0.01

Table 26. Phase shift results from the current analysis at 418 MeV.  
The differences from the previous analysis are also shown.

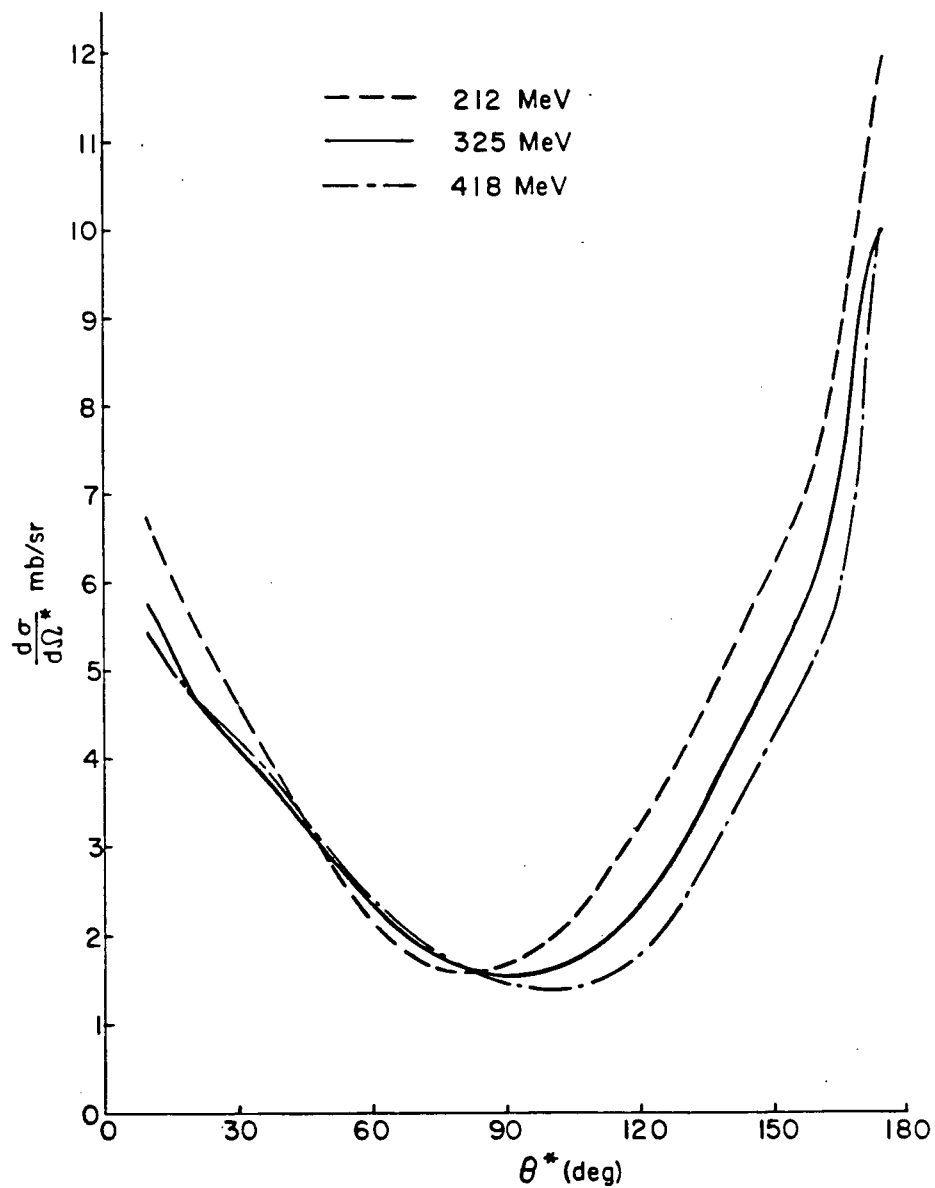


Fig 55. Energy dependence of the differential cross section.  
 The extreme forward region of the distributions now show a smooth energy dependence.

$\text{I}$  phases with new data included  
 $\times, \circ$  previous phases (where different from new ones)  
 — Paris potential predictions  
 (deg)

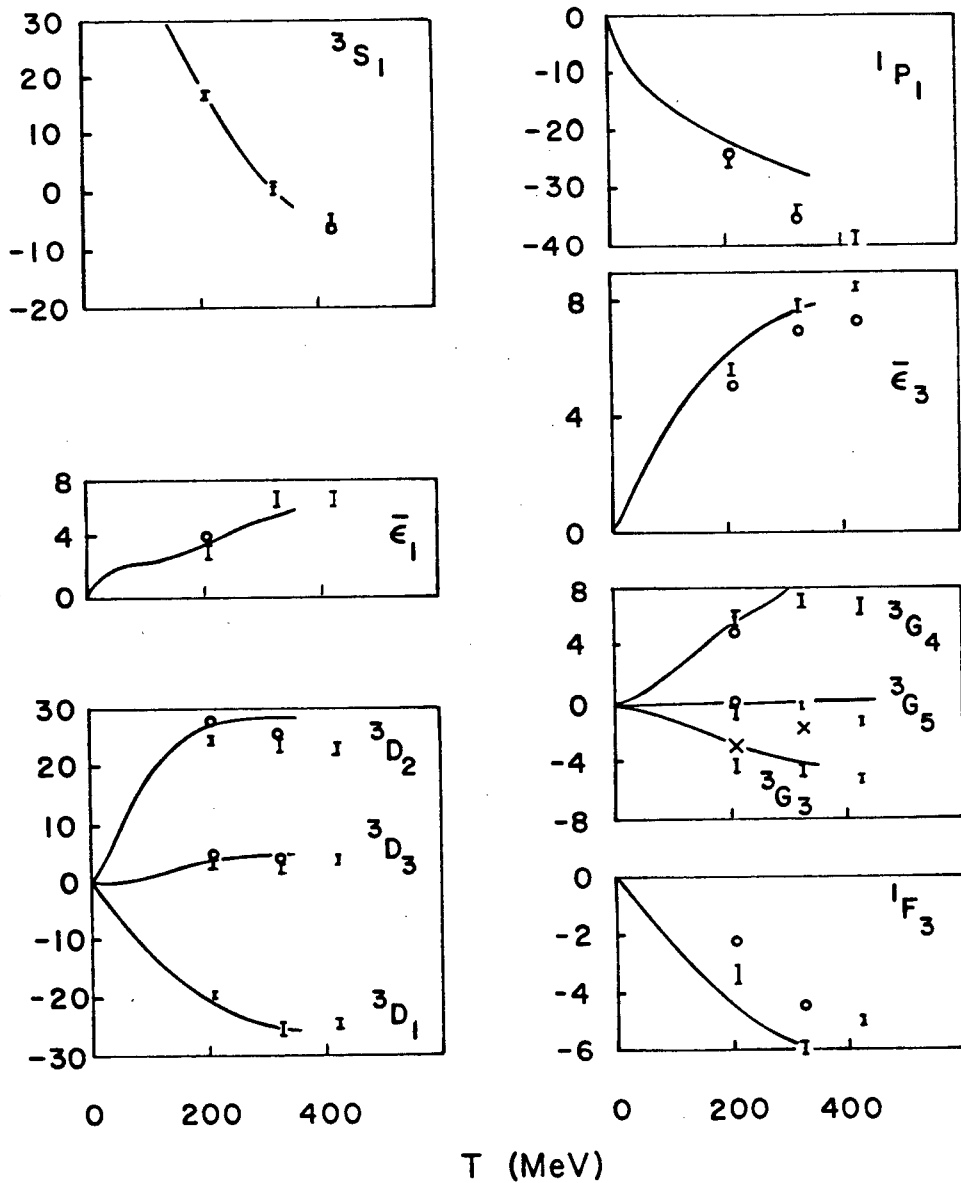


Fig 56. Energy dependence of the I=0 phase shifts.  
 The dependence has improved over previous fits, especially for  $\bar{E}_3$  and  ${}^3G_3$ . The results<sup>13</sup> of the Paris group's dispersion relation approach are also shown.

† phases with new data included  
 • previous phases (where different from new ones)  
 — Paris potential predictions

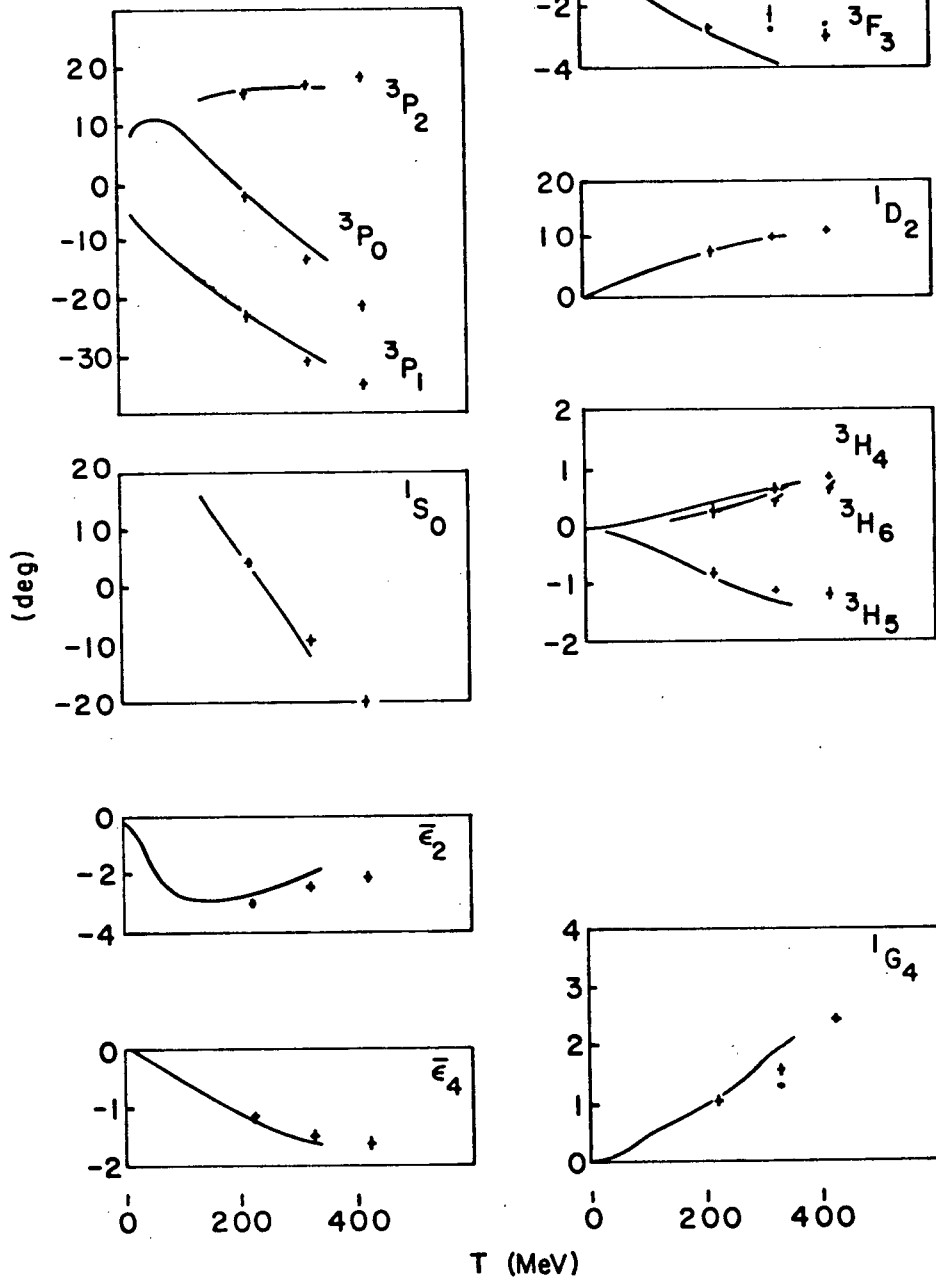


Fig 57. Energy dependence of the I=1 phase shifts.

The I=1 phase shifts are virtually unaffected by our new data. They are shown to update those of Ref 41, with the new p-p data. The Paris group's results<sup>13</sup> are also shown.

including the new values of the total n-p cross section in the intermediate energy region. This re-evaluation may affect the conclusion concerning the  ${}^3G_3$  phase improvement, however.

#### V.4 CONCLUSION

The shape of the n-p elastic differential cross section has been measured to about 2%, with overall normalizations of 3-4% at 212 and 418 MeV, over the full angular range.

The energy dependence of  $d\sigma/d\Omega$  in the extreme forward angles has become more reasonable than was previously indicated in phase shift analyses. Furthermore, the energy dependence of the phase shifts has improved, notably those of  $\bar{\xi}_2$  and  ${}^3G_2$ .

The BASQUE measurements of n-p elastic scattering observables have provided unambiguous information about the I=0 N-N phase shifts in the energy range 200-500 MeV. This ties in with the I=1 phases which were already well determined to provide a good phenomenological description of the N-N interaction in this energy region. This phenomenology can now be used to compare with strong

interaction models, which, as yet, provide no theory. This information can also be directly applied to nuclear physics calculations requiring knowledge of the N-N force.

REFERENCES

1. Chadwick J.            Nature 129, 312(1932)
2. Lock W.O., Measday D.F.    Intermediate Energy Physics,  
Methuen, London, (1967)
3. Gammel J.L., Thaler R.M.    Phys Rev 107, 291,1395(1957)
4. Heisenberg W.            Zeit F Phys 77, 1(1932)
5. Kellogg J.M.B.            Phys Rev 55, 318(1939)
6. Wigner E.                Proc Nat Acad Sci U.S. 27, 281(1941)
7. Yukawa H.                Proc Phys-Math Soc Japan 20, 720(1938)
8. Lattes C.M.G., Muirhead H., Occhialini G.P.S., Powell C.F.  
Nature 159, 694(1947)
9. Arndt R.A.                Phys Rev C20, 555(1974)
10. Erkelenz K.              Phys Reports 13C, 5(1974)
11. MacGregor M.H., Stapp H.P., Moravcsik M.J.  
Ann Rev Nucl Sci 11, 95(1961)
12. Arndt R.A.                Phys Rev 141, 873(1966)
13. Vinh Mau R.              Mesons in Nuclei, Wiley, New York
14. Bryan R.A.                Texas A&M Univ Report Oro-5223-10
15. Signell P.                Proceedings of the Telluride Conference,  
11, 95(1979)
16. MacGregor M.H., Arndt R.A., Wright R.M.    Phys Rev 182,  
1714(1969)

17. Shepard P.F., Devlin T.J., Mischke R.E., Solomon J.  
PPA Report PPAR 10
18. Ashmore A., Range W.H., Taylor R.T., Townes B.M., Castillejo L.,  
Peierls R.F. Nucl Phys 36, 258(1962)
19. Bugg D.V., TRIUMF Internal Report TRI-75-5, (1975)
20. Richardson J.R. IEEE Trans Nucl Sci 22, 3(1975)
21. Craddock M.K. Nature 270, 671(1978)
22. Linlor W.I. UCRL Report 2303, 1(1953)
23. Richardson J.R. Nucl Instr and Meth 24, 493(1963)
24. Craddock M.K. (Ed.) TRIUMF Annual Report (1978)
25. Hodges T.A. TRIUMF Internal Report TRI-1-73-2, (1973)
26. Singleton A.H., Lapin A. Adv in Cryo Eng 11, 617(1966)
27. Ludgate G.A. Thesis, Rutherford Lab, HEP/T/62, (1976)
28. Charpak G. Ann Rev Nucl Sci 20, 195(1970)
29. Larsen R.R. Nuovo Cim 18, 1039(1960)
30. Lecroy HV4032 Programmable Power Supply
31. Edgington J.A. Nucl Instr and Meth 164, 175(1979)
32. Arndt R.A., Hackman R.H., Roper L.D. Phys Rev C15, 1002(1977)
33. Keeler R.K. Thesis, University of British Columbia,  
(unpublished), (1980)
34. Carlini R., Dieterle B., Donahue J., Leavitt C., Rupp T.,  
Thomas W., Wolfe D., Auerbach L.B.,  
Highland V.L., Johnson K.F., MacFarlane W.K.,  
Pratt J., Bentley R. Phys Rev Lett 41,  
1341(1978)



47. Shepard P.F., Devlin T.J., Mischke R.E., Solomon J.  
Phys Rev D10, 2735(1974)
48. Thomas A.R., Spalding D., Thorndike E.H. Phys Rev 167, 1240  
(1968)
49. Kazarinov Y.M., Simonov Y.N. JETP 16, 24(1963)
50. Hartzler A.J., Siegel R.T., Opitz W. Phys Rev 95, 591(1954)
51. Lacombe M., Loiseau B., Richard J.M., Vinh Mau R.  
Phys Rev C21, 861(1980)
52. Bubble Chamber Group Selected Cryogenic Handbook, BNL
53. Measday D.F., Spuller J.E., Menard M.R. TRIUMF Kinematics  
Handbook
54. Evans R.D. The Atomic Nucleus, McGraw Hill, Toronto(1955)
55. Hess R. private communication

APPENDIX A. MWPC TRACK FITTING CRITERIA

The MWPC's have an effective 4 mm wire spacing, and, given the integral wire number of the wire hit, the x (or y) coordinate can easily be calculated. Often several wires in a chamber fired, so that some procedure was required to determine which wires formed clusters and which had fired singly, as it was quite possible to have more than one track going through the chambers.

Groups of consecutive wires were treated in two ways: if three or less fired adjacently, they were considered to have been due to a single track which had passed through the centre of the cluster. For greater than three, the entire cluster was passed on as single wires. No a priori decision could be made as to where, in a large cluster, the track had passed. This decision was left to the track fitting code.

Once the number of discrete wire firings in each chamber had been determined, the granularity of the integral wire numbers was removed by randomizing the coordinate, using a square distribution, over the 4 mm of the wire resolution.

To find whether an event had a fittable track, the code tried all combinations of wires fired in the MWPC's in each plane, eg. for three wires in each of three chambers, in one plane, fits to 27 lines were attempted. For each set of wires a linear least squares fit was made, with the goodness of fit requirement based on the error of the intercept of the fitted line, which was proportional to the  $\chi^2$  of the fit.

Events where only two chambers fired, in any plane, were accepted on the condition that there was only a single cluster in each chamber. Of course, a fit was not required to obtain the equations of these lines. In the vertical plane, where there were four chambers, it was assumed that any one could misfire. If no four-chamber fit was obtained, all combinations of wires in any three chambers were tried to see if an acceptable fit could be found.

In the case of multiple lines fit, rather than look for a vertex (in that plane) at the carbon, the line with the smallest  $\chi^2$  was taken as the best, and was the only one used to characterize the event. Originally, a vertex criterion was used, but had a low success rate. The MWPC's were found to often fire wires close to each other, but

not adjacent. Frequently, lines were fit to all these wires, giving multiple lines which diverged on their way to the carbon. The  $\chi^2$  criterion was used to eliminate those lines, rather than a test on the proximity of the clusters.

APPENDIX B. CORRECTION FOR INCOMPLETE AZIMUTHAL ACCEPTANCE  
OF DETECTORS

This appendix describes an algorithm whose purpose is to compensate for the limited azimuthal acceptance of detectors. Consider a planar detector viewing particles coming from a point source. As the polar angle  $\theta$  increases, there comes a value for  $\theta$  for which detection becomes a function of the azimuthal angle  $\phi$ , as well. For these values of  $\theta$ , only particles having a restricted range of values of  $\phi$  can be detected. This algorithm calculates the region of  $\phi$  accessible and then determines a factor  $2\pi / \phi_{\text{allowed}}$  which is used to weight the number of detected particles, eliminating the dependence on  $\phi$ , and so the dependence on the geometry of the detector.

### E.1 PRINCIPLE OF THE ALGORITHM

Differential cross sections depend only on the polar angle of scatter,  $\theta$ . Therefore, the number of particles observed by a detector is

$$N_{obs} = \int_0^{\theta_{max}} N(\theta) \int_{\phi} d\phi$$

where the azimuthal angle  $\phi$  is integrated over all regions allowed for that value of  $\theta$ , as shown in Fig B1.

Define

$$\int d\phi = 2\pi\beta$$

If the detector were of infinite extent, there would be no limits on  $\phi$ , and

$$\beta = 1$$

and so the true number of events scattered at angle would be

$$N_{true} = N_{obs}/\beta$$

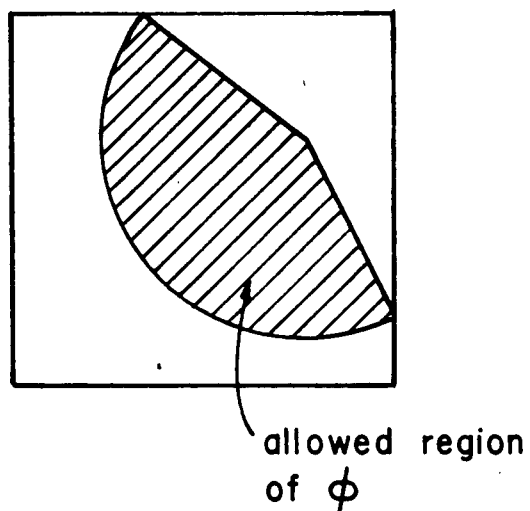


Fig B1. Allowed regions of the azimuthal scattering angle.

The amount of the azimuthal range available depends on the polar scattering angle, being unrestricted at small angles and zero at large angles.

with the result that a calculation of  $\beta$  would allow the determination of  $N_{true}$  from the data.

Consider now the case shown in Fig B2. An incident particle whose direction is  $(\theta_0, \phi_0)$  with respect to the z axis scatters at angle  $(\theta, \phi)$  into the detector. In general, the cone generated by rotating the scattered track about the incident one would intersect the detector forming an ellipse. In order to determine the fraction of the ellipse circumference inside the detector, it is necessary to calculate the interaction points of the ellipse with the detector boundaries.

Define a coordinate frame based on the incident track

$$\begin{aligned}\hat{z}' &= \sin\theta_0 \cos\phi_0 \hat{x} + \sin\theta_0 \sin\phi_0 \hat{y} + \cos\theta_0 \hat{z} \\ \hat{y}' &= \hat{z}' \times \hat{z} \\ \hat{x}' &= \hat{z}' \times \hat{y}'\end{aligned}$$

then in this frame, the major axis of the ellipse will intersect the cone at azimuthal angles

$$\phi' = 0, \pi$$

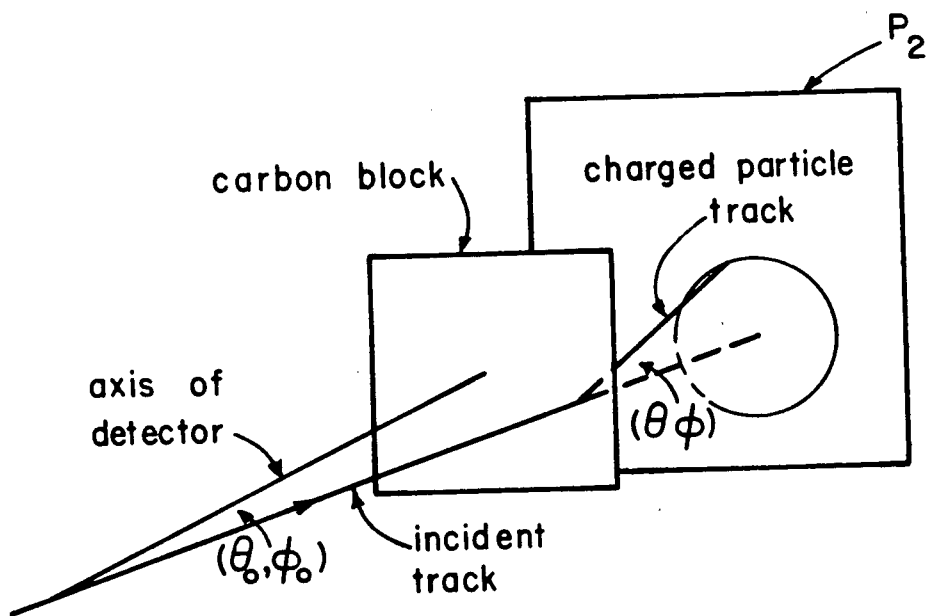


Fig B2. Geometry of the  $\phi$ - $s$  algorithm.  
 A typical event is characterized by a track incident on the carbon at  $(\theta_0, \phi_0)$ , with a scattered track at  $(\theta, \phi)$  into P<sub>2</sub>.

One uses the transformation matrix  $M$  to go from the primed frame to the detector frame

$$\begin{pmatrix} x \\ y \\ z \end{pmatrix} = M \begin{pmatrix} x' \\ y' \\ z' \end{pmatrix} = \begin{pmatrix} \cos \theta_0 \cos \phi_0 & -\sin \phi_0 & \sin \theta_0 \cos \phi_0 \\ \cos \theta_0 \sin \phi_0 & \cos \phi_0 & \sin \theta_0 \sin \phi_0 \\ -\sin \theta_0 & 0 & \cos \theta_0 \end{pmatrix} \begin{pmatrix} x' \\ y' \\ z' \end{pmatrix}$$

and back by

$$\begin{pmatrix} x' \\ y' \\ z' \end{pmatrix} = M^{-1} \begin{pmatrix} x \\ y \\ z \end{pmatrix} = \begin{pmatrix} \cos \theta_0 \cos \phi_0 & \cos \theta_0 \sin \phi_0 & -\sin \theta_0 \\ -\sin \phi_0 & \cos \phi_0 & 0 \\ -\sin \theta_0 \cos \phi_0 & \sin \theta_0 \sin \phi_0 & \cos \theta_0 \end{pmatrix} \begin{pmatrix} x \\ y \\ z \end{pmatrix}$$

Note that for  $\theta_0 = 0$   $M$  reduces to the unit matrix as expected.

Repeated use of these transformations yields the two points on the major axis of the ellipse in the detector frame: the distance between these two points gives the semi-major axis, and the average of the two gives the center of the ellipse. Note that the center of the ellipse

does not correspond to the intersection point of the incident track with the detector.

For an ellipse with its major axis along an axis  $x''$ , the equation of the ellipse with semi-major and -minor axes  $a$  and  $b$ , one has

$$\frac{x''^2}{a^2} + \frac{y''^2}{b^2} = 1 \quad (b.1)$$

If this ellipse is rotated by an angle  $\phi$ , as in Fig B3, then

$$\begin{pmatrix} x'' \\ y'' \end{pmatrix} = \begin{pmatrix} \cos\phi_0 & \sin\phi_0 \\ -\sin\phi_0 & \cos\phi_0 \end{pmatrix} \begin{pmatrix} x \\ y \end{pmatrix}$$

The minor axis is obtained in a similar fashion to the major axis. A point on the cone is chosen which lies on the intersection of the detector and the ellipse, and is transformed back to the detector frame. Then the center point and this point are transformed to the double-primed frame where equation b.1 holds, so that the minor axis can be simply solved for in terms of  $x'', y''$  and the major axis.

Upon transforming equation b.1 to the detector frame,

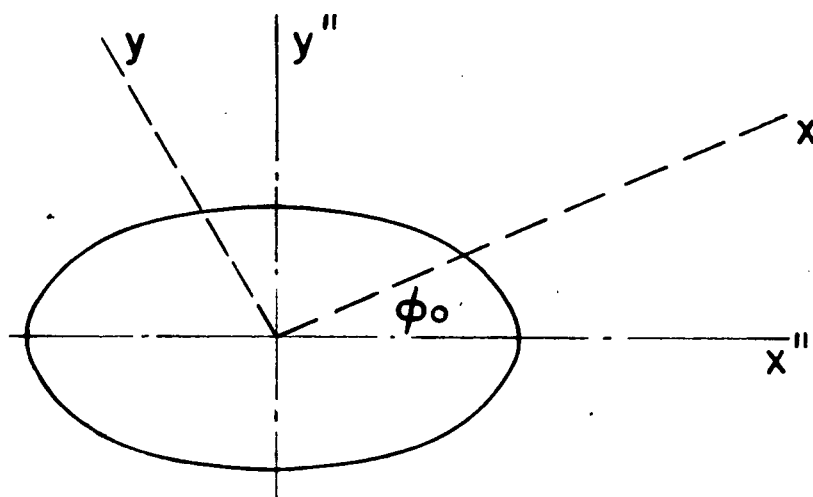


Fig B3. Rotation of the exit track ellipse by the incident azimuthal angle.  
The azimuthal angle of the incident track will determine the amount of rotation of the ellipse on P2.

the equation of the ellipse becomes

$$\frac{x^2}{x_i^2} - 2r_{12}xy + \frac{y^2}{y_i^2} = 1$$

with

$$\begin{aligned} x_i^2 &= b^2 \cos^2 \phi_0 + a^2 \sin^2 \phi_0 \\ y_i^2 &= b^2 \sin^2 \phi_0 + a^2 \cos^2 \phi_0 \\ r_{12} &= -\sin \phi_0 \cos \phi_0 (b^2 - a^2) \end{aligned}$$

Given the equation of the ellipse, one can obtain the eight possible intersection points (Fig B4) of the ellipse and the four boundary lines of the detector. These eight values are termed the  $\phi_{1-8}$ . Transformation of these intersection points into the primed frame yields the azimuthal angles on the cone. Setting the angle  $\phi'$  to  $c_1$  for all  $\phi_{1-8}$  intersection points outside the boundaries, and to  $c_2$  all those which did not have an intersection point, the weighting factor is

$$\beta = \frac{1}{2\pi} \int d\phi = \sum_{i=1}^8 (-1)^i \phi_i$$

For every data point, with  $(\theta, \phi)$ ,  $\beta$  is

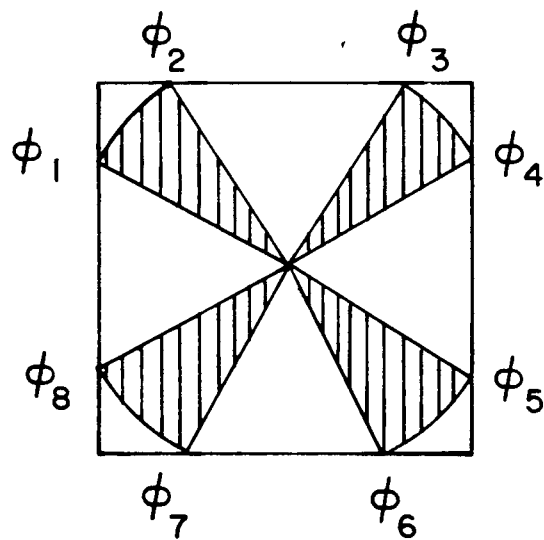


Fig B4. Definition of the eight possible intersections of the ellipse and the detector boundaries. Depending on the size of the ellipse, there are eight possible intersections of the ellipse and the detector boundaries.

calculated and used to weight that point, compensating for the finite size of the detector. The data itself then acts as a Monte Carlo integration over the allowed polar angles  $\theta$ .

## E.2 APPLICATION TO THE NEUTRON DETECTOR

As discussed in Sec IV., at 212 MeV the detector P2 developed a region of low efficiency, so that P2 effectively had a "hole" in the bottom. With a cut of  $17^\circ$  on the polar angle, the only source of loss in  $\phi$  was in the inefficient region, P2E.

There was no information on the incident neutron track, so that their origins were randomized over the target volume.  $(\theta_0, \phi_0)$  was then calculated using the reconstructed interaction point at the carbon converter. The  $\phi_{1-3}$  algorithm was used to calculate the allowed region of  $\phi$ .  $\beta'$  so that weighting the data by the factor

$$\frac{1}{\beta} = \frac{1}{1 - \beta'}$$

corrected for the loss of P2E.

The algorithm was tested on the 22.5 $^\circ$  setting at 212

MeV, and  $10^\circ$  at 418 MeV. P2E was operational for both of these settings. The data was analyzed as usual, and with P2E artificially removed using the MWPC's and then "replaced" by the  $\phi_{1.8}$  algorithm. The agreement between the pairs was better than 0.25%.

Fig B5 shows a similar pair of histograms for a setting at 212 MeV in which P2E had failed. This is illustrated by the distinct slope in the profile in the uncorrected data. The slope is removed by the algorithm, showing that no instrumental or geometrical inefficiencies remain.

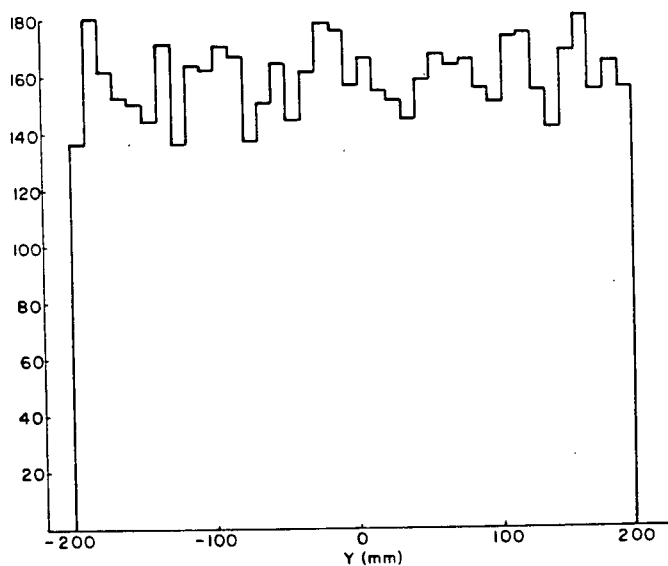
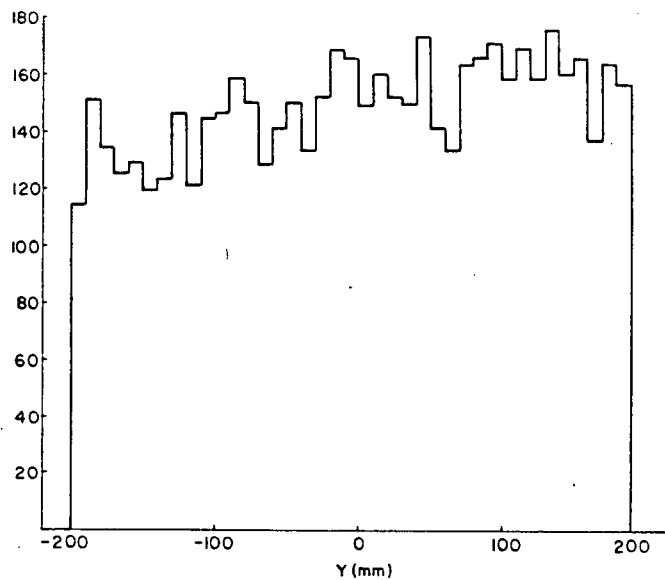


Fig B5. Vertical profile at the carbon with P2E failed.  
The vertical profile shows a distinct rise from the bottom to the top of the carbon. This is due to the failure of P2E, which is at the bottom of the P2E hodoscope.

APPENDIX C. DENSITIES OF LIQUID AND GASEOUS HYDROGEN IN  
THE TARGET

This Appendix describes the procedure used to determine the density of the para-hydrogen liquid in the target when it was full, and of the gas when it was nominally empty. The thermodynamic data used in this Appendix are from Ref 52.

The pressure of the target was maintained at  $17.00 \pm 0.25$  psia by the refrigerator. A plot of vapour pressure versus temperature is shown in Fig C1, indicating that the liquid temperature was

$$T_{liq} = 20.76 \pm 0.06 \text{ K}$$

In Fig C2, a plot of temperature versus density is shown. The liquid density was  $0.0350 \pm 0.0002$  g-mole/cm<sup>3</sup>, corresponding to

$$\rho_{liq} = 0.0701 \pm 0.0004 \text{ g/cm}^3$$

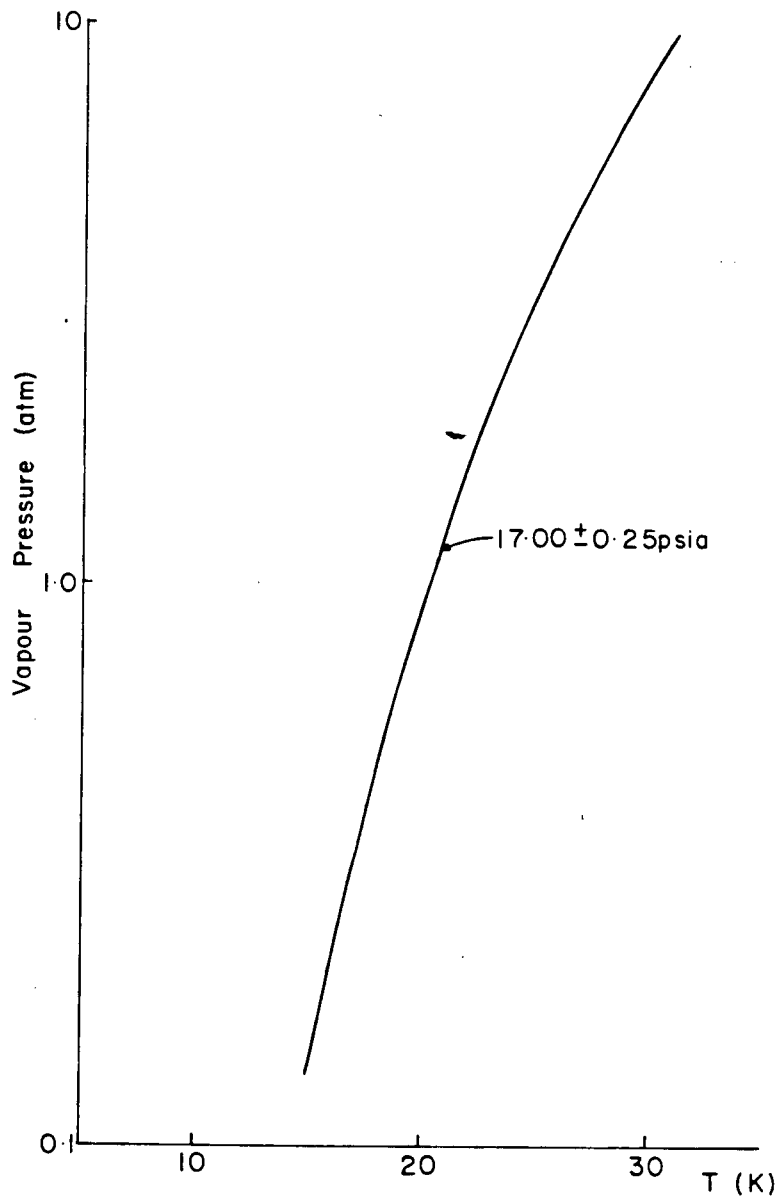


Fig C1. Temperature of the liquid as a function of the pressure.

The data was taken from Ref 52. The pressure was held constant by the refrigerator, allowing the temperature to be determined.

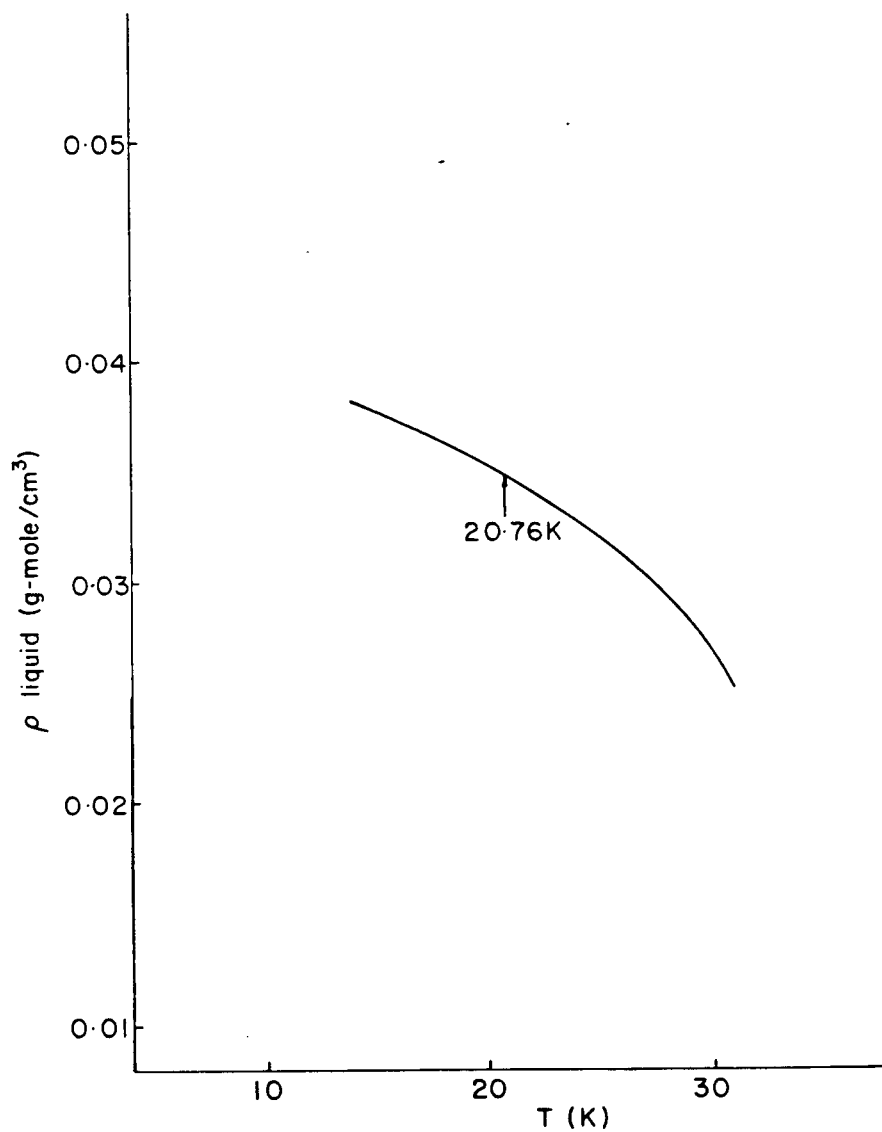


Fig C2. Density of the liquid hydrogen as a function of temperature.  
The data was taken from Ref 52. Note the units of g-mole/cm<sup>3</sup>.

The temperature of the target was monitored by Cu/Constantan thermocouples, which, using the liquid temperature as a base, gave a gas temperature of

$$T_{\text{gas}} = 48 \pm 8 \text{ K}$$

Plots of temperature against density were not available for the gas phase, and intermediate isotherm plots of pressure versus entropy and density versus entropy (Fig C3) were used. Fig C4 shows the relation between the temperature and gas density at the constant pressure of 17 psia, yielding

$$p_{\text{gas}} = (2.7 \pm 0.1) \cdot 10^{-4} \text{ g-mole/cm}^3, \text{ or}$$

$$p_{\text{gas}} = (5.4 \pm 0.2) \cdot 10^{-4} \text{ g/cm}^3$$

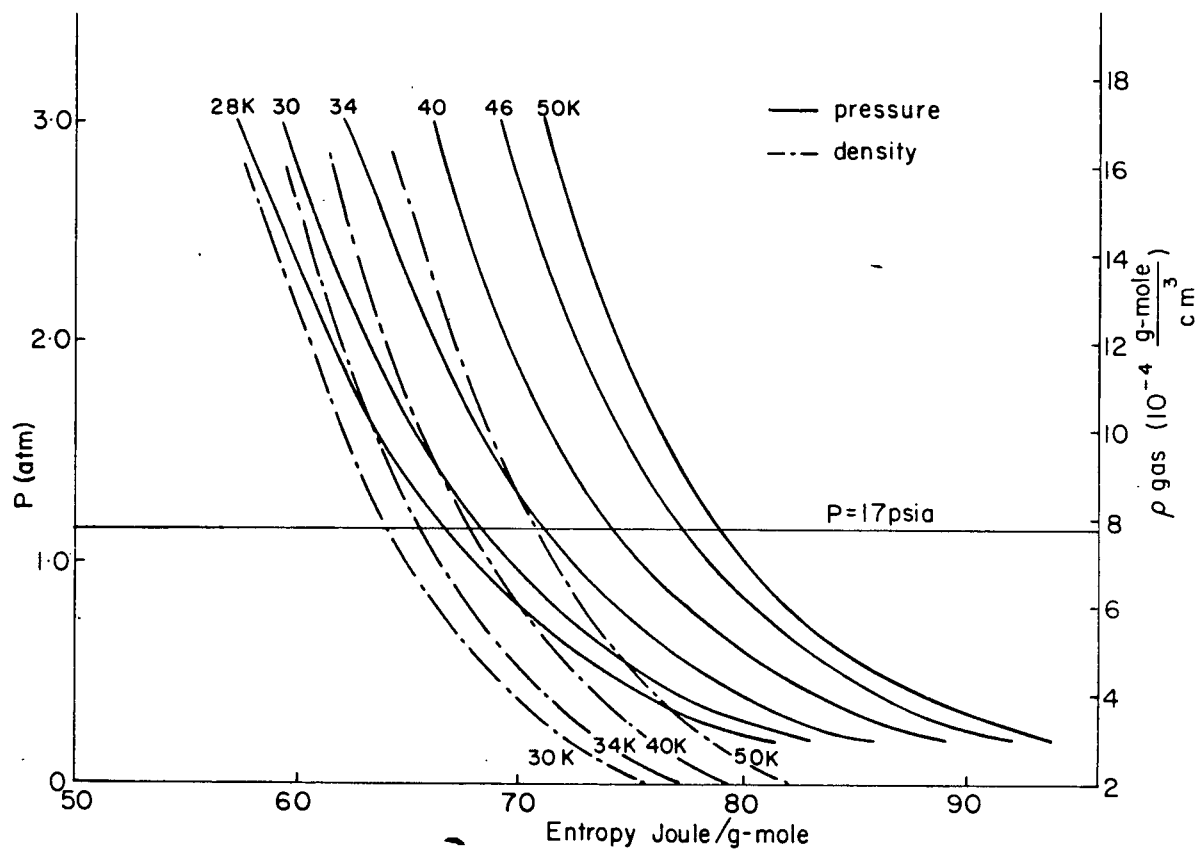


Fig C3. Hydrogen gas pressure and density as functions of entropy.

As data on gas density versus temperature were unavailable, intermediate plots of density and pressure against entropy were used to obtain the isobaric plot of density versus temperature.

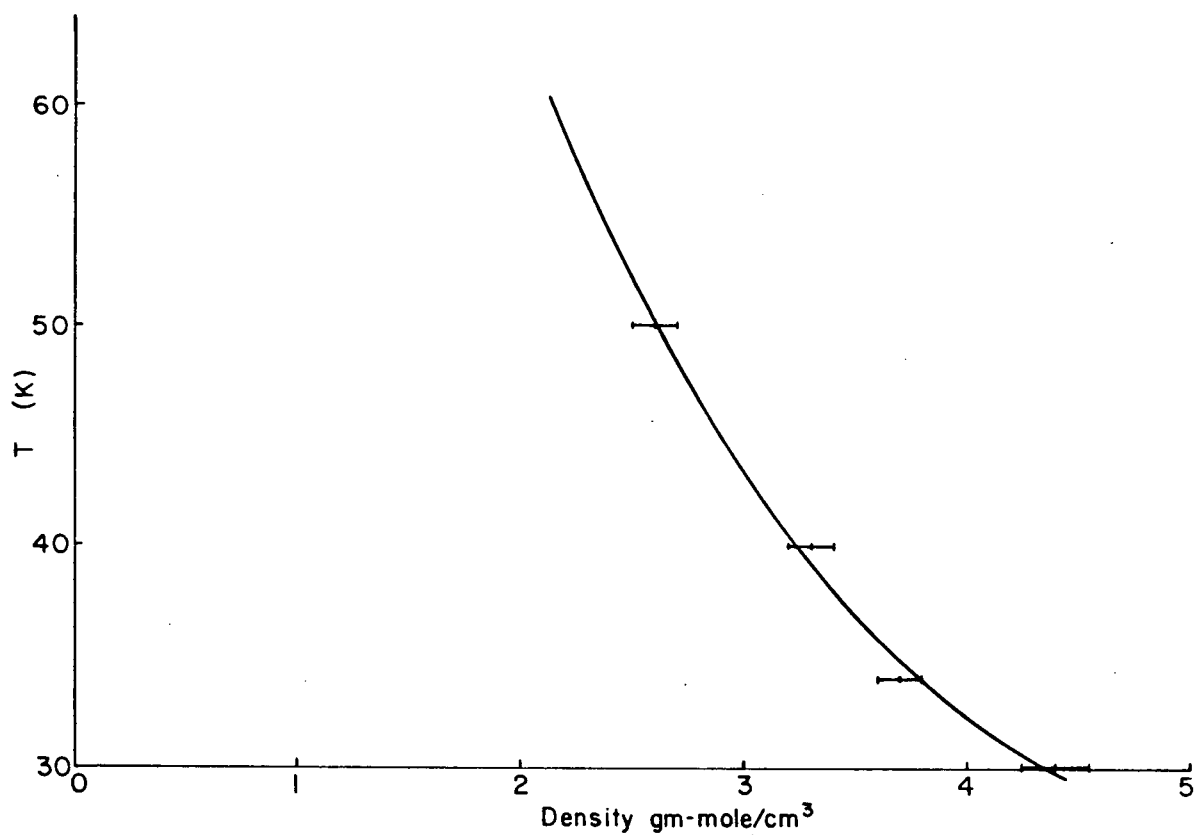


Fig C4. Hydrogen gas density as a function of temperature.  
The points below 50 K were obtained using Fig C3. Above 50 K the hydrogen behaves as an ideal gas.

APPENDIX D. INVENTORY OF MATERIALS

This appendix deals with the amount of material between the point of scatter in the hydrogen target and the detectors. It will pertain specifically to the spectrometer, with small changes required in the length of air to describe the other two configurations. This information is required for the corrections applied for attenuation and multiple scattering, and to range-energy cutoffs in the spectrometer.

Protons scattered out of the hydrogen target lost energy before they reached the spectrometer magnet, so that the measurement yielded a value less than the true scattered momentum.

The energy lost by protons in matter by Coulomb scattering from electrons has been well documented<sup>53</sup>. The range of protons in non-hydrogenous materials can be related to each other by<sup>54</sup>

$$\frac{R_1}{R_2} = \sqrt{\frac{A_1}{A_2}}$$

where the R's are ranges (in g/cm<sup>2</sup>) in the materials, and

the A's the atomic numbers. For simplicity, the thicknesses of all non-hydrogenous materials were converted to carbon equivalent using the above relation.

Table D1 lists the materials between the hydrogen and the spectrometer magnet. The mean path length of the protons in the hydrogen was calculated and is shown in Fig D1. For scattering angles less than  $34^\circ$ , the curvature of the aluminium dome made it normal to the proton trajectories, while above that angle, the thickness varied inversely with the sine of the angle. As a function of scattering angle, the material thickness was

for  $\theta < 34^\circ$

$$t = d(\theta) (H) + 1.44 (C) \quad (\text{g/cm}^2)$$

and for  $\theta > 34^\circ$ ,

$$t = d(\theta) (H) + 0.45/\sin(\theta) (C) + 0.99 (C) \quad (\text{g/cm}^2)$$

The quantities in brackets refer to either hydrogen or carbon-equivalent materials, and  $d(\theta)$  is the mean path

Material -----	Thickness (g/cm <sup>2</sup> ) -----	Carbon-equivalent Thickness (g/cm <sup>2</sup> ) -----
mylar surrounding the target	0.053	0.041
aluminium dome	0.274	0.41
air before magnet	0.277	0.31
scintillator	0.50	0.32
MWPC wires before magnet	0.17	0.20
mylar surrounding MWPCs	0.21	0.16
air after magnet	0.24	0.27
MWPC wires after magnet	0.17	0.20
mylar surrounding MWPCs after magnet	0.21	0.16
		Total -----
		2.07

Table D1. Thickness of materials between the hydrogen target and spectrometer.  
The materials are listed in terms of linear dimensions and carbon-equivalent thickness.

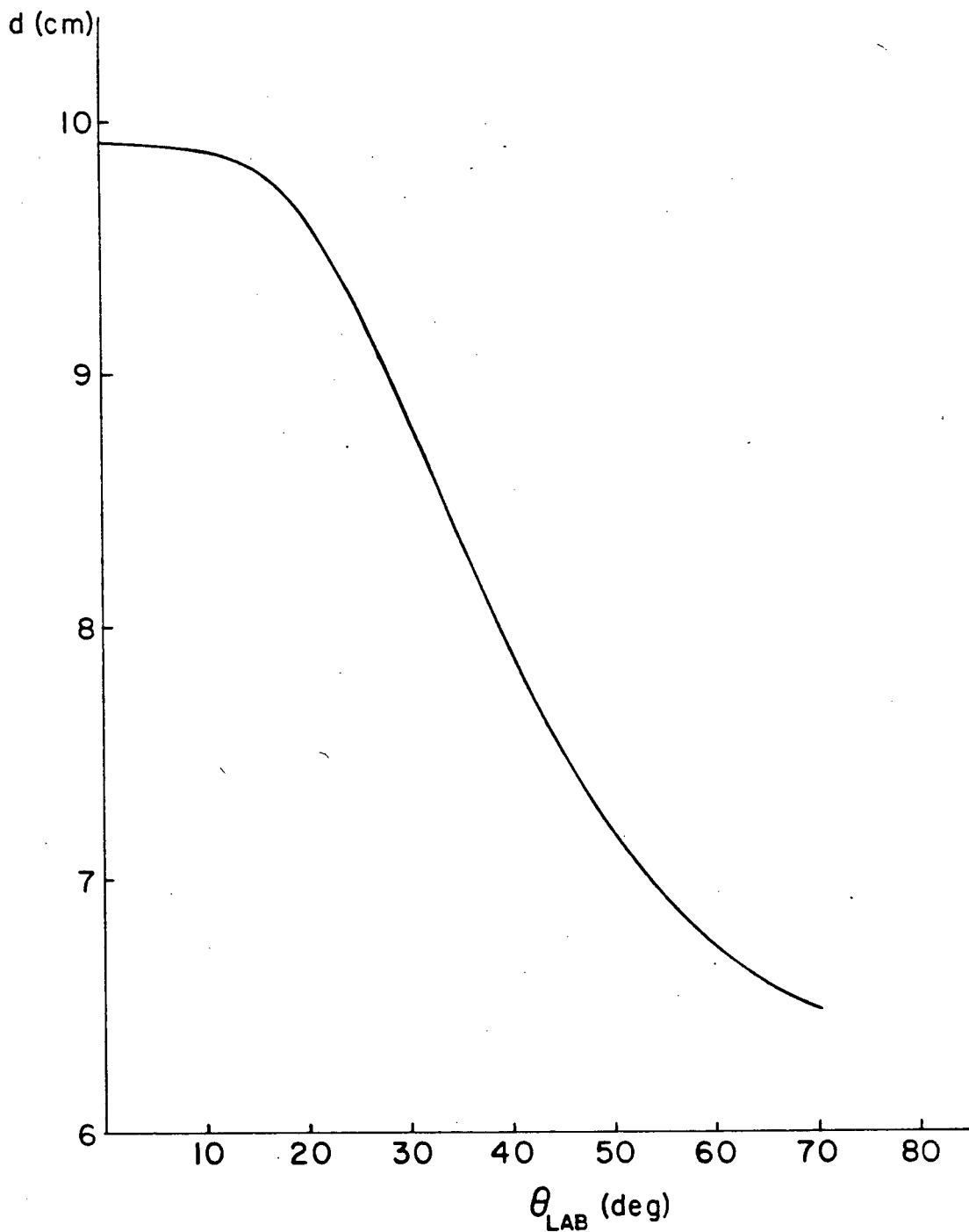


Fig D1. Mean path length of scattered protons in hydrogen.  
The mean path length was calculated from the geometry of the apparatus and the differential cross section predicted from phase shift analysis.

length in hydrogen.